SANDIA REPORT
SAND2014-1217
Unlimited Release
February 2014

Plastic Cap Evolution Law Derived From Induced Transverse Isotropy In Dilatational Triaxial Compression

David James Macon, Rebecca Moss Brannon, and Otto Erik Strack

Prepared by
Sandia National Laboratories
Albuquerque, New Mexico 87185 and Livermore, California 94550

Sandia National Laboratories is a multi-program laboratory managed and operated by Sandia Corporation, a wholly owned subsidiary of Lockheed Martin Corporation, for the U.S. Department of Energy's National Nuclear Security Administration under contract DE-AC04-94AL85000.

Sandia National Laboratories

Issued by Sandia National Laboratories, operated for the United States Department of Energy by Sandia Corporation.

Printed in the United States of America. This report has been reproduced directly from the best available copy.

Available to DOE and DOE contractors from
U.S. Department of Energy
Office of Scientific and Technical Information
P.O. Box 62
Oak Ridge, TN 37831

Telephone: (865) 576-8401
Facsimile: (865) 576-5728
E-Mail: reports@adonis.osti.gov
Online ordering: http://www.osti.gov/bridge

Available to the public from
U.S. Department of Commerce
National Technical Information Service
5285 Port Royal Rd.
Springfield, VA 22161

Telephone: (800) 553-6847
Facsimile: (703) 605-6900
E-Mail: orders@ntis.fedworld.gov
Online order: http://www.ntis.gov/help/ordermethods.asp?loc=7-4-0#online

SAND2014-1217
Unlimited Release
February 2014

Plastic Cap Evolution Law Derived From Induced Transverse Isotropy In Dilatational Triaxial Compression

David James Macon
Department of Mechanical Engineering,
The University of Utah
Salt Lake City, UT 84112

Rebecca Moss Brannon
Department of Mechanical Engineering,
The University of Utah
Salt Lake City, UT 84112

Otto Erik Strack
Sandia National Laboratories
P.O. Box 5800
Albuquerque, New Mexico 87185-MS1320

Abstract

Mechanical testing of porous materials generates physical data that contain contributions from more than one underlying physical phenomenon. All that is measurable is the “ensemble” hardening modulus. This thesis is concerned with the phenomenon of dilatation in triaxial compression of porous media, which has been modeled very accurately in the literature for monotonic loading using models that predict dilatation under triaxial compression (TXC) by presuming that dilatation causes the cap to move outwards. These existing models, however, predict a counter-intuitive (and never validated) increase in hydrostatic compression strength. This work explores an alternative approach for modeling TXC dilatation based on allowing induced elastic anisotropy (which makes the material both less stiff and less strong in the lateral direction) with no increase in hydrostatic strength.

Induced elastic anisotropy is introduced through the use of a distortion operator. This operator is a fourth-order tensor consisting of a combination of the undeformed stiffness and deformed compliance and has the same eigenprojectors as the elastic compliance. In the undeformed state, the distortion operator is equal to the fourth-order identity. Through the use of the distortion operator, an evolved stress tensor is introduced. When the evolved stress tensor is substituted into an isotropic yield function, a new anisotropic yield function results. In the case of the von Mises isotropic yield function (which contains only deviatoric components), it is

shown that the distortion operator introduces a dilatational contribution without requiring an increase in hydrostatic strength.

In the thesis, an introduction and literature review of the cap function is given. A transversely isotropic compliance is presented, based on a linear combination of natural bases constructed about a transverse-symmetry axis. Using a probabilistic distribution of cracks constructed for the case of transverse isotropy, a compliance expression is presented that demonstrated a decrease in lateral stiffness, but leaves axial stiffness unchanged. A demonstration of how the distortion operator could be used in the elastic/plastic analysis of a von Mises surface loaded in TXC is also presented.

ACKNOWLEDGMENTS

This report is a verbatim public release of a Masters thesis by the same name by the first author, David Macon, under advisement of the second author, Rebecca Brannon, with a research grant initiated by the third author, Erik Strack of Sandia National Laboratories.

The first author would like to thank Nancy King for her patience with me during this project, and for her loving support.

CONTENTS

FIGURES

TABLES

NOMENCLATURE

Symbol	Definition	Units (SI units)
a	Crack size	m
$a_1,\ a_2,\ a_3,\ a_4$	Experimental constants from Kayenta model	Units vary
$\underset{\approx}{b}_1, \underset{\approx}{b}_2, \underset{\approx}{b}_3, \underset{\approx}{b}_4, \underset{\approx}{b}_5$	Fourth-order transverse basis tensor about $\underset{\sim}{m}$	1
$\underset{\approx}{B}_1,\ \underset{\approx}{B}_2,\ \underset{\approx}{B}_3,\ \underset{\approx}{B}_4,\ \underset{\approx}{B}_5$	Fourth-order transversely-isotropic base tensors	1
c	$c = \cos\theta$	1
$\underset{\approx}{c}^o$	Fourth-order open fabric tensor	1
$\underset{\approx}{C}$	Fourth-order elastic tangent stiffness of the deformed material	Pa
$\underset{\approx}{C}_m$	Fourth-order isotropic elastic tangent stiffness of the undeformed material	Pa
E_o	Young's modulus of the substrate material	Pa
F_ρ	Third moment of the number density function	Number of cracks$\cdot$m
G_o	Shear modulus of the substrate material	Pa
$h_1,\ h_2,\ h_3,\ h_4,\ h_5$	Components of the compliance matrix for a transversely isotropic material	Pa^{-1}
$h_1^c, h_2^c, h_3^c, h_4^c, h_5^c$	$\underset{\approx}{b}_i$ basis coefficients, $h_i^c = \sum_{j=1}^{5} \int_0^{\pi} \tilde{\alpha}_j(\theta)\beta_{ij}(\theta)\,d\theta$	Pa^{-1}
h	Parameter used in definition of elastic-plastic coupling tensor $\underset{\approx}{Z}$	1
h_i'	Tsai-Wu strength tensors of the second rank	Pa^{-1}
h_{ij}'	Tsai-Wu strength tensors of the fourth rank	Pa^{-2}
H	Ensemble hardening modulus	Pa
$I_1,\ I_2,\ I_3$	Invariants of the stress tensor	Pa
$\underset{\sim}{I}$	Second-order identity tensor	1
$\underset{\approx}{I}$	Fourth-order identity tensor	1
$J_1 = I_1,\ J_2,\ J_3$	Invariants of the deviatoric stress tensor	Pa
J_2^ξ	Second invariant of the shifted stress tensor	Pa
k	Critical value from yield function	Units vary

Symbol	Definition	Units (SI units)
$K_{\Delta\tilde{\alpha}_3}$	Constant	Pa^{-1}
$\underset{\approx\approx}{L}$	Fourth-order distortion operator	1
$\underset{\sim}{m}$	Axis of symmetry for a transversely isotropic material of unit length coinciding with the principal loading direction	1
$\underset{\approx}{M}$	Second-order unit tensor in the direction of the yield surface gradient	1
$\underset{\sim}{n}$	Unit orientation for a crack	1
N	Kayenta model internal state variable	1
N_i	Number of cracks of size *"i"* and orientation $\underset{\sim}{n}$ in the volume	Number of cracks
N_V	Number of cracks per unit volume	Number of cracks/m^3
$\underset{\approx}{N}$	Unit normal to the yield surface	1
$\underset{\sim}{o}$	Unit vector defined in the x_1 - x_2 plane for a unit sphere	1
p	Joint probability density	1
p_{ave}	Mean stress	Pa
p_i	Fraction of the total cracks having size a_i	1
P^{bath}	Compressive hydrostatic bath pressure	Pa
$\underset{\approx\approx}{P}^{symdev}$	Symmetric-deviatoric projector	1
r	Radial coordinate	m
s	$s = \sin\theta$	1
$\underset{\approx}{s}$	Second-order deviatoric stress tensor	Pa
$\underset{\approx\approx}{S}$	Fourth-order compliance tensor of the deformed material	Pa^{-1}
$\underset{\approx\approx}{S}_o$	Fourth-order compliance tensor of the underlying substrate matrix material	Pa^{-1}
t	Time	s
t_{End}	Time at which the TXC test ends	s
t_{TXC}	Time at which TXC leg starts	s
t_Y	Time at which the loading path intersects the yield surface	s
$\underset{\approx\approx}{T}$	Elastic-plastic tangent stiffness fourth-order tensor	Pa^{-1}

Symbol	Definition	Units (SI units)
X	Kayenta model variable	Pa
V	Representative volume	m^3
z	Axial coordinate	m
$\underset{\approx}{Z}$	Elastic-plastic second-order coupling tensor	Pa
$\underset{\approx}{\alpha}$	Back stress second-rank tensor	Pa
$\underset{\approx}{\alpha}^K$	Symmetric second-rank crack density tensor	1
$\tilde{\alpha}_i$	Coefficients defined as $\tilde{\alpha}_j(\theta)=\int_0^\infty h_j\left(a,\mu^o,\rho\right)q\left(a,\theta\right)da$	Pa^{-1}
$\Delta\tilde{\alpha}_3$	Compliance enhancement factor (CEF) $\Delta\tilde{\alpha}_3=\tilde{\alpha}_3-\tilde{\alpha}_{3o}$	Pa^{-1}
$\Delta\dot{\tilde{\alpha}}_3$	$d\Delta\tilde{\alpha}_3/dt$	$(Pa\cdot s)^{-1}$
β	Angle of inclination for Drucker-Prager criterion	Radians
$\underset{\approx\approx}{\beta}$	Fourth-rank crack density tensor	1
γ	Elastic constant arising from open and closed penny-shaped cracks	Pa^{-1}
δ_{ij}	Kronecker delta	1
$\underset{\approx}{\varepsilon}$	Total strain second-order tensor	1
$\underset{\approx}{\varepsilon}^e$	Elastic second-order strain tensor	1
$\underset{\approx}{\varepsilon}^p$	Plastic second-order strain tensor	1
ε_A	Axial strain	1
ε_A^e	Elastic axial strain	1
ε_A^p	Plastic axial strain	1
ε_L	Lateral strain	1
ε_L^e	Elastic lateral strain	1
ε_L^p	Plastic lateral strain	1
$\underset{\approx}{\dot{\varepsilon}}$	Total strain rate second-order tensor	s^{-1}
$\underset{\approx}{\dot{\varepsilon}}^e$	Elastic strain rate second-order tensor	s^{-1}
$\underset{\approx}{\dot{\varepsilon}}^p$	Plastic strain rate second-order tensor	s^{-1}

Symbol	Definition	Units (SI units)
η	Internal state variable	Units vary
θ	Inclination angle	1
$\bar{\theta}$	Lode angle	1
κ	Kayenta model internal state variable	Pa
$\dot{\lambda}$	Consistency parameter, magnitude of the plastic strain	s^{-1}
μ^o	Elastic properties of the substrate material	Units vary
ν_o	Poisson's ratio of the substrate material	1
$\underset{\approx}{\xi}$	Shifted stress second-order tensor	Pa
ρ	Number of cracks per unit mass	Number of cracks/kg
$\sigma_1, \sigma_2, \sigma_3$	Principal stresses	Pa
$\underset{\approx}{\sigma}$	Stress second-order tensor	Pa
$\underset{\approx}{\sigma}^*$	Evolved stress second-order tensor	Pa
$\underset{\approx}{\dot{\sigma}}$	Stress rate second-order tensor	Pa/s
σ_n	Normal component of the far-field traction	Pa
σ_A	Axial stress	Pa
σ_L	Lateral stress	Pa
σ_r	Radial stress	Pa
σ_z	Axial stress	Pa
σ_A^*	Modified axial stress, $\sigma_A^* = \sigma_A$	Pa
σ_L^*	Modified lateral stress, $\sigma_L^* = \sqrt{2}\sigma_L$	Pa
τ	Signed equivalent shear stress	Pa
φ	Azimuth angle	1
$\Delta \underset{\approxeq}{S}$	Fourth-order change in compliance tensor	Pa^{-1}
$\Delta\Psi$	Solid angle on the unit sphere	1
Ω	Solid angle surface	1

Function List

Symbol	Function
$\underset{\approx}{\tilde{B}_I}(\ )$	$\underset{\approx}{\tilde{B}_I}(\theta)=\frac{1}{2\pi}\int_0^{2\pi}\underset{\approx}{B_I}\left(\underset{\sim}{n}(\varphi,\theta)\right)d\varphi$
$dev(\ )$	Function that returns the deviatoric component
$f(\ )$	Yield function, can be either isotropic or anisotropic
$f_o(\ )$	Yield function for the initial state of consideration (can be undamaged state)
$f_c(\ )$	Kayenta cap function
$f_f(\ )$	Kayenta fracture function
$F(\ )$	Yield function, specified to be isotropic
$F_c(\ )$	Kayenta model-specific function
$F_f(\ )$	Kayenta model-specific function
$g(\ )$	Yield function based on a critical strain
$h'(\ )$	Tsai-Wu yield function, specified to be anisotropic
$H[\ ]$	Heaviside function
$iso(\ )$	Function that returns the isotropic component
$n(\ )$	Number density-distribution function
$p(\ )$	Probability distribution function
$q(\ )$	Distribution function with a restricted inclination angle
$p(\ )$	Probability distribution function
$\mathrm{sgn}(\ )$	Signum operator
$tr(\ )$	Function returns the trace
$\tilde{\alpha}_j(\ )$	$\tilde{\alpha}_j(\theta)=\int_0^{\infty}h_j\left(a,\mu^o,\rho\right)q(a,\theta)\,da$
$\beta_{ij}(\ )$	Coefficient functions
$\delta(\ )$	Dirac delta function
$\Gamma(\ )$	Kayenta model-specific function
$\Pi(\ )$	Crack size distribution function
$\langle\ \rangle$	Macauley brackets

1. INTRODUCTION OF THE KAYENTA CAP EVOLUTION MODEL

Macroscale constitutive models typically have more than one internal state variable (ISV), (e.g., porosity and matrix strength of a porous metal), but macroscale testing involves all ISVs changing at once, making it literally impossible to infer ISV evolution laws from macroscale data. All that is measurable is the "ensemble" hardening modulus.

This leads to modeling uncertainty of what are appropriate ISVs and corresponding evolution laws, which is a major issue motivating mesoscale modeling. This thesis is concerned with the phenomenon of dilatation in triaxial compression of porous media. Such dilatation has been modeled very accurately by Warren, Fossum, and Frew [1]. This is also the cap model used in the Kayenta geomechanics code and will henceforth be referred to as the Kayenta model. This cap evolution law assumes an isotropic yield model with a porosity-related ISV that evolves in a way that gives compaction followed by dilatation in triaxial compression (TXC), but it does so by unrealistically evolving the hydrostatic strength (determined from the evolving porosity ISV). Specifically, to get such an excellent fit to TXC dilatation data, Kayenta predicts an increase in hydrostatic compressive strength when dilatation is occurring. This work aims to explore an alternative model for TXC dilatation based on allowing induced elastic anisotropy with no increase in hydrostatic strength.

By showing that two fundamentally different models are capable of describing limited (TXC) data, modeling uncertainty is exposed for any other loading mode following the TXC leg. Ideally, this work will encourage mesoscale studies to help identify physics-based ISVs and their evolution laws, especially under changes in loading direction.

Overall, our motivation is that materials reach stress states in engineering applications that are not close to stress states in controlled calibration tests, meaning that the models are being used in unvalidated domains. Additionally, actual lab testing will almost always induce more than one ISV to change at a time, making it impossible to identify individual terms in the definition of the ensemble hardening modulus. This uncertainty can be investigated using in silico (virtual) testing where it is possible to suppress evolution of ISVs, and where the material state can be returned to the initial state to investigate material response to a realistic variety of loading directions.

This thesis discusses the cap evolution law as written in Kayenta, reports on a literature review of the topic, and finally reports on an alternative approach that can be incorporated into the Kayenta model. The intent of this approach is to introduce an alternative way to fit triaxial compression data without resulting in counterintuitive changes to the hydrostatic response.

This work is divided into following sections:

1. Section 0 presents a guide to the cap evolution model in Kayenta.
2. Section 2 documents a literature review that discusses the following subtopics:

- Experimental evidence supporting the cap evolution law currently in Kayenta.
- Examination of experimental data that researches the effect of nonmonotonic loading on the elastic limit.
- Other research efforts that model the cap behavior.
- Experimental evidence of inelastic induced anisotropy resulting from triaxial compression.

3. Section 3 discusses an alternative approach for modifying an isotropic yield function.
4. Section 4 demonstrates the use of a distortion operator in elastic/plastic analysis.
5. Section 5 is the conclusion and summarizes the major points of the thesis.

1.1 Notation

Throughout this work, mathematical notation will follow the notational conventions set forth in the Kayenta manual [2]. A notation used in the Kayenta manual is to underline vectors and tensors. Scalars, vectors, and tensors will be "underlined" according to their order. So vectors will be written as $\underset{\sim}{x}$, second-order tensors as $\underset{\approx}{\sigma}$, fourth-order tensors as $\underset{\approx\!\approx}{E}$, etc. The following definitions for vector and tensor analysis are employed:

- Definition of over bar: $\bar{x} \equiv -x$.
- Dot product between two vectors: $\underset{\sim}{u} \cdot \underset{\sim}{v}$ is $u_k v_k = u_1 v_1 + u_2 v_2 + u_3 v_3$.
- Vector-to-vector linear transformation; $\underset{\sim}{u} = \underset{\approx}{A} \cdot \underset{\sim}{v}$ is $u_i = A_{ij} v_j$.
- Dot product between a tensor and a tensor: $\underset{\approx}{C} = \underset{\approx}{A} \cdot \underset{\approx}{B}$ or $C_{ij} = A_{ik} B_{kj}$.
- Tensor-to-tensor linear transformation: $\underset{\approx}{X} = \underset{\approx\!\approx}{E} : \underset{\approx}{Y}$ is $X_{ij} = E_{ijkl} Y_{kl}$.
- Kronecker Delta: $\delta_{ij} = 1$ if $i = j$; or $\delta_{ij} = 0$ if $i \neq j$.
- Identity tensor: $\underset{\approx}{I}$ is the tensor whose ij components are δ_{ij}.
- Inner product between two tensors: $\underset{\approx}{A} : \underset{\approx}{B}$ or $A_{ij} B_{ij}$.
- Magnitude of a vector: $\sqrt{\underset{\sim}{v} \cdot \underset{\sim}{v}}$ is $\sqrt{v_k v_k} = \sqrt{\sum_{k=1}^{3} v_k^2}$.
- Magnitude of a tensor: $\sqrt{\underset{\approx}{A} : \underset{\approx}{A}}$ is $\sqrt{A_{ij} A_{ij}} = \sqrt{\sum_{i=1}^{3} \sum_{j=1}^{3} A_{ij}^2}$.
- Trace of a tensor: $tr\,\underset{\approx}{A}$ is $A_{kk} = A_{11} + A_{22} + A_{33}$.
- Deviatoric part of a tensor, $dev\left(\underset{\approx}{A}\right)$ is $dev\left(A_{ij}\right) = A_{ij} - \frac{1}{3} A_{kk} \delta_{ij}$.

Additionally,

- Second-order tensors are symmetric; $\sigma_{ij} = \sigma_{ji}$.

- The elastic stiffness tensor is major symmetric; $C_{ijkl} = C_{klij}$.
- Other fourth order tensors are minor-symmetric; $C_{ijkl} = C_{jikl} = C_{ijlk}$.

Other symbols and functions in this thesis are defined in Appendix A.

1.2 Kayenta Yield Surface

This subsection of the document gives a brief review of the Kayenta model, and how it pertains to this project. Parts of this section may directly quote or paraphrase statements or use figures and/or equations from the Kayenta manual [2], which is a public-domain document.

The Kayenta model prescribes that there exists a convex contiguous elastic domain of stress states for which any deformation would be constrained within the elastic limit. The boundary of the elastic domain is called the yield surface. The yield criterion can be expressed as an isotropic yield function, $f(\sigma_1, \sigma_2, \sigma_3) = 0$, in terms of the three principal stresses, σ_i (note: the yield function can be written in terms of other stress invariants). The isotropic assumption of Kayenta implies that the yield surface in six dimensions can be visualized in three dimensions (Haigh–Westergaard stress space). Viewing the yield surface through different cross sections gives insight into the yield surface. A very important line associated with the yield surface is the hydrostatic axis for which all three principal stresses are equal. Any plane that contains the hydrostatic axis is called a meridional plane. An octahedral plane is any plane perpendicular to the hydrostatic axis. Further defined is an octahedral profile, which is a cross section of the yield surface defined by an octahedral plane [2].

As previously mentioned, the yield criterion defines the elastic limits of a material under combined states of stress. The yield function can additionally depend on internal state variables (ISV) that affect the material's physical properties (e.g., porosity, density, etc.). The yield surface is not necessarily fixed in stress space, and its location will change by changing the internal state variables (e.g., hardening, plastic deformation, pore collapse, etc.). In additional to a yield surface, a limit surface is often defined, which is the boundary of possible stress states achievable by any means (elastic or plastic). Stress states outside of the limit surface are not achievable by any quasistatic process.

In the nondamaging version of Kayenta, the limit surface is considered fixed, and it contains all attainable stress states. By definition, the yield surface is contained within the limit surface. The material can have an infinite number of yield surfaces but has only one limit surface. One constraint on the limit surface is that it will always be an open convex set. When damage is allowed, the limit surface can collapse, meaning that initially attainable stress states may not be attainable more than once.

1.3 Stress Invariants

To ease the illustration of the yield and limit surfaces, new quantities are introduced. The stress deviator, s_{ij}, is the deviatoric part of the stress, defined as

$$s_{ij} = \sigma_{ij} - \frac{1}{3}\left(tr\left(\sigma_{kk}\right)\right)\delta_{ij} \tag{1}$$

Conceptually, the stress deviator is a tensor measure of shear stress. Also introduced are the stress invariants, I_1, J_2, and J_3. These quantities are the same no matter which orthonormal basis is used for the stress components.

$$I_1 = tr\left(\sigma_{ij}\right) = \sigma_1 + \sigma_2 + \sigma_3 \tag{2}$$

$$J_2 = \frac{1}{2}tr\left(s_{ij}^2\right) = \frac{1}{2}\left(s_1^2 + s_2^2 + s_3^2\right) \tag{3}$$

$$J_3 = \frac{1}{3}tr\left(s_{ij}^3\right) = \frac{1}{3}\left(s_1^3 + s_2^3 + s_3^3\right) \tag{4}$$

Many descriptions of the limit surface make use of the stress invariants. Some additional terms are defined as

$$p_{ave} = \frac{I_1}{3} = \frac{\sigma_{kk}}{3} \tag{5}$$

where p_{ave} is the mean stress. Sometimes the negative of this term is defined as the pressure, in which case it is marked as $\overline{p}_{ave}$ where the over bar denotes a compressive stress.

1.3.1 Important Kayenta Stress States

These subsections contain details on important stress states that are used to parameterize Kayenta. From these stress states, Kayenta interpolates from the known stress states to general stress states.

1.3.2 Hydrostatic Loading

For this loading case, a hydrostatic pressure, $\overline{p}_{ave}$, is applied to the material. Note that the over bar indicates a negative stress. Expressed in tensor form, the hydrostatic loading is expressed as

$$\sigma_{ij} = \begin{bmatrix} \bar{p}_{ave} & 0 & 0 \\ 0 & \bar{p}_{ave} & 0 \\ 0 & 0 & \bar{p}_{ave} \end{bmatrix} \tag{6}$$

Kayenta uses data from hydrostatic loading to determine the bulk modulus, as well as the crush curve (also called consolidation curve) that governs the relationship between evolving porosity and applied pressure.

1.3.3 Triaxial Loading

The "triaxial" state, a term common to the geomechanics community, is very important to the material characterization of brittle materials. Though termed triaxial, there are two equal principal stresses (lateral stresses) and one axial principal stress. Expressed in matrix form, the stress components of this state are

$$\begin{bmatrix} \sigma_L & 0 & 0 \\ 0 & \sigma_L & 0 \\ 0 & 0 & \sigma_A \end{bmatrix} \tag{7}$$

where σ_A is the axial stress, and σ_L is the lateral stress.

The stress state is called triaxial compression (TXC) if the axial stress is more compressive than the lateral stress (i.e., recalling that stress is positive in tension, TXC corresponds to $\sigma_A < \sigma_L$). Triaxial compression testing is conducted with the axial stress being of greater compressive magnitude than the lateral stresses. Triaxial extension (TXE) corresponds to $\sigma_A > \sigma_L$ and is not associated with strain or deformation. The geomechanics community uses the word "extension" to indicate that, for typical isotropic materials, this TXE produces a shape change that increases the *ratio* of cylinder height to diameter even though height and diameter are both decreasing. **Figure 1** illustrates this loading setup (taken from Kayenta Manual [2]). Interestingly,

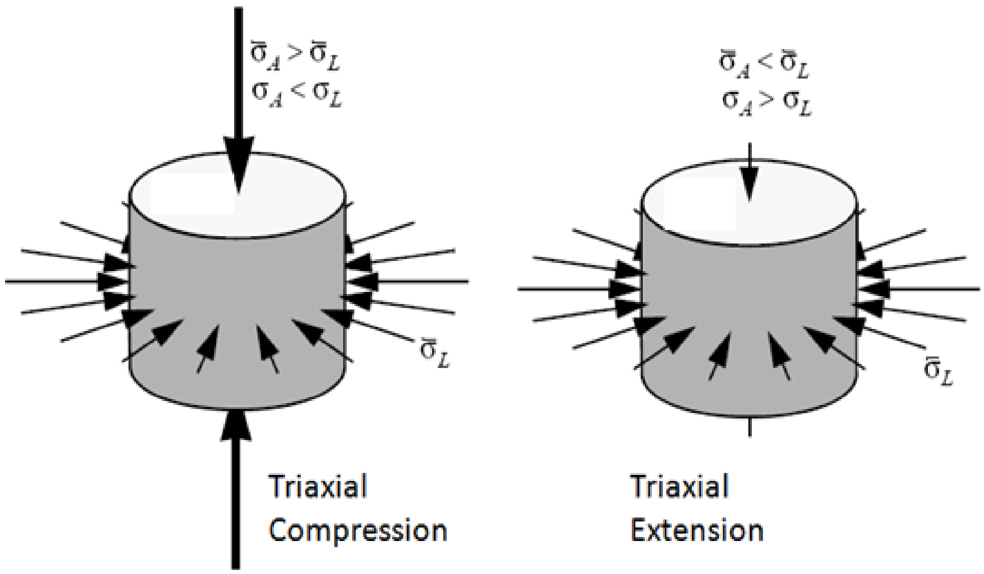

Figure 1. Illustration of triaxial compression (TXC) and triaxial extension (TXE). Strictly speaking, these terms refer exclusively to the stress state (not deformation). The ratio of cylinder height to cylinder diameter will typically decrease in TXC, but this ratio typically increases in TXE.

triaxial extension testing does not necessarily mean the axial stress is tensile, instead it is specified that the axial stress is less compressive than the lateral stress.

Using Equation (7), the deviatoric tensor for triaxial loading is expressed as

$$\frac{\sigma_A - \sigma_L}{3}\begin{bmatrix} -1 & 0 & 0 \\ 0 & -1 & 0 \\ 0 & 0 & 2 \end{bmatrix} \tag{8}$$

The stress invariants are

$$I_1 = \sigma_A + 2\sigma_L\,,\ J_2 = \frac{1}{3}\left(\sigma_A - \sigma_L\right)^2,\ J_3 = \frac{2}{27}\left(\sigma_A - \sigma_L\right)^3 \tag{9}$$

The signed equivalent shear stress for triaxial loading is

$$\tau = \frac{\sigma_A - \sigma_L}{\sqrt{3}} \tag{10}$$

As shown in **Figure 2**, the material is initially compressed hydrostatically to a pressure of $\overline{P}^{bath}$ ($\bar{I}_1 = 3\overline{P}^{bath}$). Then, the lateral stress is held constant ($\bar{\sigma}_L = \overline{P}^{bath}$) as the axial stress is compressed further.

1.4 Lode Coordinates

Lode coordinates provide an alternative way of viewing the yield surface. Normally, the stress space is expressed in terms of the principal stresses ($\sigma_1, \sigma_2, \sigma_3$). The Lode coordinate system replaces the Cartesian coordinate system with cylindrical coordinates expressed as $\left(r, \bar{\theta}, z\right)$. This is a reasonable choice because an isotropic yield function has 120° rotational symmetry about the hydrostatic direction and reflective symmetry about the triaxial extension and triaxial compression axes when viewed down the hydrostatic direction (called an octahedral plane). An additional advantage of Lode coordinates system is that they may be expressed in terms of stress invariants.

Illustrations of the Lode coordinate system are shown in Figure 3 (taken from Kayenta Manual [2]). Figure 3(a) is a meridional yield profile, and Figure 3(b) is an octahedral yield profile. The distorted view in the octahedral profile results because brittle materials are weaker in tension when compared to compression.

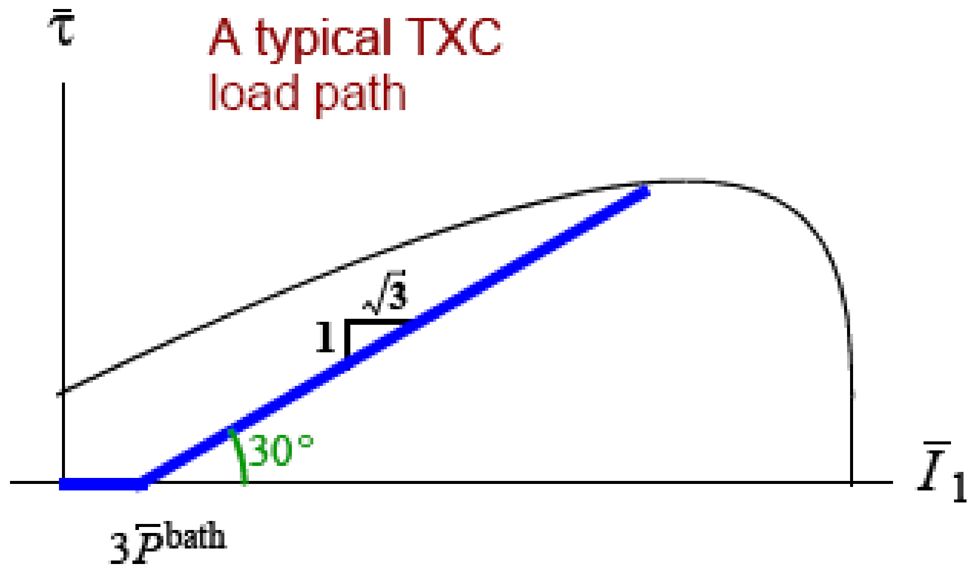

Figure 2. Diagram of a triaxial compression load path in $\bar{\tau}$ vs. $\bar{I}_1$ space. Here, $\bar{P}^{\text{bath}}$ is the initial hydrostatic compressive stress, and it is then the lateral stress value (typically supplied by a fluid bath) after the triaxial phase begins.

The descriptions of the individual components of the coordinate system are:

- $r = \sqrt{2J_2}$; The radial r coordinate equals the magnitude of the stress deviator.
- $\sin 3\bar{\theta} = -\frac{J_3}{2}\left(\frac{3}{J_2}\right)^{\frac{3}{2}}$; The Lode angle $\bar{\theta}$ is the angular coordinate of the stress state as illustrated in Figure 3(b), and it varies monotonically as the middle eigenvalue transitions from the far left side of the three-dimensional Mohr's circle to the far right side. Specifically, it is defined to be zero in shear, and can vary in value from -30° in triaxial extension to +30° in triaxial compression. The bar is placed over the θ symbol to ensure that $\bar{\theta}$ will be positive in triaxial compression and negative in triaxial extension.

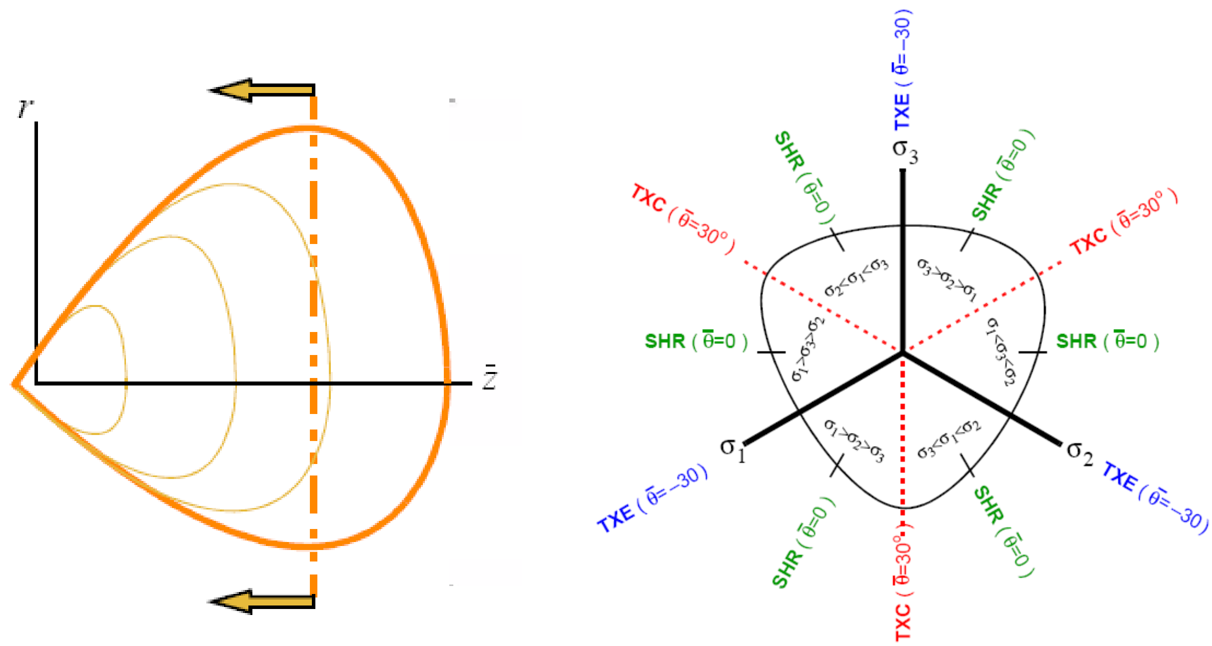

(a) (b)

Figure 3. Illustration of isotropic hardening of an isotropic yield surface; (a) meridional yield profile of the yield surface at a variety of porosities, (b) octahedral profile.

- $z = I_1 / \sqrt{3}$; The z-coordinate is the projection of the stress onto the hydrostatic axis, and the $\sqrt{3}$ term appears because the magnitude of the hydrostatic axis $[111]$ is $\sqrt{3}$. The z-coordinate will normally be used as $\bar{z} = -z$, because most of the yield surface resides in the compressive domain.

1.5 Kayenta Plasticity Theory

The total strain rate, $\dot{\varepsilon}_{ij}$, is separated into an elastic and plastic component as $\dot{\varepsilon}_{ij} = \dot{\varepsilon}^e_{ij} + \dot{\varepsilon}^p_{ij}$ where $\dot{\varepsilon}^e_{ij}$ is the elastic strain rate, $\dot{\varepsilon}^p_{ij}$ is the plastic strain rate, and where the superimposed dot denotes a rate.

Focusing on only the elastic component of the total strain prior to the onset of inelastic loading, the stress rate, $\dot{\sigma}_{ij}$, can be written as

$$\dot{\sigma}_{ij} = C_{ijkl} \dot{\varepsilon}^e_{ij} \tag{11}$$

where C_{ijkl} is the elastic tangent stiffness tensor. In the case when C_{ijkl} is isotropic, the fourth-order tensor is characterized by two material constants (e.g., shear modulus and bulk modulus). A novel aspect of the work in this thesis will be to allow the elastic stiffness to evolve in response to inelastic loading, which will require a revision of Equation (11) to include the rate of stiffness.

1.5.1 Elastic Yield Surface

To begin each time step, Kayenta evaluates a tentative prediction of the updated state corresponding to an assumption that the loading is elastic. If the resulting “trial elastic stress” [2] is within or on the yield surface, the actual stress is set equal to the trial elastic stress. However, if the solution lies outside the yield surface then the assumption of elastic response is incorrect, and the time step is solved again using inelastic governing equations.

The elastic limit used by Kayenta is a phenomenological fit of all mechanisms that lead to inelastic yielding. As long as the stress is inside or on the yield surface, elasticity equations are used. If the stress is outside the yield surface, then plasticity equations are used.

The Kayenta yield function is

$$f\left(\sigma_{ij},\alpha_{ij},\kappa\right)=J_2^{\xi}\Gamma^2\left(\bar{\theta}^{\xi}\right)-\left[F_f\left(I_1\right)-N\right]^2 F_c\left(I_1,\kappa\right) \tag{12}$$

where α_{ij} is the backstress and is a stress tensor-valued ISV about which the yield surface is centered. The following paragraph from page 32 of the Kayenta manual [2] describes the yield function shown in Equation (12):

> Briefly, the yield *function* f is defined such that elastic states satisfy $f<0$. The yield *criterion* corresponds to $f=0$. The "building block" function F_f and Γ are used to describe the elastic limit caused by the presence of microcracks, whereas the function F_c accounts for strength reduction by porosity. The function F_f represents the ultimate limit on the amount of shear the material can support in the absence of pores (i.e., F_f represents the softening initiation limit threshold resulting exclusively from microcracks). The material parameter N characterizes the maximum allowed translation of the yield surface when kinematic hardening is enabled, in which case J_2^{ξ} is the second invariant of the *shifted* stress tensor $\xi_{ij}=S_{ij}-\alpha_{ij}$, where α_{ij} is the backstress. When kinematic hardening is disabled (i.e., when N is specified to be zero), the backstress will be zero and therefore J_2^{ξ} would be simply the invariant of the stress deviator. The function F_f describes the limit strength, whereas F_f-N defines the *yield* threshold associated with cracks, which can evolve toward the limit surface via kinematic. The function $\Gamma\left(\bar{\theta}^{\xi}\right)$, where $\bar{\theta}^{\xi}$ is the Lode angle of the shifted stress, is used to account for differences in material strength in triaxial extension and

triaxial compression. By appearing as a multiple of $\left[F_f - N\right]^2$, the function F_c accommodates material weakening cause by porosity. The function F_c depends on an internal state variable κ whose value controls the hydrostatic elastic limit.

The functions F_f and F_c describe the elastic limit caused by the presence of microcracks. The other parameters of the yield surface are well demonstrated by examining an octahedral plane as shown in Figure 3(b). The $\Gamma\left(\bar{\theta}^{\xi}\right)$ function defines the shape of the octahedral profile. Since this research aims to demonstrate that induced anisotropy can allow dilation in triaxial compression without unrealistic cap motion, it is assumed that $\Gamma\left(\bar{\theta}^{\xi}\right)=1$. The size of the octahedral profile is controlled by the functions F_f and F_c.

1.5.2 Cap Function as a Combination of Porosity and Microcracks

Kayenta defines its cap function according to two underlying mechanisms: porosity and microcracks. Theoretical analyses typically focus on the effects of one of these mechanisms at a time; the Kayenta model combines basic features from both failure mechanisms into one model as shown in Figure 4 (taken from the Kayenta manual [2]). Figure 4(a) shows the shape of the meridional profile when only porosity is considered. Figure 4(b) shows a qualitative meridian that considers only the influence of microcracks without porosity. Note that the compressive fracture strength increases monotonically as the pressure is increased in Figure 4(b). This is because an increase in pressure causes additional friction at the crack faces, and less of the shear load has to be supported by the pore-free bulk material. Figure 4(c) shows the combined qualitative effects from porosity and microcracks. To obtain a combined model, Kayenta multiplies the individual porosity and microcrack profiles and scales the ordinate appropriately to match data.

The shape of the combined effects (microcracks and porosity) are continuously differentiable, which makes it both well suited for reproducing observed data and numerically well based. By multiplying the individual crack and porosity functions, Kayenta's combined TXC profile is defined as

$$\sqrt{J_2^{\xi}} = f_f\left(\bar{I}_1\right) f_c\left(\bar{I}_1\right) \qquad (13)$$

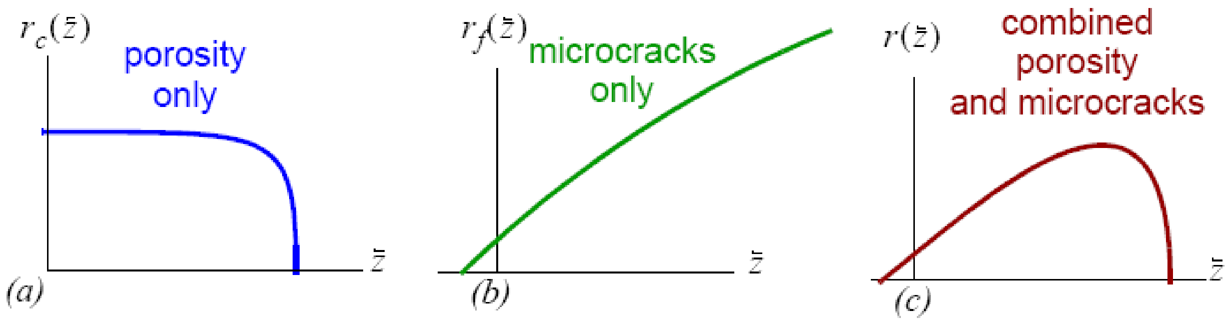

Figure 4. Qualitative meridional profile shapes**:** (a) porosity only, (b) microcracks only, and (c) combined porosity and microcracks.

where f_f is the fracture function and f_c is the cap function. Equation (13) is comparable to Equation (12) in that $f_f = F_f - N$ and $f_c = \sqrt{F_c}$.

1.5.3 The Cap Function

The cap function accounts for irreversible changes in volumetric strain resulting from compressive loading. The irreversible volumetric changes can occur in a porous medium even if the matrix material is not compressible. Kayenta provides a phenomenological fit of this event (plastic volume changes) and does not try to explicitly model the underlying physical mechanisms. The cap function, f_c, fits the volume changes by defining where the yield function intersects the $\bar{I}_1$ axis in compression, as illustrated in Figure 5.

The branch point $\bar{\kappa}$ marks the boundary between the constant and elliptical portions of f_c as shown in **Figure 5**.

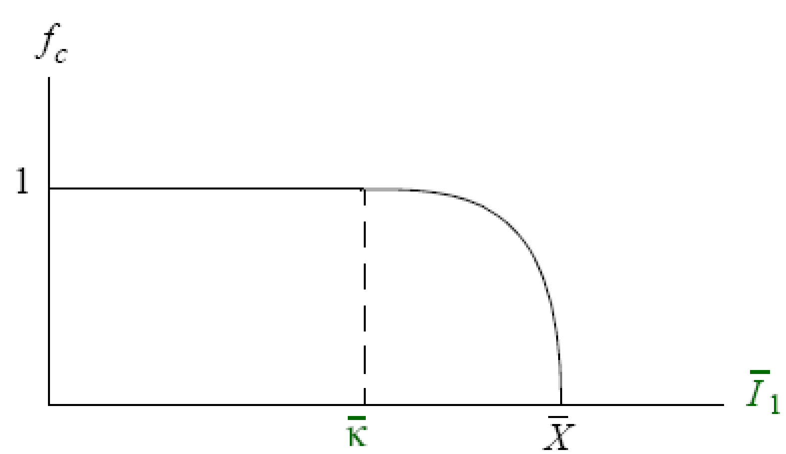

Figure 5. Cap function that accounts for the presence of pores.

$$F_c = f_c^2\left(\bar{I}_1,\kappa\right) = \begin{cases} 1 & \text{if} \quad \bar{I}_1 < \bar{\kappa} \\ 1-\left(\dfrac{\bar{I}_1-\bar{\kappa}}{\bar{X}-\bar{\kappa}}\right)^2 & \text{otherwise} \end{cases} \tag{14}$$

where $\bar{\kappa}$ and $\bar{X}$ are defined in **Figure 5**. Both $\bar{\kappa}$ and $\bar{X}$ increase as pores are eliminated in response to pressure increases. Within Kayenta, $\bar{\kappa}$ is treated as an internal variable, and $\bar{X}$ is calculated to preserve eccentricity of the ellipse and to match similar behavior predicted by idealized pore collapse models. The F_c function defined in Equation (12) is defined in terms of f_c as

$$F_c = f_c^2 \tag{15}$$

1.5.4 Meridional Shear Limiter Function

Following common terminology in the geomechanics community, the term “yield” is broadened to refer to any form of inelasticity, and the “yield surface” is the boundary of elastically attainable stress states. The term “limit stress” refers to the onset of softening, and the “limit surface” is the boundary of attainable states. Accordingly, the set of all possible yield surfaces must reside within the limit surface. Reaching a state on the limit surface generally requires a hardening process that evolves the yield surface out to the limit surface, after which a softening process commences by allowing the limit surface to collapse. The fracture function, f_f, is identical to the yield function if the material has microcracks and no porosity. As in the cap function, the fracture function is a phenomenological fit of available experimental data. The Kayenta manual describes some observed behavior of brittle materials, which are briefly summarized here:

- For a given mean stress, inelasticity in triaxial extension occurs at a lower stress than in triaxial compression. This gives rise to a third invariant dependence in the yield function. Brittle materials are weak in tension. The implication is that the meridional yield profile will include few if any tensile stress states.
- If brittle fracture is the only failure mechanism, the material strength will increase monotonically with increasing pressure, which corresponds to an ever-expanding cone-like shape for the yield surface. From Equation (12), the function $F_f\left(I_1\right)-N$ defines how the shear stress limit varies with pressure for a nonporous, but microcracked material in its virgin state. The meridional yield profile is

$$f_f\left(I_1\right) = F_f\left(I_1\right) - N \tag{16}$$

- The user-specified shift parameter, N, helps define the zero pressure intercept on the $\sqrt{J_2^{\xi}}$ axis. This is shown in Figure 6 (taken from the Kayenta Manual [2]).

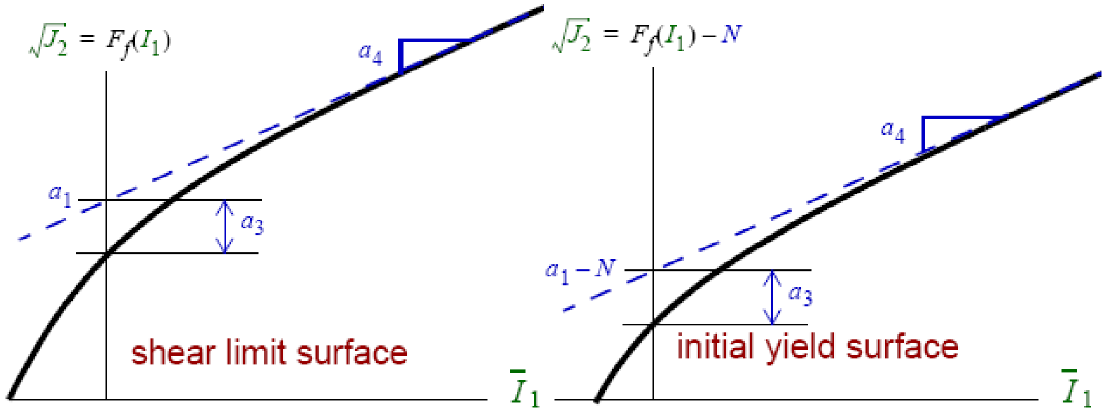

Figure 6. Shear limit function, unshifted and shifted.

The parameter N sets the value to which the yield function is permitted to translate under kinematic hardening. The function F_f is the limit envelope, beyond which stresses can never be reached quasistatically.

1.5.5 Cap Curvature Branch Point

The branch point in the yield function is of particular interest to this project. As previously mentioned, the yield function is constructed by multiplying the yield function, f_f, and the cap porosity function f_c. As illustrated in **Figure 7** (taken from the Kayenta manual [2]), the branch point is defined by the $\bar{\kappa}$ intercept on the $\bar{I}_1$ axis. For $\bar{I}_1$ values larger than $\bar{\kappa}$, the yield function is influenced by the cap function. The yield function is still dominated by shear cracking, resulting in plastic dilatation. Between the peak and the hydrostatic limit point $\bar{X}$, porosity dominates the material response, resulting in plastic volume compaction from pore collapse.

Most two-surface models construct and evolve the yield function according to a ratio (A/B), which is typically smaller than unity (see **Figure 7**). Kayenta constructs and

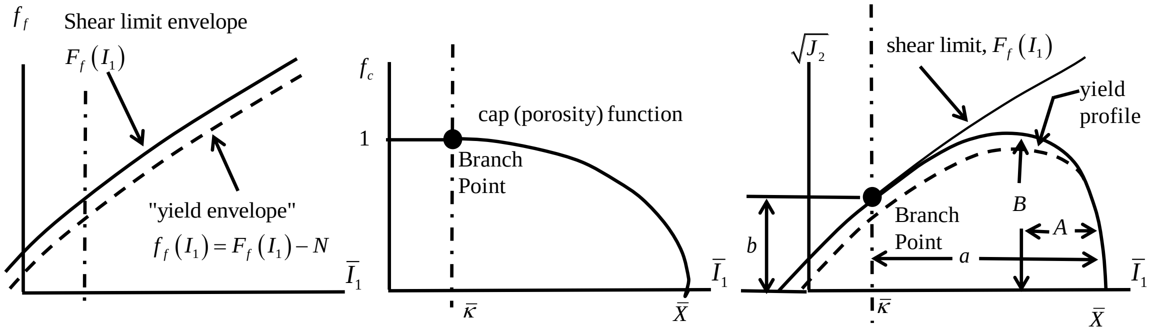

Figure 7. Yield function branch point. The black-dashed line in the figure represents equivalent values of $\bar{I}_1$.

evolves the yield function according to the ratio a/b, which is typically larger than unity. Kayenta defines a user-specified constant known as the cap eccentricity equal to a/b that can be used to help define the hydrostatic limit point.

The cap model currently used in Kayenta does an excellent job of fitting TXC data as shown in **Figure 8**. The situation becomes more interesting when the yield profile has not yet reached the shear limit, $F_f(I_1)$. Consider the load profile, shown in **Figure 9**,

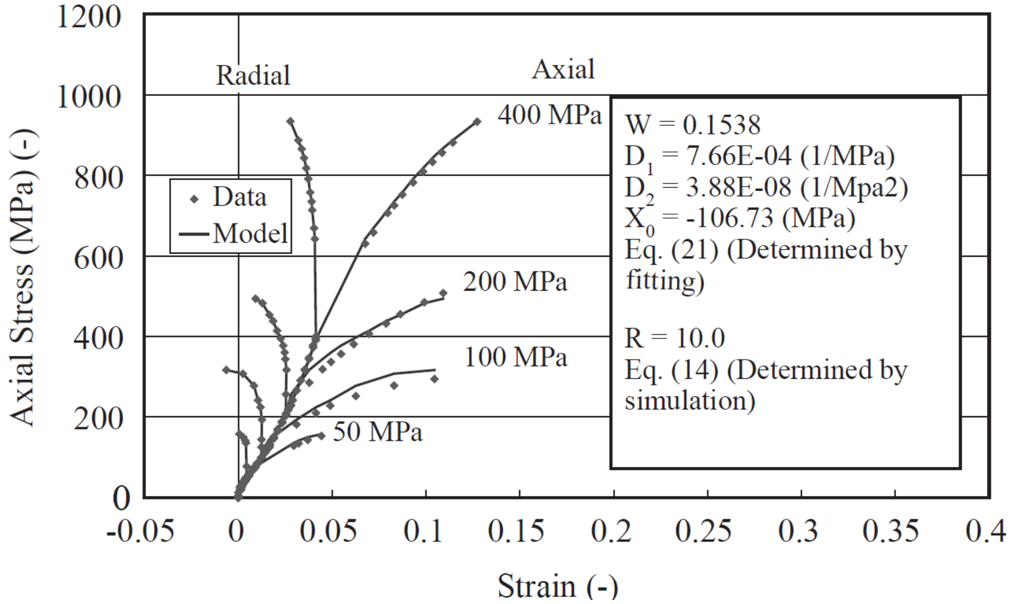

Figure 8. Plot of TXC data along with mathematical fit generated by the Kayenta model [1].

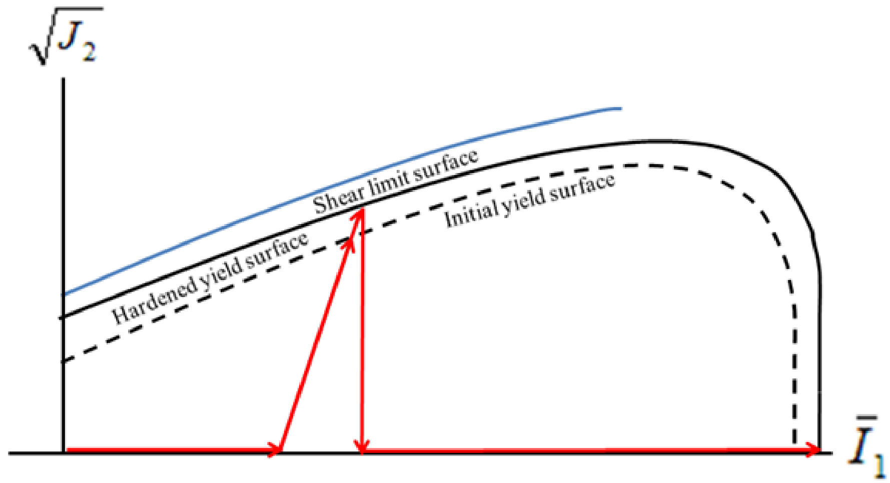

Figure 9. Loading profile for expansion of the yield surface with subsequent hardening resulting from dilatation.

that starts with hydrostatic loading but does not exceed the peak of the yield profile.

Additional loading then commences with the lateral stress being held constant, and the axial stress varying. This results in dilatation and expansion of the yield surface until the shear limit is reached. If the load profile is then changed so that the shear component of the stress is again zero, a new load profile can be introduced so that the compaction side of the yield profile is encountered.

However, this is problematic. By expanding the original yield surface, more pores are introduced by dilatation according to the Kayenta model. Yet, the current evolution model in Kayenta then predicts additional hydrostatic loading becoming more difficult because of the addition of pores.

This is highly counter intuitive as it is difficult to conceive how the addition of pores can effectively stiffen the material by making it more difficult to compact the material. As discussed in Section 2, no experimental data exist (to our knowledge) to validate this hardening model.

The remainder of this document deals with a literature review of triaxial compression and then concludes with an approach for altering the Kayenta cap model to predict dilatation in triaxial compression without causing a counterintuitive hydrostatic strengthening.

2. LITERATURE REVIEW

This literature review focuses on determining if any experimental evidence to support the Kayenta cap model is available. The following subtopics are discussed:

- Experimental evidence supporting the cap evolution law currently in Kayenta.
- Other modeling efforts that duplicate the cap model.
- Experimental evidence of inelastically induced anisotropy resulting from triaxial compression, and modeling that incorporates anisotropy.
- Mesoscale modeling that analyzes yield surfaces.

2.1 Evidence Supporting the Kayenta Cap Evolution Law

To provide experimental evidence supporting or contradicting the Kayenta cap evolution law, triaxial compression tests would have to be conducted so that dilatation is induced without causing sample failure. By unloading from a partially dilatated state, an experiment could then probe for the location of the hydrostatic elastic limit (see **Figure 9**) by hydrostatically loading until compaction is caused. In the literature review, testing neither absolutely validated nor invalidated the Kayenta cap law, but many bodies of work exist that might address the issue of hardening under triaxial compression.

Much effort has been devoted in recent years to conducting conventional triaxial compression tests. A huge body of work in which a brittle material is tested under monotonic loading exists, and fit to a variety of phenomenological models (distinguished only by their predictions for noncalibration loading modes). Much of this material is not relevant to the problem presented in the previous section, but some mention will be made of more recent test efforts in the bibliography [3-11]. Another common nonmonotonic testing protocol reported in the literature is the triaxial cyclic test [12-14]. However, none of these tests appeared to yield useful information about the failure cap.

Today's modern instrumentation certainly allows for more complicated (nonmonotonic) stress paths. Kodaka et al. [15] describe a series of triaxial compression tests performed on diatomaceous mudstone using both a conventional triaxial test under drained conditions, and also a constant stress ratio test. They showed that a cap-shaped yield locus is clearly obtained from the triaxial tests. However, they did not try to expand the cap surface. They used a newly developed technique called PTV (particle tracking velocimetry) to measure the strain localization. After testing, they used X-ray CT scanning to observe that high-density regions corresponded to compaction bands.

Many authors describe new testing machines that allow for testing on multiple axes, instead of the standard axisymmetric triaxial test [16, 17]. However, evolution of the hydrostatic failure cap caused by nonhydrostatic loading does not appear to have yet been investigated in the laboratory. Wang and coworkers [18] developed a servo-controlled true triaxial (cubical) apparatus for evaluating the mechanical response of asphalt concrete under multiaxial stress states. The apparatus allows the testing of specimens along a wide range of stress paths and stress levels that are not achievable in a conventional uniaxial or cylindrical apparatus. They are able to test along a series of multistage stress paths that included triaxial compression, triaxial extension, simple shear, conventional triaxial compression, conventional triaxial extension, and cyclic conventional triaxial extension. The testing documented in this report did not include any testing to failure or yielding.

Reddy et al. [19] report developing a triaxial testing apparatus that is different from conventional axisymmetric triaxial testing apparatuses. Tests are performed on cemented sand along different stress paths, which included hydrostatic compression, conventional triaxial compression, and testing along different directions on octahedral planes. However, the testing did not map out yield surface of the cemented sand. It instead focused on the stress-strain and volumetric responses.

Other researchers have been rather active with regards to the topic of triaxial testing and materials modeling. They report triaxial testing, which includes conventional triaxial tests, triaxial tension (extension) tests and combined compression-tension triaxial tests [20, 21]. Other researchers have measured anisotropy in soil subjected to general stress states [22]. One group of authors has measured the effect of initial mean effective stress on the behavior of otherwise unconfined column samples. Tests are conducted using undrained (pores may contain trapped fluid) cyclic loading at several initial confining stresses but with the same stress ratios (proportional stress loading relative to the prestressed state). The results indicate that the stress path is not affected by changing the initial effective mean stress if the shear stress ratios remain the same [23].

Hattab and Hicher [24] conducted testing to characterize the dilatancy in clay in relation to the overconsolidation ratio (the highest stress experienced divided by the current stress). This phenomenon is investigated along a large range of loading paths, with a strong emphasis placed on constant mean stress paths, given that it is possible to measure the volumetric strain created by the sole deviatoric stress. They determined three different types of behavior for the specimen submitted to a deviatoric stress; no volume change, dilatancy, and contraction. They conducted testing to the limit of the maximum strength envelope. The experimental results are then compared to plastic flow theories. Finally, by measuring the plastic strain increment vectors along different stress paths in the (mean pressure vs. deviatoric stress) plane, they demonstrated that the uniqueness hypothesis of the plastic potential is not valid. The results could be explained by using two plastic strain mechanisms: a deviatoric one and an isotropic one.

Brannon and coworkers [25] attempted to run tests to experimentally validate the cap-hardening model used in Kayenta. Several loading profiles were undertaken, including one to match the loading profile shown in **Figure 9**. Attempts to perform such experiments were inconclusive.

In summary, a significant body of work that deals with monotonic loading of triaxial specimens is available, but very few experimental investigations have dealt with nonmonotonic loading, thus making the hardening evolution law in Kayenta (and models like it) essentially unvalidated.

2.1.1 Investigation of the Cap Evolution Model

The yield surface model in Kayenta is similar to other widely used yield/plastic models. The issue of cap evolution is not unique to Kayenta. To further explore the issue, a comparison of related models is presented in this section. For a history of the cap model, the reader is referred to an article by Sandler [26].

A number of authors have devised cap models based on two or more invariants. For example, Tong and Tuan [27] developed a viscoplastic approach based on a two-invariant inviscid cap model.

Most modern cap models are based on the work of Sandler et al. [28-30]. Their model uses two different and independent yielding functions; one proposed for the shear envelope and the other for compaction. Their functions usually result in a continuous but nonsmooth yield surface. The corner point at which the shear and compaction surfaces of nonsmooth cap models intersect is nondifferentiable. Hence, the plastic flow direction at the corner point is not unique, which leads to a difficulty for numerical integrations [31]. Several revisions to the Sandler model have been proposed. Liu and coathors [31] devised two methods for converting the Sandler and Rubin surface to a smooth model. They give two model examples to demonstrate the good performance of the approach. Ayden et al. [32] formulated a three invariant failure model with a compression cap as seen in Figure 10. It appears quite similar to the Kayenta model. As mentioned previously, the continuity of the yield/failure surface from dilatation to compaction is not included in all models. Issen [33] described a two-yield surface constitutive model, which predicted both the compaction and shear bands. The two yield surfaces account

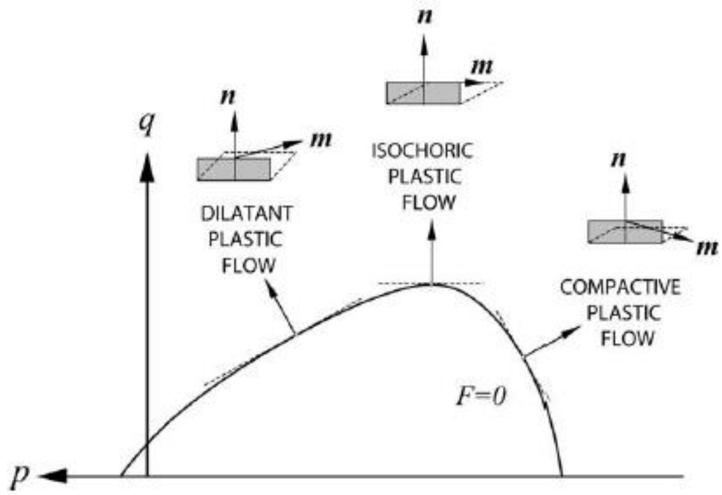

Figure 10. Representation of dilatant shear band, simple shear band, and compactive shear band [32].

for effects from the different deformation mechanisms and incorporate the effects into the model through independent increments of strain [34]. Liu et al. [35], also adopted a nonsmooth two-yield surface (**Figure 11**) based on a double elliptic strength criterion.

Khoei et al. [36] had some success developing a cap evolution model for cohesionless powders. Their work is based on a three-invariant cap plasticity model with an isotropic hardening rule. They presented a single-cap model with a continuous function that transitions from dilatancy to compaction. A plot of the model is shown in **Figure 12**. They presented a model for single-cap plasticity, which is comparable to double-surface plasticity models.

These failure surfaces and others have different approaches to the cap evolution law. However from the literature review of yield surfaces, no systematic study that investigated the effect of changing loading direction is found, especially changing from triaxial to hydrostatic stress conditions.

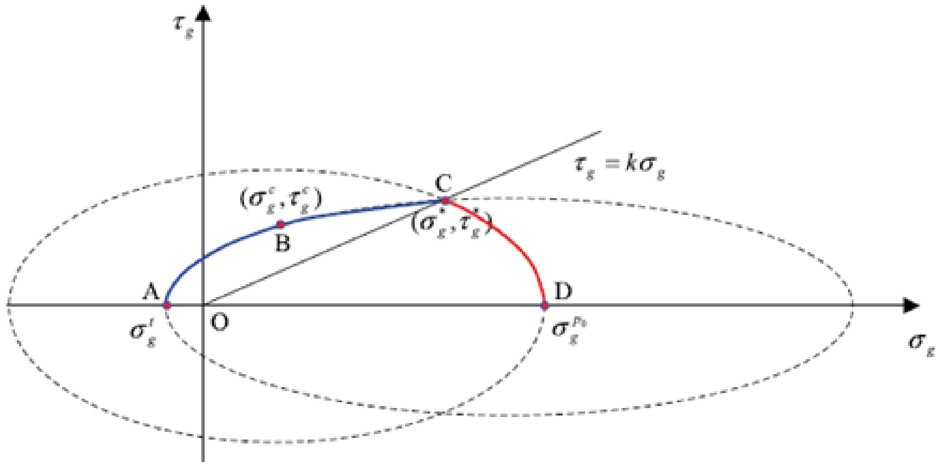

Figure 11. Double elliptic strength criterion by generalized shear and normal stress representation [35].

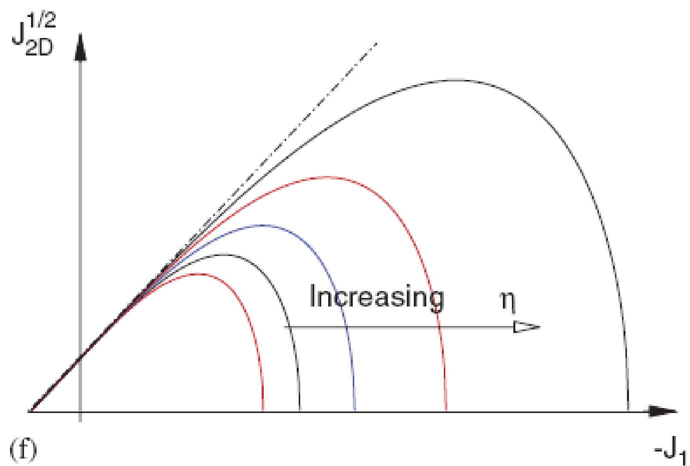

Figure 12. Yield surface of Khoei, A.R., et al. [36].

2.1.2 Inelastic Induced Anisotropy Resulting from TXC

The goal of this section is to explore the idea that inelastically induced anisotropy might be a viable means of modeling dilation in triaxial compression and without causing the material to become stronger in hydrostatic compression. A great number of anisotropic yield models exist and the following list details some of the approaches used by other researchers:

- Anisotropy is achieved through rotation of the yield surface around the origin of the stress space. The model is capable of describing the effects of stress anisotropy and stress reorientation in clays. [37].
- The anisotropic yield surface is achieved by incorporating distorted ellipsoids into the bounding surface and the yield surface to describe the evolution of structure and anisotropy [38-41].
- Another method proposed by Dean [42] deals with "patterns." This method assumes that soil fabric (arrangement, size, shape, and frequency of soil constituents, excluding pores) consists of elementary units called “patterns.” A model using these patterns is developed. In addition to elastic and plastic components, a third strain-increment component is deduced which helps explain nonassociated flow. The proposed method explains critical states, anisotropy, sensitivity, the Bauschinger effect, and swept-out memory.

Other authors use a similar approach [43-45]. The generation of anisotropic models or at least anisotropic capable models have become popular during the last decade and a half [46-49].

An additional approach to modeling anisotropy is to change the compliance in a particular direction in response to matrix (pore free bulk material) damage [50-53]. When brittle solids are subjected to compressive stress states, microcracks nucleate and grow as the stresses are increased. The microcracks generally grow from preexisting flaws, pores, or other discontinuities within the solid. The presence of microcavities and microcracks affects the effective or volume average elastic properties of the material. The formation and evolution of the microcrack damage cause a progressive loss of stiffness in the constitutive response of the material [54].

Experimentally, it has been determined (for brittle materials such as stone or ceramic) that the application of shear stress will induce anisotropy [55, 56]; with the result of loss of stiffness coincident with the axis of the major principal stress, the shear modulus degrades in a plane aligned parallel to the major principal stress axis. Essentially, under hydrostatic stress, the material can be described as being isotropic and the materials stiffness increases. However, when the material is subjected to shearing, the material becomes anisotropic and softens.

One publication reports loading [57] rock salt under triaxial compressive loading to establish the source mechanisms of microcracks. The induced failure cracks resulted primarily from mode I fracture mechanisms. These so-called extension fractures are well known from many triaxial compression tests [58, 59]. Fractures accumulate in zones of high shear stress, which form a cone of shear bands. In this highly damaged zone, the ultimate failure occurs by sliding along the shear bands as shown in **Figure 13**.

Similar observations were made by Sfer and coauthors [60] on triaxial compression tests of concrete. At zero or low confinement, distributed microcracking and several macrocracks are present. At high confinement, distributed cracking is not present (i.e., cracks are not randomly oriented), and failure occurs with the propagation of a few macrocracks. In general, the observed trends confirm and extend

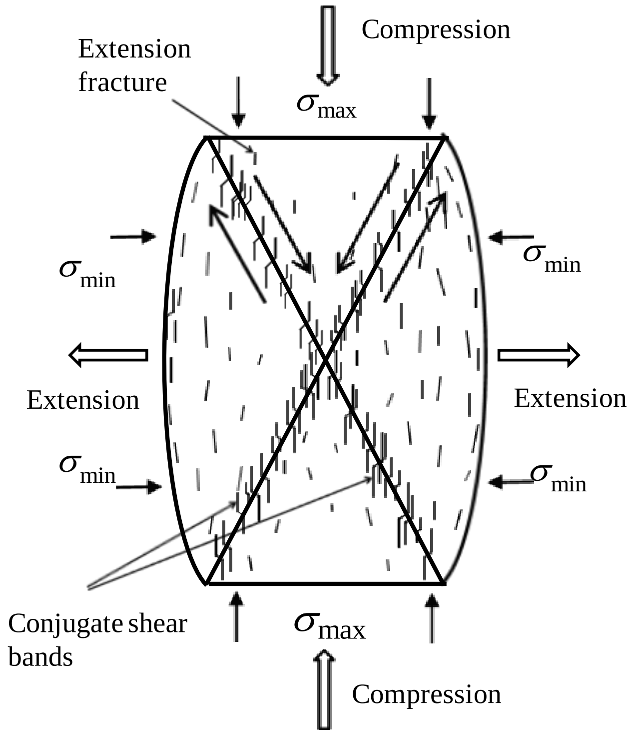

Figure 13. Damage and fracture development during failure of the rock salt specimen [57].

results previously reported in the literature. Optical microscopy shows extensive microcracking, especially in the aggregates, and pore collapse at high confinement.

On subsequent loading paths, existing cracks will significantly change the failure mechanism. This was observed by Lei and coworkers [61]. The authors tested two similar course-grained granite samples in triaxial compression. The main difference between the two rocks is that one of the granite sets contained large preexisting cracks, while the other was almost crack free. Using acoustic emission tomography, they demonstrated that preexisting cracks are the most dominant factor of all heterogeneities that govern the fault nucleation process. They also established that failure predictability is dependent on the preexisting crack density and orientation.

An interesting set of experiments is performed by Zhu et al. [62]. They performed triaxial extension tests (where both principal stresses are compressive, $0 > \sigma_A > \sigma_L$ and $0 < \bar{\sigma}_A < \bar{\sigma}_L$, not to be confused with triaxial tension where the axial stress is tensile) to investigate the influence of radial stress on porosity and permeability in three porous sandstones. The effective mean stresses are sufficiently high such that the samples failed by cataclastic flow, with development of strain hardening and shear-enhanced compaction. They inferred from the triaxial compression and extension data that stress can induce anisotropic permeability. Before the onset of shear-enhanced compaction, the reduction in permeability and in porosity is found to be primarily controlled by the effective mean stress, and stress-induced anisotropy is negligible. The authors found with the onset of shear-enhanced compaction and development of cataclastic flow, coupling of the deviatoric and hydrostatic stresses induced considerable permeability and porosity reduction aligned along the principal stress directions. Microstructural observations on the shear-compacted samples showed appreciable increase of grain crushing and pore collapse, which explains the overall decrease in permeability. The damage from grain crushing is highly anisotropic, with the stress-induced microcracks preferentially aligned (i.e., perpendicular to minimum tensile stress direction) with the maximum compressive principal stress direction. Because more microcrack conduits are available to focus the flow in this direction, the permeability is relatively enhanced along the maximum principal stress direction. This line of research implies that failure in triaxial loading conditions can lead to anisotropic damage. The important conclusion of this work is that pressure does not induce anisotropy. It requires a combination of pressure and shear stress.

From the publications review in this section, the following may be concluded:

- Triaxial compression can induce anisotropy due to damage formation.
- Cracks aligned or kinked into the direction of principal stress (i.e., crack perpendicular to the lowest principal stress direction (measured positive in tension) result from a combination of deviatoric and hydrostatic stresses.
- Hydrostatic pressure does not cause anisotropy.
- The presence of cracks, aligned along a principal direction, causes a reduction in compliance in the lateral directions. This effectively induces transverse anisotropy in the material (meaning a material property is unchanged when the undeformed material is rotated about the principal direction).

2.1.3 Mesoscale Modeling that Analyzes Yield Surfaces

As detailed in the previous section, triaxial compression can induce transverse anisotropy in brittle materials. Mesoscale modeling is one option that can be used to predict the yield/failure behavior of such materials. For the case of triaxial compression, mesoscopic modeling has been used successfully to predict failure surfaces [63, 64]. This section will demonstrate that mesoscopic modeling can be used to successfully model transverse anisotropic behavior.

Abelev et al. [65] developed an isotropic hardening model that is modified to include the effects of inherent cross anisotropy (having one axis of symmetry and is usually used when referencing granular materials). Based on the experimental results of cross-anisotropic sands in isotropic compression tests, the principal stress coordinate system is rotated such that the model operates isotropically within the rotated framework. The same rotation technique is then employed on the plastic potential and yield surface. Verification of the cross-anisotropic model is presented using comparisons of predictions with both experimental data and results from the hardening model. They stated the model is shown to capture the overall trends of the observed behavior of cross-anisotropic sand with reasonably good accuracy within the scatter of the test results.

In their abstract, Zhu and Hu [66] report the development of a homogenization-based constitutive model for the description of anisotropic damage by mesocracking. A Coulomb-type interfacial frictional sliding criterion at mesoscopic scale is used as the loading function, and a nonassociated flow rule is adopted in the determination of the evolution rate of friction-induced inelastic deformation. They report that their model has the ability to account for contributions to microcracking such as: nonlinear stress-strain relations, damage induced anisotropic behavior, coupling between damage and friction on crack surfaces, sensitivity of mechanical responses to confining pressures, volumetric dilation as well as effects due to total or partial closure of microcracks, etc. They also state that their model shows good prediction of experimental data (conventional triaxial compression tests on marble).

Kowalczyk and Ostrowska-Maciejewska [67] used mesoscale modeling to describe the behavior of a transversely isotropic material. They used an energy approach to describe the behavior of transverse isotropy. A reduced compliance tensor is presented, which represented a limit condition of the Maxwell-Huber-Mises condition. Similar work was conducted [68] in which the reduction in stiffness is described as a fourth-rank tensor in a Cartesian frame.

One group [69] described the main mechanism of failure for brittle materials as nucleation and growth of microcracks. They ascertained that a way to model anisotropic damage is to consider the influence of compliance/stiffness on the material. They conducted a numerical study of a growing mixed-mode internal crack in a unit cell. The model gives values for the elastic compliance tensor modified by damage as the crack grows. It demonstrated the evolution of the anisotropic damage and the evolution of the type of material symmetries. The evolution of the elasticity tensor showed that the damage associated with a growing elliptical crack changed the isotropic properties into orthotropic ones. The crack growth rotated the principal loading axes to align with the local coordinates of the crack.

Wimmer and Karr [70] used a fracture approach to model brittle, polycrystalline ice. Constitutive equations are based on the damage mechanics of elastic materials containing microcracks. For homogeneous deformation modes, microcrack growth from inhomogeneous defects caused changes in the average elastic compliance of the material. A system of constitutive equations is developed based on a combination of stress or strain ratios. Bifurcation approaches to nonlinear problems are used to determine the loss of uniqueness of particular equilibrium states. Failure criteria in terms of bifurcations of the constitutive paths are established by examining the properties of the evolving tangent stiffness tensor. The influence of lateral stresses is studied for biaxial stress states, and faulting is found to occur for moderate levels of lateral compressive stress and lateral tension.

Papanikolaou and Kappos [71] proposed a plasticity constitutive model that is based on the experimental data of 130 triaxial tests conducted on cylindrical specimens. In the model, damage is quantified by the volumetric expansion that builds up by propagation of microcracks that progressively lead to failure. Softening is modeled using a reduced compliance.

It is reemphasized that the presence of cavities and cracks is known to have first-order effects on the macroscale, continuum properties of elastic materials [54, 72, 73]. Changes in microstructure cause variation in the overall elastic compliance and stiffness, hence providing a source of nonlinearity to an otherwise linear elastic material. Several papers have presented methods for constructing the compliance tensor based on the presence of voids of various shapes [52, 74-77].

3. ALTERNATIVE APPROACH FOR EVOLVING A YIELD FUNCTION

This section discusses an alternative mechanism that can be incorporated into Kayenta to avoid the undesired changes in the hydrostatic elastic limit cause by triaxial dilatation. The proposed method is to examine whether inelastically induced anisotropy will give realistic predictions of dilatation in triaxial compression without increasing the hydrostatic strength. As shown previously, triaxial compression can lead to induced transverse isotropy because of development of axial cracking (i.e., formation of cracks whose normals are perpendicular to the primary loading direction). The proposed method adopts a modified failure surface that starts as an isotropic surface, but, as anisotropy is induced, the surface evolves to accommodate the changes in material behavior. A practical approach to add anisotropy is to use an anisotropically transformed stress in the isotropic yield model.

3.1 Modifications to Yield Surfaces

One of the earliest expressions for an isotropic yield criterion is the von Mises yield criterion [78]. It states that yielding begins when the octahedral shearing stress reaches a critical value, k, which can be expressed as

$$F\left(\underset{\approx}{\sigma}\right) = dev\left(\underset{\approx}{\sigma}\right) : dev\left(\underset{\approx}{\sigma}\right) - k^2 \qquad (17)$$

An illustration of other yield functions for isotropic and kinematic hardening (also a combination of both) is shown in **Figure 14**.

To accommodate additional anisotropy, Tsai and Wu made use of an anisotropic tensor in their description of the yield function. The Tsai-Wu failure model [79] was originally developed to describe composite materials, which have different strengths in tension and compression. The Tsai-Wu failure model expressed in Mandel notation is

$$h'\left(\underset{\approx}{\sigma}\right) = h_i'\sigma_i + h_{ij}'\sigma_i\sigma_j - 1 \qquad i, j = 1, 2, \ldots 6 \qquad (18)$$

where the h_i' and h_{ij}' are, respectively, second and fourth rank material property tensors. The equation parameters result from a fit of failure data, and are assumed without loss to be symmetric. The Tsai-Wu theory is a well-known example of a more general class of anisotropic plasticity theories in which an isotropic yield function is called using an affinely transformed stress.

In our case, the yield theory is written as

$$f\left(\underset{\approx}{\sigma}\right)=F\left[\underset{\underset{\sim}{\approx}}{L}:\left(\underset{\approx}{\sigma}-\underset{\approx}{\alpha}\right),\eta_1,\eta_2,\ldots\right] \tag{19}$$

where $\underset{\underset{\sim}{\approx}}{L}$ is a fourth-order distortion operator that possesses the same eigenprojectors as the elastic compliance, $\underset{\approx}{\alpha}$ is the backstress, η_i are internal state variables and may represent such things as porosity, and F is an isotropic function.

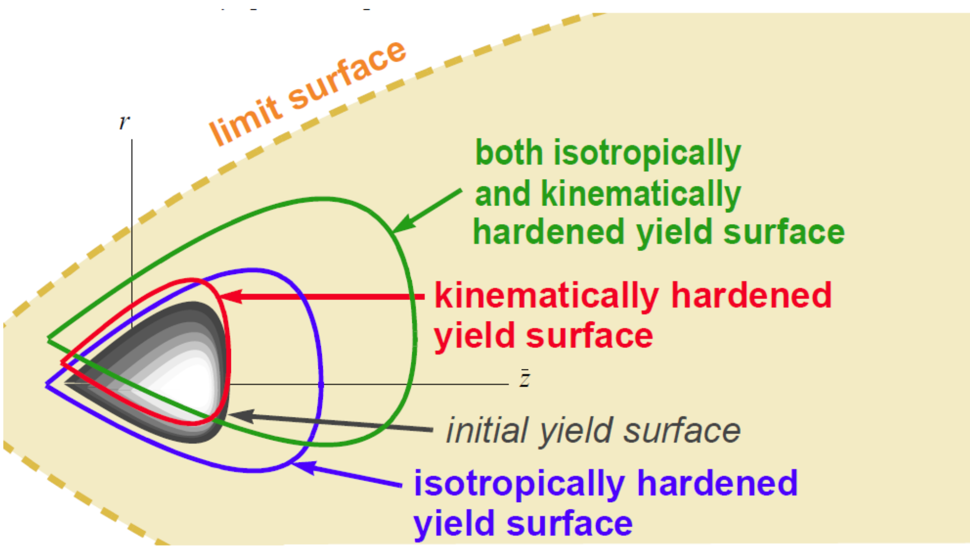

Figure 14. A meridional profile of an initial yield surface along with hardened yield surfaces.

For our approach, the $\underset{\underset{\sim}{\approx}}{L}$ tensor starts as the fourth-order identity in the initial state, but once deformed, $\underset{\underset{\sim}{\approx}}{L}$ evolves to an anisotropic tensor. An evolved stress term, $\underset{\approx}{\sigma}^*$, is defined where $\underset{\approx}{\sigma}^*=\underset{\underset{\sim}{\approx}}{L}:\left(\underset{\approx}{\sigma}-\underset{\approx}{\alpha}\right)$ (Note: $\underset{\approx}{\sigma}^*=\underset{\underset{\sim}{\approx}}{L}:\left(\underset{\approx}{\sigma}\right)$ if kinematic hardening is not present). A new anisotropic function, $f\left(\underset{\approx}{\sigma}\right)$, is introduced

$$f\left(\underset{\approx}{\sigma},\underset{\underset{\sim}{\approx}}{L},\underset{\approx}{\alpha}\right)=F\left(\underset{\approx}{\sigma}^*,\eta_1,\eta_2,\ldots\right) \tag{20}$$

where $\underset{\underset{\sim}{\approx}}{L}$ and $\underset{\approx}{\alpha}$ act as additional internal state variables. As written, the yield surface is evolved by changes in $\underset{\underset{\sim}{\approx}}{L}$ and $\underset{\approx}{\alpha}$ even if F does not change.

If an associative flow rule is assumed, the plastic part of the strain rate, $\dot{\underset{\approx}{\varepsilon}}^p$, can be expressed as

$$\dot{\underset{\approx}{\varepsilon}}^p = \dot{\lambda} \underset{\approx}{M}, \quad \text{where } \underset{\approx}{M} = \text{sgn}\left(\frac{\partial f\left(\underset{\approx}{\sigma}\right)}{\partial \underset{\approx}{\sigma}} \right)_{\underset{\approx}{\alpha},\eta} \tag{21}$$

Here, "sgn" is the signum operator, making $\underset{\approx}{M}$, therefore, a unit tensor in the direction of the yield surface gradient, $\frac{\partial f\left(\underset{\approx}{\sigma}\right)}{\partial \underset{\approx}{\sigma}}$. Accordingly, the scalar multiplier $\dot{\lambda}$ (called the consistency parameter) is the magnitude of the plastic strain rate. The direction cosines of the normal vector to the yield surface are proportional to components of the gradient $\frac{\partial f\left(\underset{\approx}{\sigma}\right)}{\partial \underset{\approx}{\sigma}}$. In our case, the gradient through the use of Equation (20) is

$$\frac{\partial f\left(\underset{\approx}{\sigma}\right)}{\partial \underset{\approx}{\sigma}} = \frac{\partial F\left(\underset{\approx}{\sigma}^*\right)}{\partial \underset{\approx}{\sigma}^*} : \frac{\partial \underset{\approx}{\sigma}^*}{\partial \underset{\approx}{\sigma}} = \frac{\partial F\left(\underset{\approx}{\sigma}^*\right)}{\partial \underset{\approx}{\sigma}^*} : \underset{\approx}{\underset{\approx}{L}} \tag{22}$$

where $\underset{\approx}{\underset{\approx}{L}} = \partial \underset{\approx}{\sigma}^* \big/ \partial \underset{\approx}{\sigma}$. The gradient $\partial f\left(\underset{\approx}{\sigma}\right) \big/ \partial \underset{\approx}{\sigma}$ has an isotropic part giving rise to dilatation even if $\partial \underset{\approx}{\sigma}^* \big/ \partial \underset{\approx}{\sigma}$ does not have an isotropic part.

The evolution equations for $\underset{\approx}{\underset{\approx}{L}}$ must allow for dilatation in triaxial compression without expanding the yield surface in the case of hydrostatic compression. If material failure is proposed to be governed by attainment of a critical strain, then (as derived in Appendix A) $\underset{\approx}{\underset{\approx}{L}}$ can be defined as

$$\underset{\approx}{\underset{\approx}{L}} = \underset{\approx}{\underset{\approx}{C}}_o : \underset{\approx}{\underset{\approx}{S}}$$

where $\underset{\approx}{\underset{\approx}{S}}$ is the generally anisotropic compliance tensor of the deformed material and $\underset{\approx}{\underset{\approx}{C}}_o$ is the isotropic elastic stiffness of the undeformed material. As demonstrated in upcoming sections, if a transversely isotropic expression for the compliance is used, dilatation can result. A shear stress component of large magnitude can open some microcracks and cause a reduction of stiffness in the lateral directions. For the case of hydrostatic loading, all of the cracks will close, resulting in no reduction in stiffness.

3.2 Stress Tensor in Terms of Lode Coordinates for TXC

Given that $\underset{\approx}{\sigma}$ and $\underset{\approx}{\varepsilon}$ are symmetric, the tensors can be interpreted as six-dimensional vectors (first order tensors), and since $\underset{\approx\approx}{C}$ is doubly symmetric, its component matrix may be written as a 6×6 Mandel matrix, which differs from more conventional Voigt representations by factors of $\sqrt{2}$ in the last three rows and columns. For the case of TXC, the state of stress can be decomposed into two components;

$$\underset{\approx}{\sigma} = \sigma_A \begin{bmatrix} 0 & 0 & 0 \\ 0 & 0 & 0 \\ 0 & 0 & 1 \end{bmatrix} + \sqrt{2}\sigma_L \frac{1}{\sqrt{2}} \begin{bmatrix} 1 & 0 & 0 \\ 0 & 1 & 0 \\ 0 & 0 & 0 \end{bmatrix} = \sigma_A \underset{\approx}{E}_A + \sqrt{2}\sigma_L \underset{\approx}{E}_L \tag{23}$$

the subscript A and L correspond to the axial and lateral directions, respectively, and the two $\underset{\approx}{E}$ tensors form an orthonormal basis for the set of all second-order tensors that are axisymmetric about the 3-direction. In other words, axisymmetric stress can be viewed in a two-dimensional subspace of six-dimensional tensor space.

The stress tensor can alternatively be written as a component in the direction of the hydrostat, z, and as a component perpendicular to the hydrostat, r, as

$$\underset{\approx}{\sigma} = \sigma_z \frac{1}{\sqrt{3}} \begin{bmatrix} 1 & 0 & 0 \\ 0 & 1 & 0 \\ 0 & 0 & 1 \end{bmatrix} + \sigma_r \frac{1}{\sqrt{6}} \begin{bmatrix} -1 & 0 & 0 \\ 0 & -1 & 0 \\ 0 & 0 & 2 \end{bmatrix} = \sigma_z \underset{\approx}{E}_z + \sigma_r \underset{\approx}{E}_r \tag{24}$$

The affine change in basis between the two coordinate systems shown by Equations (23) and (24) is given by

$$\begin{bmatrix} \underset{\approx}{E}_z \\ \underset{\approx}{E}_r \end{bmatrix} = \frac{1}{\sqrt{3}} \begin{bmatrix} 1 & \sqrt{2} \\ \sqrt{2} & -1 \end{bmatrix} \begin{bmatrix} \underset{\approx}{E}_A \\ \underset{\approx}{E}_L \end{bmatrix} \tag{25}$$

Conceptually, the change in basis is shown in **Figure 15**.

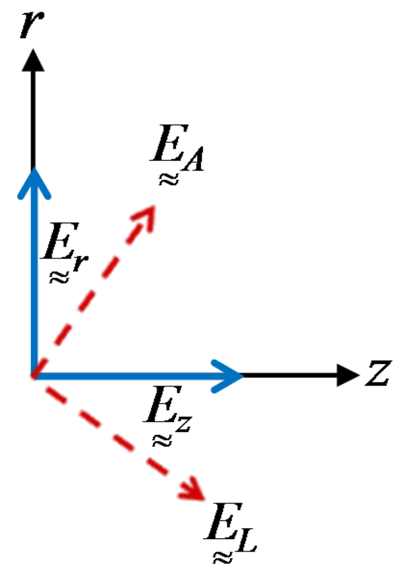

Figure 15. Change of basis from Lode to TXC coordinates.

3.3 Transverse Isotropic Compliance Matrix

The compliance matrix for a transversely isotropic material can be written as [80]

$$\begin{bmatrix} h_0 & h_2 & h_3 & 0 & 0 & 0 \\ h_2 & h_0 & h_3 & 0 & 0 & 0 \\ h_3 & h_3 & h_1 & 0 & 0 & 0 \\ 0 & 0 & 0 & h_5 & 0 & 0 \\ 0 & 0 & 0 & 0 & h_5 & 0 \\ 0 & 0 & 0 & 0 & 0 & h_4 \end{bmatrix} \tag{26}$$

where $h_0 = h_2 + h_4 = S_{1122} + 2S_{1212}$, $h_1 = S_{3333}$, $h_2 = S_{1122}$, $h_3 = S_{1133}$, $h_4 = 2S_{1212}$, and $h_5 = 2S_{3131}$.

For a material having axisymmetry about a given orientation, $\underset{\sim}{n}$ [81], the macroscopic material properties must be unchanged upon any rigid rotation

about $\underset{\sim}{n}$. The compliance of such a material is also transversely isotropic with respect to $\underset{\sim}{n}$, and is expressible as a linear combination of a natural basis, $\underset{\approx}{B}_i$ (where i ranges from

1 to 5)

$$\underset{\approx}{S} = h_1 \underset{\approx}{B}_1 + h_2 \underset{\approx}{B}_2 + h_3 \underset{\approx}{B}_3 + h_4 \underset{\approx}{B}_4 + h_5 \underset{\approx}{B}_5 \tag{27}$$

Here, the five parameters $\{h_1, ..., h_5\}$ quantify the anisotropic compliance, and (if desired) a scalar measure of anisotropy can be evaluated using formulas developed by Fuller and Brannon [82]. The quantities $\left\{\underset{\approx}{B}_1, ..., \underset{\approx}{B}_5\right\}$ are the five transversely-isotropic base tensors, which can be written out in full indicial notation as [80]

$$\left(\underset{\approx}{B}_1\right)_{ijkl} = n_i n_j n_k n_l \tag{28}$$

$$\left(\underset{\approx}{B}_2\right)_{ijkl} = \delta_{ij}\delta_{kl} - n_i n_j \delta_{kl} - \delta_{ij} n_k n_l + n_i n_j n_k n_l \tag{29}$$

$$\left(\underset{\approx}{B}_3\right)_{ijkl} = n_i n_j \delta_{kl} + \delta_{ij} n_k n_l - 2 n_i n_j n_k n_l \tag{30}$$

$$\left(\underset{\approx}{B}_4\right)_{ijkl} = \frac{1}{2}\left(\delta_{ik}\delta_{jl} + \delta_{il}\delta_{jk}\right) - \frac{1}{2}\left(\delta_{il} n_j n_k + n_i \delta_{jk} n_l + n_i \delta_{jl} n_k + \delta_{ik} n_j n_l\right) + n_i n_j n_k n_l \tag{31}$$

$$\left(\underset{\approx}{B}_5\right)_{ijkl} = \frac{1}{2}\left(\delta_{ik} n_j n_l + \delta_{il} n_j n_k + n_i \delta_{jl} n_k + n_i \delta_{jk} n_l\right) - 2 n_i n_j n_k n_l \tag{32}$$

Important insight is revealed by noting how each of the base tensors transform an arbitrary stress tensor, $\underset{\approx}{\sigma}$. If a physical basis is set up with $\underset{\sim}{n}$ aligned in the 3-direction, $\begin{Bmatrix} 0 \\ 0 \\ 1 \end{Bmatrix}$, (the tensors for $\underset{\approx}{B}_i$ for this case are shown in [80]) then

$$\left[\underset{\approx}{B}_1 : \underset{\approx}{\sigma}\right] = \begin{bmatrix} 0 & 0 & 0 \\ 0 & 0 & 0 \\ 0 & 0 & \sigma_{33} \end{bmatrix}$$

$$\left[\underset{\approx}{\underset{\approx}{B}}_2 : \underset{\approx}{\sigma}\right] = \begin{bmatrix} \sigma_{11}+\sigma_{22} & 0 & 0 \\ 0 & \sigma_{11}+\sigma_{22} & 0 \\ 0 & 0 & 0 \end{bmatrix}$$

$$\left[\underset{\approx}{\underset{\approx}{B}}_3 : \underset{\approx}{\sigma}\right] = \begin{bmatrix} \sigma_{33} & 0 & 0 \\ 0 & \sigma_{33} & 0 \\ 0 & 0 & \sigma_{11}+\sigma_{22} \end{bmatrix}$$

$$\left[\underset{\approx}{\underset{\approx}{B}}_4 : \underset{\approx}{\sigma}\right] = \begin{bmatrix} \sigma_{11} & \sigma_{12} & 0 \\ \sigma_{21} & \sigma_{22} & 0 \\ 0 & 0 & 0 \end{bmatrix}$$

$$\left[\underset{\approx}{\underset{\approx}{B}}_5 : \underset{\approx}{\sigma}\right] = \begin{bmatrix} 0 & 0 & \sigma_{13} \\ 0 & 0 & \sigma_{23} \\ \sigma_{31} & \sigma_{32} & 0 \end{bmatrix}$$

Inspection of the relations given above shows that $\underset{\approx}{\underset{\approx}{B}}_1$ extracts the part of $\underset{\approx}{\sigma}$ that acts in the direction of $\underset{\sim}{n}$, which makes that part of the compliance tensor account for axial strain response to axial stress. The tensor $\underset{\approx}{\underset{\approx}{B}}_2$ yields the transverse trace $\sigma_{11}+\sigma_{22}$ times the transverse identity, and this part of the compliance accounts for inplane isotropic strain response to an inplane isotropic stress stimulus. The base tensor $\underset{\approx}{\underset{\approx}{B}}_3$ maps the axial component σ_{33} to the transverse 11 and 22 positions, and in addition, also maps the transverse trace $\sigma_{11}+\sigma_{22}$ to the axial 33 position; thus, the $\underset{\approx}{\underset{\approx}{B}}_3$ contribution to the compliance accounts for axial strain caused by lateral stress or lateral strain caused by axial stress (i.e., it accommodates a Poisson's effect). The base tensor $\underset{\approx}{\underset{\approx}{B}}_4$ extracts the transverse part of $\underset{\approx}{\sigma}$. The tensor $\underset{\approx}{\underset{\approx}{B}}_5$ projects $\underset{\approx}{\sigma}$ to its part that tends to shear the axis of symmetry [83].

3.4 Dienes Relation for a Damaged Material

Dienes et al. [84], give an expression for the compliance change that results from an ensemble of microcracks of all sizes and orientations. Their expression for $\Delta \underset{\approx}{\underset{\approx}{S}}$, written only for open penny-shaped cracks, is

$$\Delta \underset{\approx}{S} = \gamma \sum A_1 \underset{\approx}{c}^o \tag{33}$$

Here, the summation ranges over each crack size and crack orientation. The terms are defined as follows:

- The term - $\gamma \sum A_1 \underset{\approx}{c}^o$ represents the contribution from the open cracks, with the individual terms defined as
  - $A_1 = H[\sigma_n] F_\rho(\underset{\sim}{n}, t) \Delta\Psi$.
  - $\gamma = 8(1-\nu_o)/3G_o(2-\nu_o)$ is an elastic constant that arises from analytical solutions for open penny-shaped cracks with G_o and ν_o being the shear modulus and Poisson's ratio of the underlying substrate material, respectively.
  - $H[\sigma_n] = 1$ for an open cracks, and $H[\sigma_n] = 0$ for a closed crack. H is the Heaviside function (equal to one for positive arguments and zero for negative arguments), $\sigma_n = \underset{\sim}{n} \cdot \underset{\approx}{\sigma} \cdot \underset{\sim}{n}$ and is the normal component of the remote (far-field) traction.
  - $F_\rho(\underset{\sim}{n}, t)$ is the third moment of the number density-distribution function, $n(a, \underset{\sim}{n}, t)$: $F_\rho(\underset{\sim}{n}, t) = \int_0^\infty n(a, \underset{\sim}{n}, t) a^3 da$, where a is the crack size, $\underset{\sim}{n}$ is the unit normal to the penny-shaped crack, and t is the time. The expression $n(a, \underset{\sim}{n}, t)$ is the number density defining the distribution of crack radii and orientations, which evolve with time, t. Specifically, if N_V is the number of cracks per unit volume and if $p(a, \underset{\sim}{n}, t)$ is the joint probability density for crack size a and crack orientation $\underset{\sim}{n}$, then $n(a, \underset{\sim}{n}, t) = N_V p(a, \underset{\sim}{n}, t)$.
  - The open fabric tensor is defined as

$$c_{ijkl}^o = \frac{1}{2}\left(n_i n_k \delta_{jl} + n_i n_l \delta_{jk} + n_j n_l \delta_{ik} + n_j n_k \delta_{il}\right) - \nu_o n_i n_j n_k n_l$$

  - $\Delta\Psi = \sin\varphi \Delta\theta \Delta\varphi$ is the solid angle on the unit sphere. The cracks have symmetry such that a reversal of 180° leaves them unchanged. Thus, half the unit sphere is sufficient to characterize crack orientation; consequently, the integration limits for orientation are $0 \le \theta \le 2\pi$ and $0 \le \varphi \le \pi/2$.

3.5 Kachanov Relation for a Damaged Material

Kachanov [85] describes the change in the tensor of elastic compliances due to the multiple circular cracks of arbitrary orientation distribution as

$$\Delta S_{ijkl} = \frac{32\left(1-\nu_o^2\right)}{3\left(2-\nu_o\right)E_o}\left[\frac{1}{4}\left(\alpha_{ik}^K\delta_{jl} + \alpha_{il}^K\delta_{jk} + \alpha_{jl}^K\delta_{ik} + \alpha_{jk}^K\delta_{il}\right) - \frac{\nu_o}{2}\beta_{ijkl}\right] \qquad (34)$$

where

- $\underset{\approx}{\alpha}^K = \frac{1}{V}\sum_i a_i^3 \underset{\sim}{n}_i \underset{\sim}{n}_i$ is a symmetric second-rank crack density tensor. The summation over *i* ranges over the cracks in the sample, where $\underset{\sim}{n}_i$ is the unit normal to the i-th crack, a_i is the radius of the i-th crack, and V is the representative volume. As discussed below, this tensor in Kachanov's theory would be equivalent to $\sum F_\rho\left(\underset{\sim}{n},t\right)\underset{\sim}{n}\underset{\sim}{n}\Delta\Psi$ in Dienes' theory.
- $\underset{\approxeq}{\beta} = \frac{1}{V}\sum_i a_i^3 \underset{\sim}{n}_i \underset{\sim}{n}_i \underset{\sim}{n}_i \underset{\sim}{n}_i$ is a fourth-rank tensor, equivalent to $\sum F_\rho\left(\underset{\sim}{n},t\right)\underset{\sim}{n}\underset{\sim}{n}\underset{\sim}{n}\underset{\sim}{n}\Delta\Psi$ in Dienes' notation.

In addition to the Equations (33) and (34), other authors have given expressions for the compliance that account for differently shaped cracks, traction forces, etc. [52, 74-77]

3.6 Comparison of Dienes and Kachanov Compliance Terms

Working with the first term of the Dienes expression in Equation (33) gives

$$\Delta S_{ijkl} = \frac{8\left(1-\nu_o\right)}{3G_o\left(2-\nu_o\right)}\left[\sum_\Psi H\left[\sigma_n\right]F_\rho\left(\underset{\sim}{n},t\right)\Delta\Psi\begin{pmatrix}\frac{1}{2}\left(n_i n_k\delta_{jl} + n_i n_l\delta_{jk} + n_j n_l\delta_{ik} + n_j n_k\delta_{il}\right)\\ -\nu_o n_i n_j n_k n_l\end{pmatrix}\right] \qquad (35)$$

The multiplicative factor in front of the summation may be written in terms of E_o using $\frac{1}{G_o} = \frac{2\left(1+\nu_o\right)}{E_o}$. The multiplicative factor becomes $\frac{8\left(1-\nu_o\right)}{3G_o\left(2-\nu_o\right)} = \frac{16\left(1-\nu_o^2\right)}{3E_o\left(2-\nu_o\right)}$.

In Equation (35), the expression, $H\left[\sigma_n\right]=1$ for an open crack and the compliance expression can be written as

$$\Delta S_{ijkl} = \frac{32\left(1-\nu_o^2\right)}{3E_o\left(2-\nu_o\right)}\left[\sum_\Psi F_\rho\left(\underset{\sim}{n},t\right)\Delta\Psi\left(\frac{1}{4}\begin{pmatrix}n_i n_k\delta_{jl} + n_i n_l\delta_{jk}\\ +n_j n_l\delta_{ik} + n_j n_k\delta_{il}\end{pmatrix} - \frac{1}{2}\nu_o n_i n_j n_k n_l\right)\right] \qquad (36)$$

Using $F_\rho\left(\underset{\sim}{n},t\right)=\int_0^\infty n\left(a,\underset{\sim}{n},t\right)a^3da$ to be consistent with Dienes' theory,

$$\Delta S_{ijkl}=\frac{32\left(1-\nu_o^2\right)}{3E_o\left(2-\nu_o\right)}\left[\sum_{\Psi}\int_0^\infty n\left(a,\underset{\sim}{n},t\right)a^3da\ \Delta\Psi\begin{pmatrix}\frac{1}{4}\begin{pmatrix}n_in_k\delta_{jl}+n_in_l\delta_{jk}\\+n_jn_l\delta_{ik}+n_jn_k\delta_{il}\end{pmatrix}\\-\frac{1}{2}\nu_on_in_jn_kn_l\end{pmatrix}\right] \tag{37}$$

The Kachanov expression, Equation (34), can be written as

$$\Delta S_{ijkl}=\frac{32\left(1-\nu_o^2\right)}{3E_o\left(2-\nu_o\right)}\left[\sum_a\frac{a^3}{V}\left(\frac{1}{4}\begin{pmatrix}n_in_k\delta_{jl}+n_in_l\delta_{jk}\\+n_jn_l\delta_{ik}+n_jn_k\delta_{il}\end{pmatrix}-\frac{1}{2}\nu_on_in_jn_kn_l\right)\right] \tag{38}$$

Equation (37) and Equation (38) are equivalent (assuming only open cracks) when

$$\sum_a\frac{a^3}{V}=\sum_\Psi\int_0^\infty n\left(a,\underset{\sim}{n},t\right)a^3da\ \Delta\Psi=\sum_\Psi\int_0^\infty N_V\,p\left(a,\underset{\sim}{n},t\right)a^3da\ \Delta\Psi$$

recalling that $n\left(a,\underset{\sim}{n},t\right)=N_V\,p\left(a,\underset{\sim}{n},t\right)$.

Dienes clearly defines a number of cracks per unit volume along with a continuous crack size distribution, $p\left(a,\underset{\sim}{n},t\right)$, whereas Kachanov implies an equivalent term resulting from the summation over discrete crack sizes and orientations. Thus, Kachanov's theory is a special case of Dienes' theory corresponding to the crack size distribution function being a sum of Dirac deltas

$$p\left(a,\underset{\sim}{n},t\right)=\sum_{i=1}^{N_VV}p_i(\underset{\sim}{n})\delta(a-a_i) \tag{39}$$

where N_VV is the total number of cracks in the representative volume element and $p_i(\underset{\sim}{n})$ is the fraction of the total number of cracks having size a_i. Substituting this discrete distribution into Dienes' expression gives

$$\sum_\Psi\sum_{i=1}^{N_VV}\int_0^\infty N_V\,p_i(\underset{\sim}{n})\delta(a-a_i)a^3da\ \Delta\Psi=\sum_\Psi\sum_{i=1}^{N_VV}\frac{N_i(\underset{\sim}{n})}{V}a_i^3\ \Delta\Psi=\sum_a\frac{a^3}{V} \tag{40}$$

where $N_i(\underset{\sim}{n})$ is the total number of cracks of size *"i"* and orientation $\underset{\sim}{n}$ in the volume. The equivalence with Kachanov's theory in the final step follows by noting that the summation over $\Delta\Psi$ accumulates contributions from all possible crack orientations.

3.7 Expected Form of the Transverse Isotropic Compliance Matrix

For a material having a spatially uniform array of axisymmetric cracks all of a given orientation, $\underset{\sim}{n}$, [83] the imposed geometric symmetry demands that the macroscopic material properties be unchanged upon any rigid rotation about $\underset{\sim}{n}$. The change in compliance of such a material is also transversely isotropic with respect to $\underset{\sim}{n}$, and therefore expressible as a linear combination of a natural basis, $\underset{\approx}{B_i}$ (where i ranges from 1 to 5) as

$$\Delta \underset{\approx}{S}\left(a,\mu^o,\rho,\underset{\sim}{n},\right)=\underset{\approx}{S}\left(a,\mu^o,\rho,\underset{\sim}{n}\right)-\underset{\approx}{S_o}\left(\mu^o\right)=\sum_{i=1}^{5}h_i\left(a,\mu^o,\rho\right)\underset{\approx}{B_i}\left(\underset{\sim}{n}\right) \qquad (41)$$

where a is the radius of the crack, ρ is the number of cracks per unit mass, $\underset{\approx}{S_o}$ is the isotropic compliance of the underlying substrate matrix material, μ^o collectively stands for the elastic properties of the substrate material, the five parameters $\{h_1,...,h_5\}$ quantify the anisotropy, and the five transverse tensors { $\underset{\approx}{B_1}$, ..., $\underset{\approx}{B_5}$ } form a basis for the set of all major- and minor-symmetric transversely isotropic fourth-order tensors.

Certain terms in the expansion series from Equation (41) can be eliminated based on comparisons against compliance expressions from Dienes et al. [84] and Kachanov [85]. In their expressions, Dienes and Kachanov set all values of $h_i\left(a,\mu^o,\rho\right)$ equal to zero, except for $i=1$ and $i=5$.

3.8 Compliance Descriptions for a Damaged Material

During triaxial loading, flaws may nucleate, or if flaws are present in an undeformed state, the shape and orientation of the flaws may change during deformation. These flaws can appear as a number of different shapes, ranging from cracks to pores or even as irregular shapes as “potato chip” shaped flaws [86]. From a phenomenological perspective, cracks, pores, etc. can represent the same thing in the sense that they all can reduce the stiffness of a material.

As shown in **Figure 16**, the cracks are randomly oriented prior to deformation. As compression occurs, sliding of the crack faces will initiate at approximately 45° to the principal compression direction, along the plane of maximum shear stress. With additional loading, the cracks develop into wing cracks in the direction of axial loading [87, 88]. Assuming that newly formed crack surfaces, appearing after the kinking process begins, are large in comparison to the initial crack surface area, a single unit normal to the crack (perpendicular to the principal loading direction) approximates the particular crack orientation.

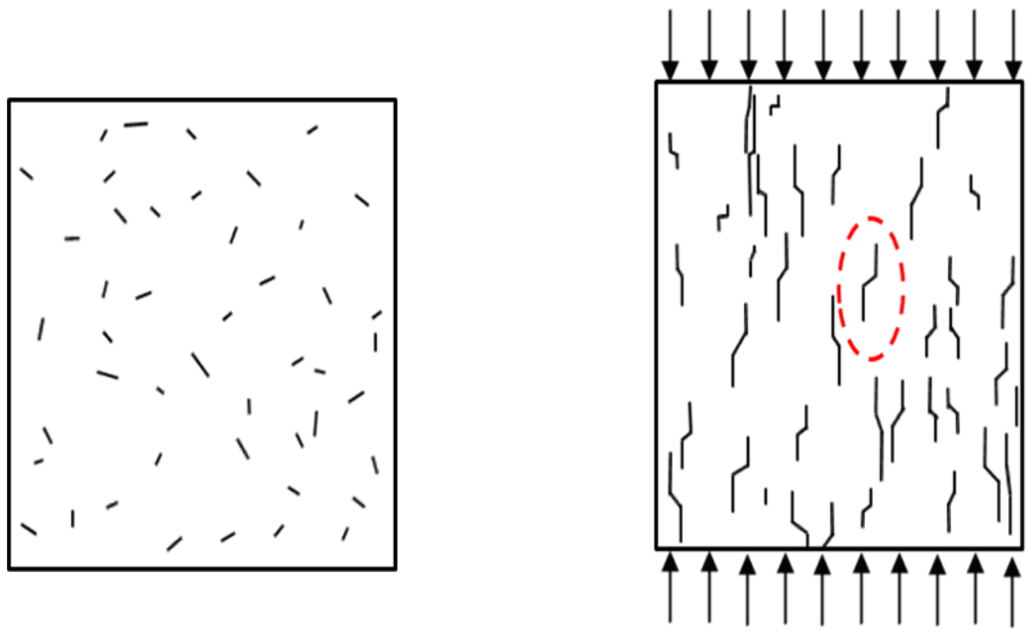

(a) (b)

Figure 16. Evolution of crack flaws: (a) undamaged material consisting of circular cracks, (b) as triaxial compression is applied to the material; cracks grow in the principal loading direction (Graham-Brady [86]).

A unit normal may be regarded as a vector extending from the origin to a point on the unit sphere. In the undeformed state, a uniformly random distribution of crack normals corresponds to a uniformly random distribution of points on the unit sphere. Depending on the extent of deformation, the cracks will reorient; possibly starting at a 45° angle to the principal loading direction and then kinking to a 90° angle [87] to reorient the leading edge of the growing crack face to be perpendicular to the direction of the largest principal stress.

When the cracks are more fully developed, the unit normals will evolve to be nearly perpendicular to the principal loading direction, thereby producing a clustering of points on the unit sphere in the vicinity of the equator. An example of this is shown in **Figure 17**, which depicts random distributions of points on a unit sphere for **Figure 17**(a). Then as the cracks evolve, the point distribution becomes concentrated, perpendicular to the loading direction (see **Figure 17**(b)).

3.9 Transverse Isotropy Over an Axisymmetric Probabilistic Distribution

In a body with many small circular cracks, each particular crack can be described with a radius of a, and a unit normal, $\underset{\sim}{n}$, to denote the crack's orientation. As illustrated in Figure 18, $\underset{\sim}{n}$ is the position vector on the unit sphere. Written in terms of the base vectors, $\underset{\sim}{e}_i$, the orientation vector can be written as $\underset{\sim}{n} = x_1\underset{\sim}{e}_1 + x_2\underset{\sim}{e}_2 + x_3\underset{\sim}{e}_3$ where $x_1^2 + x_2^2 + x_3^2 = 1$.

In Figure 18, the vector $\underset{\sim}{m}$ is taken as the principal loading direction. As described previously, the overall compliance of the material depends on the

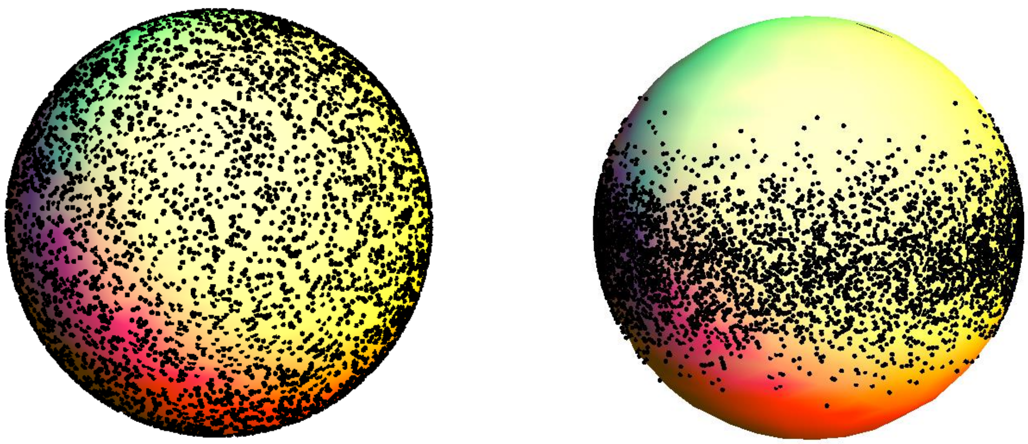

(a) (b)

Figure 17. Distribution of points on a unit sphere: (a) a uniformly random distribution of points; (b) a conceptual concentration of points caused by alignment of the unit normals in a direction perpendicular to the loading direction.

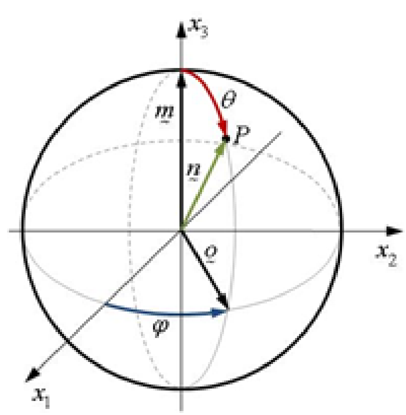

Figure 18. Spherical coordinates.

orientation and size of the materials heterogeneities.

The distribution of cracks in the material can be described by a probability distribution function that depends on both a and $\underset{\sim}{n}(\theta,\varphi)$ (θ and φ are the spherical coordinates depicted in Figure 18).

The probability function will be written as $p\left(a,\underset{\sim}{n}(\theta,\varphi)\right)$, and is defined such that the probability of a randomly selected crack has the size and orientation parameters falling in ranges $a_1 < a < a_2$, $\theta_1 < \theta < \theta_2$, and $\phi_1 < \phi < \phi_2$ is

$$\int_{a_1}^{a_2}\int_{\theta_1}^{\theta_2}\int_{\phi_1}^{\phi_2} p\left(a,\underset{\sim}{n}(\theta,\varphi)\right)\sin\theta\, d\varphi\, d\theta\, da$$

The function $\underset{\sim}{n}(\theta,\varphi)$ is referenced to the axis of symmetry, $\underset{\sim}{m}$, through the spherical coordinates θ and φ.

Cracks are "neutrally oriented" in the sense that a crack with orientation $-\underset{\sim}{n}$ is equivalent to a crack with orientation $\underset{\sim}{n}$. On this basis, the distribution function is defined such that $p\left(a,\underset{\sim}{n}(\theta,\varphi)\right) = p\left(a,-\underset{\sim}{n}(\theta,\varphi)\right)$.

In the virgin state, where the flaw orientations are presumed to be uniformly random in orientation, the initial density function is independent of crack orientation. As an axial load is applied along the vector $\underset{\sim}{m}$, the flaws will kink to a new equivalent orientation in response to the load, thereby producing a new dependence of the distribution function on the crack orientation. In particular, while any crack orientation is equally likely in the virgin state, additional crack growth beyond an approximate 45° angle makes vertical cracks increasingly likely. The new distribution of cracks will have a bias towards vertical cracks.

However, because of the symmetry of loading, no bias is introduced in the dependence of the distribution on the angle φ. As illustrated in **Figure 19**, given that a randomly selected crack has orientation angle θ, a uniform probability for ϕ is present. In **Figure 19**, the red funnel shows the full circumferential sweep for a unit normal with $\theta = constant,\ \varphi = 0$ to 2π.

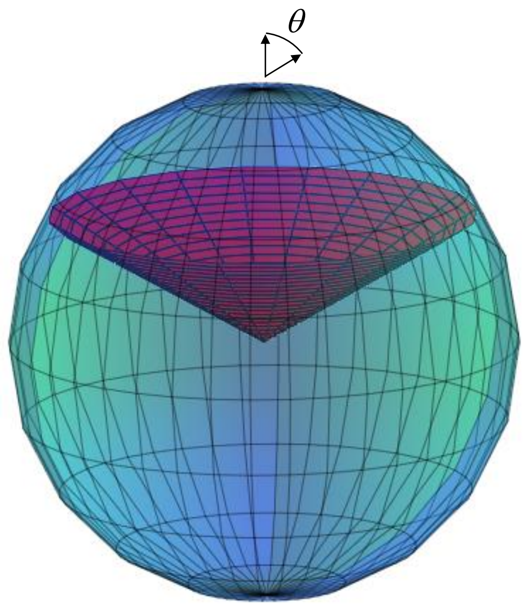

Figure 19. Illustration of uniform distribution of unit normals for a fixed azimuthal angle θ.

The distribution function made by these reoriented flaws will be denoted as $q(a,\theta)$ and is restricted for cracks that have a size between a_1 and a_2, and having an orientation vector forming an angle θ between θ_1 and θ_2 measured from the symmetry axis $\underset{\sim}{m}$. The fraction of inclusions that fall within these limits is defined by $\int_{a_1}^{a_2}\int_{\theta_1}^{\theta_2} q(a,\theta)\,d\theta da$. The function $q(a,\theta)$ is related to $p\left(a,\underset{\sim}{n}(\theta,\varphi)\right)$ through the integrand (assuming that the integrand holds for all integration limits) as

$$\int_{a_1}^{a_2}\int_{\theta_1}^{\theta_2} q(a,\theta)\,d\theta da = \int_{a_1}^{a_2}\int_{\theta_1}^{\theta_2}\int_0^{2\pi} p\left(a,\underset{\sim}{n}(\theta,\phi)\right)\sin\theta\, d\phi d\theta\, da \tag{42}$$

where, $\underset{\sim}{n}(\theta)$ for axisymmetric distributions is a function of θ.

Simplification of Equation (42), taking the value of $p\left(a,\underset{\sim}{n}(\theta,\phi)\right)$ to be independent of ϕ for an axisymmetric distribution, results in

$$q(a,\theta) = 2\pi\sin\theta\, p\left(a,\underset{\sim}{n}(\theta,\phi)\right) \tag{43}$$

3.9.1 Compliance Expression Including Flaws

For a body containing flaws with a random distribution of sizes and orientation, the increase in compliance is taken to be the sum of the increases for each possible crack size and orientation times the fraction of cracks of that specified size and orientation [83].

The size and orientation distribution function, $p\left(a, \underset{\sim}{n}(\theta,\varphi)\right)$, can be combined with the aligned compliance given by $p\left(a, \underset{\sim}{n}(\theta,\varphi)\right) = \Pi(a)/4\pi$

$$\underset{\approx}{\Delta S}\left(a, \mu^o, \rho, \underset{\sim}{n}(\theta,\varphi),\right) = \sum_{i=1}^{5} \int_{\Omega}\int_{0}^{\infty} h_i\left(a, \mu^o, \rho\right) \underset{\approx}{B}_i\left(\underset{\sim}{n}\right) p\left(a, \underset{\sim}{n}(\theta,\varphi)\right) da d\Omega \qquad (44)$$

where Ω is the solid angled defined to be a contiguous patch of area on the unit sphere, which includes the diametrically opposite area for neutrally-oriented inhomogeneities. Integrating Equation (44) over the unit sphere for all possible orientations of $\underset{\sim}{n}(\theta,\varphi)$, may give a result that is anisotropic, depending on the distribution of $p\left(a, \underset{\sim}{n}(\theta,\varphi)\right)$. If the distribution function, $p\left(a, \underset{\sim}{n}(\theta,\varphi)\right)$ is axisymmetric about some fixed direction $\underset{\sim}{m}$, then symmetry demands that the net result for the integrant in Equation (44) will be transversely isotropic about the direction, $\underset{\sim}{m}$ [81].

3.9.2 Compliance Expression for an Axisymmetric Distribution

The compliance expression given by Equation (44) can be written for axisymmetric distributions as a combination of $q(a,\theta)$, where Equation (43) is defined by combining the size and orientation function into an axisymmetric distribution about $\underset{\sim}{m}$, and the transversely isotropic tensors, $\underset{\approx}{B}_i$, which are transversely isotropic about $\underset{\sim}{n}$. In the case that the distribution is axisymmetric about, $\underset{\sim}{m}$, Equation (44) simplifies to

$$\underset{\approx}{\Delta S}\left(a, \mu^o, \rho, \theta\right) = \sum_{i=1}^{5} \int_{0}^{\pi}\int_{0}^{\infty} h_i\left(a, \mu^o, \rho\right) q(a,\theta) da\, \underset{\approx}{\tilde{B}}_i(\theta)\, d\theta \qquad (45)$$

where

$$\underset{\approx}{\tilde{B}}_i(\theta) = \frac{1}{2\pi}\int_{0}^{2\pi} \underset{\approx}{B}_i\left(\underset{\sim}{n}(\varphi,\theta)\right) d\varphi \qquad (46)$$

The five integrals given of Equation (46) can be calculated in closed form as [81]

$$\underset{\approx}{\tilde{B}}_i(\theta) = \frac{1}{2\pi}\int_{0}^{2\pi} \underset{\approx}{B}_i\left(\underset{\sim}{n}(\varphi,\theta)\right) d\varphi = \sum_{j=1}^{5} \beta_{ji}(\theta) \underset{\approx}{b}_j \qquad (47)$$

where the coefficient functions, $\beta_{ji}(\theta)$ are given in **Table 3**, and the $\underset{\approx}{b}_j$ tensors are the transverse basis about $\underset{\sim}{m}$. Specifically,

Table 3: The coefficient function, $\beta_{ji}(\theta)$ (Note that $s = \sin\theta$ and $c = \cos\theta$)

	$\underset{\approx}{b}_1$	$\underset{\approx}{b}_2$	$\underset{\approx}{b}_3$	$\underset{\approx}{b}_4$	$\underset{\approx}{b}_5$
$\underset{\approx}{\tilde{B}}_1$	c^4	$\frac{s^4}{8}$	$\frac{c^2s^2}{2}$	c^2s^2	$\frac{s^4}{4}$
$\underset{\approx}{\tilde{B}}_2$	s^4	$\frac{s^4-8s^2+8}{8}$	$\frac{s^2}{2}\left(2-s^2\right)$	c^2s^2	$\frac{s^4}{4}$
$\underset{\approx}{\tilde{B}}_3$	$2c^2s^2$	$\frac{s^2}{4}\left(4-s^2\right)$	$\frac{2s^4-3s^2+2}{2}$	$-2c^2s^2$	$-\frac{s^4}{2}$
$\underset{\approx}{\tilde{B}}_4$	s^4	$\frac{s^4}{8}$	$\frac{c^2s^2}{2}$	$\frac{s^2}{2}\left(3-2s^2\right)$	$\frac{s^4-4s^2+4}{4}$
$\underset{\approx}{\tilde{B}}_5$	$2c^2s^2$	$-\frac{s^4}{4}$	$-c^2s^2$	$\frac{4s^4-5s^2+2}{2}$	$\frac{s^2}{2}\left(2-s^2\right)$

$$\left(\underset{\approx}{b}_1\right)_{ijkl} = m_i m_j m_k m_l \tag{48}$$

$$\left(\underset{\approx}{b}_2\right)_{ijkl} = \delta_{ij}\delta_{kl} - m_i m_j \delta_{kl} - \delta_{ij} m_k m_l + m_i m_j m_k m_l \tag{49}$$

$$\left(\underset{\approx}{b}_3\right)_{ijkl} = m_i m_j \delta_{kl} + \delta_{ij} m_k m_l - 2 m_i m_j m_k m_l \tag{50}$$

$$\begin{aligned}\left(\underset{\approx}{b}_4\right)_{ijkl} &= \frac{1}{2}\left(\delta_{ik}\delta_{jl} + \delta_{il}\delta_{jk}\right) - \frac{1}{2}\begin{pmatrix}\delta_{il} m_j m_k + m_i \delta_{jk} m_l \\ + m_i \delta_{jl} m_k + \delta_{ik} m_j m_l\end{pmatrix} \\ &\quad + m_i m_j m_k m_l\end{aligned} \tag{51}$$

$$\left(\underset{\approx}{b}_5\right)_{ijkl} = \frac{1}{2}\begin{pmatrix}\delta_{ik} m_j m_l + \delta_{il} m_j m_k \\ + m_i \delta_{jl} m_k + m_i \delta_{jk} m_l\end{pmatrix} - 2 m_i m_j m_k m_l \tag{52}$$

Substitution of Equation (47) into Equation (45) results in

$$\underset{\approx}{\Delta S}\left(a,\mu^{o},\rho,\theta\right)=\sum_{i=1}^{5}\left[\underbrace{\sum_{j=1}^{5}\int_{0}^{\pi}\underbrace{\left(\int_{0}^{\infty}h_{j}\left(a,\mu^{o},\rho\right)q\left(a,\theta\right)da\right)}_{\tilde{\alpha}_{j}}\beta_{ji}\left(\theta\right)d\theta}_{h_{i}^{c}}\right]\underset{\approx}{b_{i}}=\sum_{i=1}^{5}h_{i}^{c}\underset{\approx}{b_{i}} \tag{53}$$

where $h_i^c=\sum_{j=1}^{5}\int_0^{\pi}\tilde{\alpha}_j\left(\theta\right)\beta_{ji}\left(\theta\right)d\theta$, $\tilde{\alpha}_j\left(\theta\right)=\int_0^{\infty}h_j\left(a,\mu^o,\rho\right)q\left(a,\theta\right)da$, and $q\left(a,\theta\right)=2\pi\sin\theta\, p\left(a,\underset{\sim}{n}\left(\theta\right)\right)$.

3.10 Reduced Compliance for a Transversely Isotropic Material

Preexisting flaws can stably propagate via wing cracks towards the direction of maximum compressive stress [89]. When lateral compression is also present, the crack growth is usually stable and stops at some fixed length. Secondary cracks can also appear and can significantly contribute to crack coalescence [90].

In a typical triaxial compression test, the material is initially hydrostatically compressed, then the lateral stress is held constant, and the axial stress is varied. Loading continues until the material catastrophically fails or the test is terminated for other reasons (e.g., microstructural examination of the material). Unless additional information is available, the loading trace indicates very little about the nature of crack growth from the initial flaw up to the point of failure. For this discussion, it will be assumed that the primary contributor to crack propagation is the advancement of wing cracks parallel to the direction of maximum compressive stress (not an unreasonable assumption). In this case, the compliance will be most greatly increased in directions perpendicular to the wing cracks (i.e., lateral directions). If it is assumed that the only cracks of interest to the problem run parallel to the axis of symmetry, $\underset{\sim}{m}$, the unit normal for the vast majority of cracks has $\theta\approx 90°$. In this case, **Table 3** specializes to the result shown in **Table 4**.

Table

3.10.1 Reduced Compliance: Dienes and Kachanov Relations

As discussed previously, Dienes and Kachanov wrote the change in compliance as a combination of $\underset{\approx}{\tilde{B}_1}$ and $\underset{\approx}{\tilde{B}_5}$. In terms of these terms, Equation (45) then becomes

Table 4: The coefficient function, $\beta_{ji}(\theta)$ (from Table for $s=1$ and $c=1$)

	$\underset{\approx}{b}_1$	$\underset{\approx}{b}_2$	$\underset{\approx}{b}_3$	$\underset{\approx}{b}_4$	$\underset{\approx}{b}_5$
$\underset{\approx}{\tilde{B}}_1$	0	$\frac{1}{8}$	0	0	$\frac{1}{4}$
$\underset{\approx}{\tilde{B}}_2$	1	$\frac{1}{8}$	$\frac{1}{2}$	0	$\frac{1}{4}$
$\underset{\approx}{\tilde{B}}_3$	0	$\frac{3}{4}$	$\frac{1}{2}$	0	$-\frac{1}{2}$
$\underset{\approx}{\tilde{B}}_4$	1	$\frac{1}{8}$	0	$\frac{1}{2}$	$\frac{1}{4}$
$\underset{\approx}{\tilde{B}}_5$	0	$-\frac{1}{4}$	0	$\frac{1}{2}$	$\frac{1}{2}$

$$\Delta \underset{\approx}{S}\left(a,\mu^o,\rho,\theta\right)=\int_0^\pi\int_0^\infty h_1\left(a,\mu^o,\rho\right)q\left(a,\theta\right)da\,\underset{\approx}{\tilde{B}}_1\,d\theta + \int_0^\pi\int_0^\infty h_5\left(a,\mu^o,\rho\right)q\left(a,\theta\right)da\,\underset{\approx}{\tilde{B}}_5\,d\theta \tag{54}$$

Equation (54) can be written through the use of Equation (53) as

$$\Delta \underset{\approx}{S}\left(a,\mu^o,\rho,\theta\right)=\tilde{\alpha}_1\left[\beta_{11}(\theta)\underset{\approx}{b}_1+\beta_{12}(\theta)\underset{\approx}{b}_2+\beta_{13}(\theta)\underset{\approx}{b}_3+\beta_{14}(\theta)\underset{\approx}{b}_4+\beta_{15}(\theta)\underset{\approx}{b}_5\right] + \tilde{\alpha}_5\left[\beta_{51}(\theta)\underset{\approx}{b}_1+\beta_{52}(\theta)\underset{\approx}{b}_2+\beta_{53}(\theta)\underset{\approx}{b}_3+\beta_{54}(\theta)\underset{\approx}{b}_4+\beta_{55}(\theta)\underset{\approx}{b}_5\right] \tag{55}$$

where the $\beta_{ji}(\theta)$ terms are defined in **Table 3**.

Recalling that the current focus is on vertical cracks, using $\theta=90°$ reduces Equation (55) to

$$\Delta \underset{\approx}{S}\left(a,\mu^o,\rho\right)=\left(\frac{\tilde{\alpha}_1}{8}-\frac{\tilde{\alpha}_5}{4}\right)\underset{\approx}{b}_2+\frac{\tilde{\alpha}_5}{2}\underset{\approx}{b}_4+\left(\frac{\tilde{\alpha}_1}{4}+\frac{\tilde{\alpha}_5}{2}\right)\underset{\approx}{b}_5 \tag{56}$$

For the case of triaxial loading, the axial direction is aligned along the axis of symmetry and can be set parallel to the x_3 axis (i.e., $m_3 = \begin{pmatrix} 0 & 0 & 1 \end{pmatrix}^T$). If the resulting change in compliance (Mandel basis) acts on a stress tensor of the form $\underset{\approx}{\sigma} = \begin{pmatrix} \sigma_L & \sigma_L & \sigma_A & 0 & 0 & 0 \end{pmatrix}^T$, the result is

$$\frac{1}{8}\begin{bmatrix} \tilde{\alpha}_1 + 2\tilde{\alpha}_5 & \tilde{\alpha}_1 - 2\tilde{\alpha}_5 & 0 & 0 & 0 & 0 \\ \tilde{\alpha}_1 - 2\tilde{\alpha}_5 & \tilde{\alpha}_1 + 2\tilde{\alpha}_5 & 0 & 0 & 0 & 0 \\ 0 & 0 & 0 & 0 & 0 & 0 \\ 0 & 0 & 0 & 2\tilde{\alpha}_1 + 4\tilde{\alpha}_5 & 0 & 0 \\ 0 & 0 & 0 & 0 & 2\tilde{\alpha}_1 + 4\tilde{\alpha}_5 & 0 \\ 0 & 0 & 0 & 0 & 0 & 4\tilde{\alpha}_5 \end{bmatrix} \begin{bmatrix} \sigma_L \\ \sigma_L \\ \sigma_A \\ 0 \\ 0 \\ 0 \end{bmatrix} = \frac{1}{4}\begin{bmatrix} \tilde{\alpha}_1\sigma_L \\ \tilde{\alpha}_1\sigma_L \\ 0 \\ 0 \\ 0 \\ 0 \end{bmatrix} \tag{57}$$

Equation (57) indicates that the strain resulting from the change in compliance is applied in the transverse directions (i.e., parallel to the axis of symmetry). This is a desirable trend for our work in that we want the intensifier $\underset{\approxeq}{L}$ to increase in magnitude in the lateral directions for the case of triaxial loading. However, the resulting lateral strains shown in Equation (57) only return a contribution from the lateral stresses. In the case of axial loading along the $\underset{\sim}{m}$-axis, no stiffening results in the lateral directions. To fit our needs, other combinations of $\underset{\approxeq}{b}_i$ will be explored.

3.10.2 Selection of Terms Based on Poisson's Effects

For the conditions that $\theta \approx 90°$, $\underset{\sim}{m} = \begin{pmatrix} 0 & 0 & 1 \end{pmatrix}^T$, and $\underset{\approx}{\sigma} = \begin{pmatrix} 0 & 0 & \sigma_A & 0 & 0 & 0 \end{pmatrix}^T$, only $\underset{\approxeq}{\tilde{B}}_i$ terms that involve $\underset{\approxeq}{b}_3$ contribute to lateral increases in strain. Inspection of

Table 4 shows that only $\underset{\approxeq}{\tilde{B}}_2$ and $\underset{\approxeq}{\tilde{B}}_3$ have expansion terms involving $\underset{\approxeq}{b}_3$. Using Equation (54), $\beta_{ji}\left(\theta = 90°\right)$ as defined in

Table , and $\underset{\approx}{\sigma} = \begin{pmatrix} \sigma_L & \sigma_L & \sigma_A & 0 & 0 & 0 \end{pmatrix}^T$, the resulting strains (written in terms of a Mandel Basis) involving the $\underset{\approxeq}{\tilde{B}}_2$ and $\underset{\approxeq}{\tilde{B}}_3$ terms are

$$\underset{\approx}{\underset{\approx}{\Delta S}}_2\left(a,\mu^o,\rho\right):\underset{\approx}{\sigma}\Rightarrow\left[\frac{\tilde{\alpha}_2\sigma_A}{2}+\frac{\tilde{\alpha}_2\sigma_L}{4}\quad\frac{\tilde{\alpha}_2\sigma_A}{2}+\frac{\tilde{\alpha}_2\sigma_L}{4}\quad\tilde{\alpha}_2\sigma_A+\tilde{\alpha}_2\sigma_L\quad 0\quad 0\quad 0\right]^T \tag{58}$$

$$\underset{\approx}{\underset{\approx}{\Delta S}}_3\left(a,\mu^o,\rho\right):\underset{\approx}{\sigma}\Rightarrow\left[\frac{\tilde{\alpha}_3\sigma_A}{2}+\frac{3\tilde{\alpha}_3\sigma_L}{2}\quad\frac{\tilde{\alpha}_3\sigma_A}{2}+\frac{3\tilde{\alpha}_3\sigma_L}{2}\quad\tilde{\alpha}_3\sigma_L\quad 0\quad 0\quad 0\right]^T \tag{59}$$

where the subscript on $\underset{\approx}{\underset{\approx}{\Delta S}}$ denotes the corresponding value of $\underset{\approx}{\underset{\approx}{\tilde{B}}}$.

Comparing the strains, given by Equations (58) and (59), shows an enhancement in the lateral directions. However, the strains associated with $\underset{\approx}{\underset{\approx}{\Delta S}}_2$ (Equation (58)) have an enhancement in the axial direction that would not be expected. Conceptually, we are describing a continuum with penny-shaped cracks whose normals are circumferentially distributed parallel to the axis of symmetry. The presence of these cracks softens the material response parallel to the axis of symmetry (i.e., increases the lateral strain in response to an axial stress), but the axial response is expected to be unchanged. This precludes the use of $\underset{\approx}{\underset{\approx}{\tilde{B}}}_2$ as the axial strain is increased by $\alpha_2\sigma_A$ as shown in Equation (58). This makes $\underset{\approx}{\underset{\approx}{\tilde{B}}}_3$ the most likely test candidate as the lateral response is enhanced, but the axial response is unchanged as shown in Equation (59). It is realized that a more realistic model suitable for general loading would require terms such as $\underset{\approx}{\underset{\approx}{\tilde{B}}}_1$ and/or $\underset{\approx}{\underset{\approx}{\tilde{B}}}_5$ to account for compliance changes considered by Dienes and Kachanov. Omitting these terms is justified. The coefficient of $\underset{\approx}{\underset{\approx}{\tilde{B}}}_1$ is zero in this context because the cracks are all in compression. The action of $\underset{\approx}{\underset{\approx}{\tilde{B}}}_5$ on the stress is zero because the axisymmetric stress state has no shear component in the plane of the cracks.

3.11 Strain Based Failure Criterion for Transverse Isotropy

A strain based failure function, $g\left(\underset{\approx}{\varepsilon}\right)$, is defined such that failure occurs at a critical strain and is not dependent on crack sizes or orientations (i.e., $g\left(\underset{\approx}{\varepsilon}\right)=0$). The strain based failure function can be converted to a stress-based function $f\left(\underset{\approx}{\sigma}\right)$ using $\underset{\approx}{\varepsilon}=\underset{\approx}{\underset{\approx}{C}}:\underset{\approx}{\sigma}$ with the result of

$$f\left(\underset{\approx}{\sigma}\right) = g\left(\underset{\approx}{\underset{\approx}{C}}^{-1} : \underset{\approx}{\sigma}\right) \tag{60}$$

A stress-based function for the initial (possibly undeformed) state $F\left(\underset{\approx}{\sigma}\right)$ can be written as

$$F\left(\underset{\approx}{\sigma}\right) = g\left(\underset{\approx}{\underset{\approx}{C}}_o^{-1} : \underset{\approx}{\sigma}\right) \tag{61}$$

Defining $\underset{\approx}{\underset{\approx}{L}} = \underset{\approx}{\underset{\approx}{C}}_o : \underset{\approx}{\underset{\approx}{C}}^{-1} = \underset{\approx}{\underset{\approx}{C}}_o : \underset{\approx}{\underset{\approx}{S}}$ and following the approach used in Appendix A, Equations (60) and (61) can be equated as

$$f\left(\underset{\approx}{\sigma}\right) = F\left(\underset{\approx}{\underset{\approx}{L}} : \underset{\approx}{\sigma}\right) = F\left(\underset{\approx}{\underset{\approx}{C}}_o : \underset{\approx}{\underset{\approx}{C}}^{-1} : \underset{\approx}{\sigma}\right) \tag{62}$$

In Section 3.10.2, the chosen expression for the compliance is

$$\Delta S_3 = \tilde{\alpha}_3 \underset{\approx}{\underset{\approx}{\tilde{B}}}_3 \Rightarrow \underset{\approx}{\underset{\approx}{C}}^{-1} = \underset{\approx}{\underset{\approx}{C}}_m^{-1} + \tilde{\alpha}_3 \underset{\approx}{\underset{\approx}{\tilde{B}}}_3 \tag{63}$$

where $\underset{\approx}{\underset{\approx}{\tilde{B}}}_3 = \frac{3}{4}\underset{\approx}{\underset{\approx}{b}}_2 + \frac{1}{2}\underset{\approx}{\underset{\approx}{b}}_3 - \frac{1}{2}\underset{\approx}{\underset{\approx}{b}}_5$.

Also,

$$\underset{\approx}{\underset{\approx}{C}}_o^{-1} = \underset{\approx}{\underset{\approx}{C}}_m^{-1} + \tilde{\alpha}_{3o} \underset{\approx}{\underset{\approx}{\tilde{B}}}_3 \tag{64}$$

Solving Equation (64) for $\underset{\approx}{\underset{\approx}{C}}_m^{-1}$ and substituting into Equation (63) yields

$$\underset{\approx}{\underset{\approx}{C}}^{-1} = \underset{\approx}{\underset{\approx}{C}}_o^{-1} + \Delta\tilde{\alpha}_3 \underset{\approx}{\underset{\approx}{\tilde{B}}}_3 \tag{65}$$

where $\Delta\tilde{\alpha}_3$ is the compliance enhancement factor (CEF) defined as $\Delta\tilde{\alpha}_3 = \tilde{\alpha}_3 - \tilde{\alpha}_{3o}$.

Substituting Equation (65) into Equation (62) gives

$$f\left(\underset{\approx}{\sigma}, \Delta\tilde{\alpha}_3\right) = F\left(\underset{\approx}{C}_o : \left(\underset{\approx}{C}_o^{-1} + \Delta\tilde{\alpha}_3 \underset{\approx}{\tilde{B}}_3\right) : \underset{\approx}{\sigma}\right) = F\left(\underset{\approx}{\sigma} + \Delta\tilde{\alpha}_3 \underset{\approx}{C}_o : \underset{\approx}{\tilde{B}}_3 : \underset{\approx}{\sigma}\right) \qquad (66)$$

As written in Equation (66), $f(\ )$ is a function of $\underset{\approx}{\sigma}$ and $\Delta\tilde{\alpha}_3$ since only $\underset{\approx}{\sigma}$ and $\Delta\tilde{\alpha}_3$ can evolve as $\underset{\approx}{C}_o$ and $\underset{\approx}{\tilde{B}}_3$ do not evolve and are treated as implicit constants. The rational for choosing of $\underset{\approx}{\tilde{B}}_3$ as our basis is explained in Section 3.10.2, however, the ultimate selection of this particular basis is not critical. It is more important to emphasize that the modified failure function depends on the current stress state and $\Delta\tilde{\alpha}_3$.

3.12 Use of the Distortion Operator Introduces Anisotropy

The use of the distortion operator, $\underset{\approx}{L}$, allows what is otherwise an isotropic function to have an anisotropic component. The operator $\underset{\approx}{L}$ starts as the fourth-order identity in the initial state, but once deformation starts, $\underset{\approx}{L}$ becomes an anisotropic tensor. Consider Equation (62), the function F is an isotropic function for the undeformed state. Through the use of $\underset{\approx}{L}$, which has the same eigenprojectors as the elastic compliance, the stress tensor, $\underset{\approx}{\sigma}$, is distorted in such a manner that the resulting function f is itself distorted.

For example, the von Mises function is isotropic and when used with the evolved stress becomes

$$F\left(\underset{\approx}{\sigma}\right) = dev\left(\underset{\approx}{\sigma}\right) : dev\left(\underset{\approx}{\sigma}\right) - k^2 \qquad (67)$$

where $dev\left(\underset{\approx}{\sigma}\right)$ is the deviatoric component of the second-order stress tensor and k is a constant. By itself, $\partial F / \partial \underset{\approx}{\sigma}$ as defined by the von Mises function contains only deviatoric components, but through the use of the distortion operator, $\underset{\approx}{L}$, an isotropic part is introduced.

Consider the following applied to the von Mises function

$$\frac{\partial f}{\partial \underset{\approx}{\sigma}} = \frac{\partial F}{\partial \underset{\approx}{\sigma}^*} : \frac{\partial \underset{\approx}{\sigma}^*}{\partial \underset{\approx}{\sigma}} \qquad (68)$$

where $\frac{\partial F}{\partial \underset{\approx}{\sigma}^*} = 2\ dev\left(\underset{\approx}{\sigma}\right)$ and $\frac{\partial \underset{\approx}{\sigma}^*}{\partial \underset{\approx}{\sigma}} = \underset{\approxeq}{C_o} : \underset{\approxeq}{C}^{-1} = \underset{\approxeq}{L}$ as shown by Equation (22). The partial $\frac{\partial F}{\partial \underset{\approx}{\sigma}^*}$ returns only the deviatoric part of $\underset{\approx}{\sigma}$ (i.e., $tr\left(\frac{\partial F}{\partial \underset{\approx}{\sigma}^*}\right) = 0$). As long as $\underset{\approxeq}{L} \neq \underset{\approxeq}{I}$, $\underset{\approxeq}{L}$ will introduce an anisotropic component to $\partial f / \partial \underset{\approx}{\sigma}$. Equation (68) can be rewritten as

$$\frac{\partial f}{\partial \underset{\approx}{\sigma}} = \left(2dev\left(\underset{\approx}{\sigma}^*\right)\right) : \underset{\approxeq}{C_o} : \underset{\approxeq}{C}^{-1} \tag{69}$$

Introducing Equation (65) into Equation (69) yields

$$\frac{\partial f}{\partial \underset{\approx}{\sigma}} = 2dev\left(\underset{\approx}{\sigma}^*\right) + 4G_o \Delta\tilde{\alpha}_3\, dev\left(\underset{\approx}{\sigma}^*\right) : \underset{\approxeq}{\tilde{B}_3} \tag{70}$$

where G_o is the shear modulus of the undeformed matrix.

The trace of Equation (70) becomes

$$tr\left(\frac{\partial f}{\partial \underset{\approx}{\sigma}}\right) = \left(\frac{\partial f}{\partial \underset{\approx}{\sigma}}\right) : \underset{\approx}{I} = \underbrace{tr\left(2dev\left(\underset{\approx}{\sigma}^*\right)\right)}_{0} : \underset{\approx}{I} + 4G_o \Delta\tilde{\alpha}_3\, dev\left(\underset{\approx}{\sigma}^*\right) : \underset{\approxeq}{\tilde{B}_3} : \underset{\approx}{I} \tag{71}$$

The deviatoric component of $\underset{\approx}{\sigma}^*$ for TXC loading is given by

$dev\left[\underset{\approx}{\sigma}^*\right] = \frac{\sigma_A^* - \sigma_L^*}{3}\begin{bmatrix} -1 & 0 & 0 \\ 0 & -1 & 0 \\ 0 & 0 & 2 \end{bmatrix}$. Substitution of $dev\left(\underset{\approx}{\sigma}^*\right)$, and $\underset{\approxeq}{\tilde{B}_3}$ into Equation (71) gives

$$tr\left(\frac{\partial f}{\partial \underset{\approx}{\sigma}}\right) \rightarrow -8G_o \Delta\tilde{\alpha}_3 \frac{\sigma_A^* - \sigma_L^*}{3} \tag{72}$$

Noting that in Equation (72), the term $\frac{\sigma_A^* - \sigma_L^*}{3}$ is compressive for TXC loading and has a negative value. The net result of Equation (72) is that $tr\left(\partial f / \partial \underset{\approx}{\sigma}\right) > 0$ and shows that dilation results. *This result is extremely important in that dilatation has been introduced* *through the use of the distortion operator,* $\underset{\approx}{L}$*, and does not require an increase in hydrostatic strength.*

4. DISTORTION OPERATOR IN ELASTIC/PLASTIC ANALYSIS

The following sections deal with the use of the distortion operator $\underset{\approx\!\approx}{L}$ in the analysis of TXC data.

4.1 Expressions for the Hydrostatic Leg and Shear Leg During TXC

Traditional triaxial compression (TXC) consists of a hydrostatic leg followed by the triaxial compression leg, where the lateral stresses, σ_L, are held constant and the axial stress, σ_A, is varied. For the hydrostatic leg, the stresses are equal, and the hydrostatic stress at the end of the hydrostatic leg, $\underset{\approx}{\sigma}_H$, can be written as $\underset{\approx}{\sigma}_H = P^{bath}\underset{\approx}{I}$ where P^{bath} is the bath pressure and is taken as positive in compression. The triaxial compression portion of the test allows the stresses to be written as

$$\underset{\approx}{\sigma}_{TXC} = \sigma_A \underset{\sim}{m}\underset{\sim}{m} + P^{bath}\left(\underset{\approx}{I} - \underset{\sim}{m}\underset{\sim}{m}\right) \tag{73}$$

During the triaxial compression leg, the elastic strain can be written using Equations (65) and (73) as

$$\begin{aligned}\underset{\approx}{\varepsilon}^{e} &= \sigma_A\left(\underset{\approx\!\approx}{C}_o^{-1} : \underset{\sim}{m}\underset{\sim}{m}\right) + P^{bath}\left(\underset{\approx\!\approx}{C}_o^{-1} : \left(\underset{\approx}{I} - \underset{\sim}{m}\underset{\sim}{m}\right)\right) \\ &\quad + \Delta\tilde{\alpha}_3\sigma_A\left(\underset{\approx\!\approx}{\tilde{B}}_3 : \underset{\sim}{m}\underset{\sim}{m}\right) + \Delta\tilde{\alpha}_3 P^{bath}\left(\underset{\approx\!\approx}{\tilde{B}}_3 : \left(\underset{\approx}{I} - \underset{\sim}{m}\underset{\sim}{m}\right)\right)\end{aligned} \tag{74}$$

where $\underset{\approx\!\approx}{C}_o^{-1}$ is the compliance of the undeformed material. It is assumed that linear elasticity applies for the undeformed material and setting setting $\underset{\sim}{m} = \begin{bmatrix}0 & 0 & 1\end{bmatrix}^T$, the term $\underset{\approx\!\approx}{C}_o^{-1} : \underset{\sim}{m}\underset{\sim}{m}$ in Equation (74) is evaluated as

$$\underset{\approx\!\approx}{C}_o^{-1} : \underset{\sim}{m}\underset{\sim}{m} = \frac{1}{E_o}\underset{\sim}{m}\underset{\sim}{m} - \frac{\nu_o}{E_o}\left(\underset{\approx}{I} - \underset{\sim}{m}\underset{\sim}{m}\right) \tag{75}$$

The term $\underset{\approx}{\underset{\approx}{C}}_o^{-1}:\left(\underset{\approx}{I}-\underset{\sim}{m}\underset{\sim}{m}\right)$ can be written as

$$\underset{\approx}{\underset{\approx}{C}}_o^{-1}:\left(\underset{\approx}{I}-\underset{\sim}{m}\underset{\sim}{m}\right)=-\frac{2\nu_o}{E_o}\underset{\sim}{m}\underset{\sim}{m}+\frac{1-\nu_o}{E_o}\left(\underset{\approx}{I}-\underset{\sim}{m}\underset{\sim}{m}\right) \tag{76}$$

The term $\underset{\approx}{\underset{\approx}{\tilde{B}}}_3:\underset{\sim}{m}\underset{\sim}{m}$ becomes

$$\underset{\approx}{\underset{\approx}{\tilde{B}}}_3:\underset{\sim}{m}\underset{\sim}{m}=\frac{1}{2}\left(\underset{\approx}{I}-\underset{\sim}{m}\underset{\sim}{m}\right) \tag{77}$$

The term $\underset{\approx}{\underset{\approx}{\tilde{B}}}_3:\left(\underset{\approx}{I}-\underset{\sim}{m}\underset{\sim}{m}\right)$ results in

$$\underset{\approx}{\underset{\approx}{\tilde{B}}}_3:\left(\underset{\approx}{I}-\underset{\sim}{m}\underset{\sim}{m}\right)=\underset{\sim}{m}\underset{\sim}{m}+\frac{3}{2}\left(\underset{\approx}{I}-\underset{\sim}{m}\underset{\sim}{m}\right) \tag{78}$$

Inserting Equations (75)-(78) into Equation (74) gives

$$\begin{aligned}\underset{\approx}{\varepsilon}^e=&\left(\underset{\sim}{m}\underset{\sim}{m}\right)\left[\frac{\sigma_A}{E_o}+\Delta\tilde{\alpha}_3P^{bath}-P^{bath}\frac{2\nu_o}{E_o}\right]\\&+\left(\underset{\approx}{I}-\underset{\sim}{m}\underset{\sim}{m}\right)\left[-\sigma_A\frac{\nu_o}{E_o}+\frac{\sigma_A\Delta\tilde{\alpha}_3}{2}+P^{bath}\frac{\left(1-\nu_o\right)}{E_o}+\frac{3}{2}\Delta\tilde{\alpha}_3P^{bath}\right]\end{aligned} \tag{79}$$

The axial elastic strain, ε_A^e, is the coefficient of $\underset{\sim}{m}\underset{\sim}{m}$, and the lateral elastic strain, ε_L^e, is the coefficient of $\underset{\approx}{I}-\underset{\sim}{m}\underset{\sim}{m}$. Specifically,

$$\varepsilon_A^e=\frac{\sigma_A}{E_o}+P^{bath}\left(\Delta\tilde{\alpha}_3-\frac{2\nu_o}{E_o}\right) \tag{80}$$

$$\varepsilon_L^e=\sigma_A\left(-\frac{\nu_o}{E_o}+\frac{\Delta\tilde{\alpha}_3}{2}\right)+P^{bath}\left(\Delta\tilde{\alpha}_3\frac{3}{2}+\frac{\left(1-\nu_o\right)}{E_o}\right) \tag{81}$$

4.2 Approximate Expressions for a Brittle Material Tested by TXC

During the first leg of a typical TXC test, the loading is purely hydrostatic in nature. At a set pressure, the loading then changes with the axial load increasing, while the lateral stresses are held constant. As the load increases, the Kayenta model hardens the yield surface as illustrated in **Figure 20**(a). The loading path is shown as the blue line. The dashed red lines represent evolving yield surfaces according to Kayenta's hardening model, and the black arrows are the normals to the yield surfaces.

As the shear loading increases, the material will reach a limit surface. This surface can be approximated by an affine yield function as shown in **Figure 20**(b). Using such an approximation, the angle of inclination of the line, β, can be correlated to the surface normal, $\underset{\approx}{N}$.

For this analysis, the loading path will correspond to the following times:

$$\begin{array}{rl} \text{Hydrostatic,} & 0 \leq t \leq t_{TXC} \\ \text{Triaxial compression} & \begin{cases} t_{TXC} < t < t_Y \\ t_Y \leq t < t_{End} \end{cases} \end{array}$$

where t_{TXC} is the time at which the TXC leg starts, t_Y is the time at which the yield/limit surface is reached, and t_{End} represents the time at which the test ends. At $t = t_Y$, the TXC leg reaches the affine limit surface (red line) at $\sqrt{J_2(t_Y)}$ as shown in **Figure 20**(c). In addition, a von Mises surface (blue line) is set to correspond to the shear value $\sqrt{J_2(t_Y)}$. The motivation for setting these surfaces coincident is discussed in a subsequent section. Normals to the von Mises and affine limit surfaces are designated by the dashed blue line and red line, respectively. Since the von Mises function is isotropic, the von Mises and affine limit surfaces in $\sqrt{J_2}$ - $\bar{I}_1$ space can be represented by conical and cylindrical surfaces, respectively. These surfaces are shown in **Figure 20**(d).

4.3 Consideration of Forms for a Modified Compliance

This thesis seeks an alternative means of predicting the qualitative features seen in TXC experiments (especially dilatation) by introducing anisotropic degradation of elastic

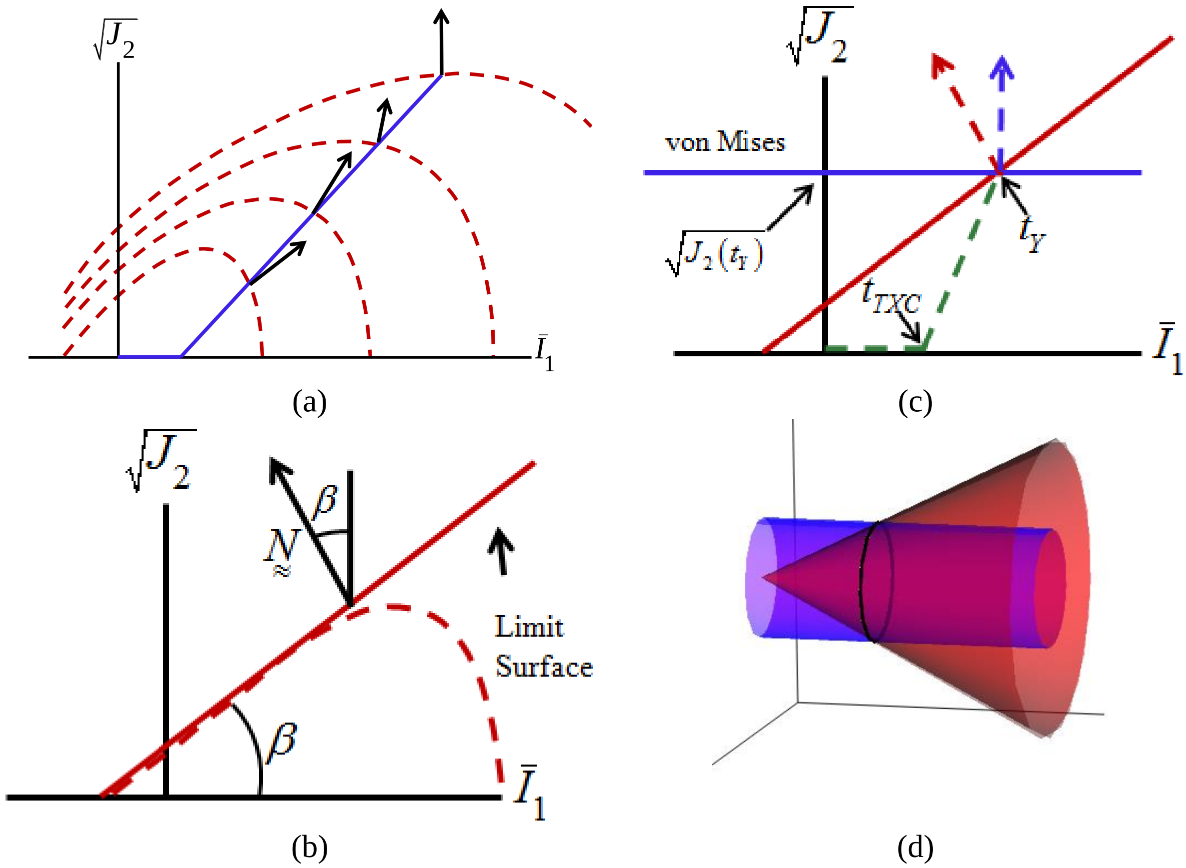

Figure 20. Load paths and yield/limit surfaces in $\sqrt{J_2}$ - $\bar{I}_1$ space: (a) evolving yield surface, (b) affine approximation of limit surface, (c) affine and von Mises limit surface and loading path for TXC, (d) von Mises and affine limit surface.

stiffness as a way to avoid the unrealistic prediction of increased hydrostatic yield strength with dilation that is intrinsic in the Kayenta formulation. For this purpose, the stress is taken as a linear function of the elastic strain, $\underset{\approx}{\sigma} = \underset{\approx\approx}{C} : \underset{\approx}{\varepsilon}^e$ where the reduction in stress from softening is achieved by reducing the elastic compliance tensor. Because a TXC experiment is run in stress control, it is more convenient to write

$$\underset{\approx}{\varepsilon}^e = \underset{\approx\approx}{C}^{-1} : \underset{\approx}{\sigma} = \left(\underset{\approx\approx}{C}_o^{-1} + \Delta\tilde{\alpha}_3 \underset{\approx\approx}{\tilde{B}}_3 \right) : \underset{\approx}{\sigma} \tag{82}$$

During the hydrostatic leg of the experiment, it is assumed that the pore-free bulk material properties remain isotropic, and the development of oriented cracks does not occur until later in the shear leg. Under these assumptions, $\Delta\tilde{\alpha}_3$ is zero until the development of cracks. Then, $\Delta\tilde{\alpha}_3$ increases in an undetermined manner (the exact form of $\Delta\tilde{\alpha}_3$ is not established here) until the end of the test ($t = t_{End}$).

Determination of the evolution law for $\Delta\tilde{\alpha}_3$ would require laboratory testing or mesoscale modeling beyond the scope of this thesis. In this text, the aim is limited to merely demonstrating that a monotonic increase in $\Delta\tilde{\alpha}_3$ at time t_Y is capable of causing an apparent dilatation. For this purpose, it is sufficient to consider a linear function of the following form

$$\Delta\tilde{\alpha}_3(t) = K_{\Delta\tilde{\alpha}_3} \cdot \langle t - t_Y \rangle \tag{83}$$

where $K_{\Delta\tilde{\alpha}_3}$ is a constant and $\langle t - t_Y \rangle = \begin{cases} 0, & t < t_Y \\ t - t_Y, & t_Y \le t \end{cases}$ is the Macaulay bracket.

Since the derivative of the Macaulay brackets is the Heaviside function, the time derivative of Equation (83) is

$$\Delta\dot{\tilde{\alpha}}_3 = \frac{d\Delta\tilde{\alpha}_3}{dt} = K_{\Delta\tilde{\alpha}_3} \cdot H\left[t - t_Y\right] \tag{84}$$

4.4 Rate-Independent Plasticity Relations

Assuming that $\Delta\tilde{\alpha}_3$ is of the form shown by Equation (83), the rate-independent plasticity relations are derived in this section. Following Brannon [91], especially with regard to the treatment of elastic-plastic coupling (*Z*-tensor below), the following governing relations can be defined

$$\text{Strain rate decomposition: } \underset{\approx}{\dot{\varepsilon}} = \underset{\approx}{\dot{\varepsilon}}^e + \underset{\approx}{\dot{\varepsilon}}^p \tag{85}$$

$$\text{Nonlinear coupled elasticity: } \underset{\approx}{\dot{\sigma}} = \underset{\approx\approx}{C} : \underset{\approx}{\dot{\varepsilon}}^e - \underset{\approx}{Z}\,\dot{\lambda} \tag{86}$$

$$\text{Flow rule: } \underset{\approx}{\dot{\varepsilon}}^p = \dot{\lambda}\,\underset{\approx}{M} \tag{87}$$

$$\text{Consistency: } \underset{\approx}{N} : \underset{\approx}{\dot{\sigma}} = H\dot{\lambda} \tag{88}$$

where the superimposed dot denotes a rate, and

- $\underset{\approx}{\dot{\varepsilon}}$ is the total strain rate.

- $\dot{\underset{\approx}{\varepsilon}}^e$ is the elastic part of the strain rate.
- $\dot{\underset{\approx}{\varepsilon}}^p$ is the plastic part of the strain rate.
- $\dot{\underset{\approx}{\sigma}}$ is the rate of stress.
- $\underset{\approx\approx}{C}$ is the elastic tangent stiffness tensor.
- $\underset{\approx}{Z}$ is the elastic-plastic coupling tensor.
- $\dot{\lambda}$ is the consistency parameter.
- $\underset{\approx}{M}$ is the unit tensor in the direction of plastic strain.
- $\underset{\approx}{N}$ is the unit normal to the yield surface.
- H is the ensemble hardening modulus.

Unless clearly defined otherwise, associativity will be assumed (i.e., $\underset{\approx}{M} = \underset{\approx}{N}$).

For this analysis, certain quantities are presumed known: $\dot{\sigma}$, $\underset{\approx\approx}{C}$, $\Delta\tilde{\alpha}_3$, $\Delta\dot{\tilde{\alpha}}_3$, $\underset{\approx\approx}{\tilde{B}_3}$, $\underset{\approx\approx}{C_o}$, and $\underset{\approx}{N} = \underset{\approx}{M}$ (found in a subsequent subsection).

The unknown quantities are $\dot{\underset{\approx}{\varepsilon}}$, $\dot{\underset{\approx}{\varepsilon}}^e$, $\dot{\underset{\approx}{\varepsilon}}^p$, $\dot{\lambda}$, h (constant determined from $\Delta\dot{\tilde{\alpha}}_3 = h\dot{\lambda}$), $\underset{\approx}{Z}$, and H. The unknown quantities are determined in the following subsections.

4.4.1 Determination of Plasticity Parameters

In a triaxial compression test, the stress rate is known, and the strain rate is unknown. As a result, Equations (85)-(88) will be combined and cast in the form of the strain rate. Equation (88) can be rearranged to give the consistency parameter

$$\dot{\lambda} = \frac{\underset{\approx}{N} : \dot{\underset{\approx}{\sigma}}}{H} \tag{89}$$

Once $\dot{\lambda}$ is known, an evolution law of the following form can be cast

$$\Delta\dot{\tilde{\alpha}}_3 = h\dot{\lambda} \Rightarrow h = \frac{\Delta\dot{\tilde{\alpha}}_3}{\dot{\lambda}} \tag{90}$$

and h can be determined.

Solving Equation (86) for $\dot{\underset{\approx}{\varepsilon}}^e$ and substituting $\dot{\lambda}$ gives the elastic strain rate

$$\dot{\underset{\approx}{\varepsilon}}^{e} = \underset{\approx}{\underset{\approx}{C}}^{-1} : \dot{\underset{\approx}{\sigma}} + \underset{\approx}{\underset{\approx}{C}}^{-1} : \underset{\approx}{Z}\left(\frac{\underset{\approx}{N} : \dot{\underset{\approx}{\sigma}}}{H}\right) \tag{91}$$

Substitution of Equation (89) into Equation (87) results in the plastic strain rate

$$\dot{\underset{\approx}{\varepsilon}}^{p} = \underset{\approx}{M}\left(\frac{\underset{\approx}{N} : \dot{\underset{\approx}{\sigma}}}{H}\right) \tag{92}$$

From Equations (85), (91), and (92), the total strain rate becomes

$$\dot{\underset{\approx}{\varepsilon}} = \underset{\approx}{\underset{\approx}{T}}^{-1} : \dot{\underset{\approx}{\sigma}} \tag{93}$$

where $\underset{\approx}{\underset{\approx}{T}}^{-1} = \underset{\approx}{\underset{\approx}{C}}^{-1} + \underset{\approx}{\underset{\approx}{C}}^{-1} : \frac{\underset{\approx}{Z}\,\underset{\approx}{N}}{H} + \frac{\underset{\approx}{M}\,\underset{\approx}{N}}{H}$ is the elastic-plastic tangent compliance tensor.

4.4.2 Triaxial Compression Expressions for Strain Rates

In Equation (91), the elastic strain rate is given in tensorial form. In the case of TXC, the axial and lateral strain rates can be found from Equations (80) and (81).

The axial strain rate is found using

$$\dot{\varepsilon}_A = \frac{\dot{\sigma}_A}{E_o} + \dot{P}^{Bath}\left(-2\frac{\nu_o}{E_o}\right) \text{ and } \dot{\sigma}_A = \dot{P}_{Bath} \qquad \text{At time, } t < t_Y$$

Using Equation (84) results in

$$\dot{\varepsilon}_A = \frac{\dot{\sigma}_A}{E_o}\left(1 - 2\nu_o\left(1 - H\left(t - t_Y\right)\right)\right) + P^{Bath} K_{\Delta\tilde{\alpha}_3} H\left(t - t_Y\right) \tag{94}$$

Solving for the lateral strain rate and using Equation (83) and(84) gives

$$\begin{aligned} \dot{\varepsilon}_L = {} & \dot{\sigma}_A\left(\frac{\left(1-2\nu_o\right) - \left(1-\nu_o\right)H\left(t-t_Y\right)}{E_o} + \frac{K_{\Delta\tilde{\alpha}_3}\left\langle t - t_Y\right\rangle}{2}\right) \\ & + \left(\frac{\sigma_A}{2} + \frac{3P^{Bath}}{2}\right) K_{\Delta\tilde{\alpha}_3} H\left(t - t_Y\right) \end{aligned} \tag{95}$$

4.4.3 Determination of the Elastic-Plastic Coupling Tensor

Assuming some compliance of the form given by Equation (65), an evolving elastic stiffness tensor can be written as a function of $\Delta\tilde{\alpha}_3$. The stress is $\underset{\approx}{\sigma} = \underset{\approx}{\underset{\sim}{C}}\left(\Delta\tilde{\alpha}_3\right) : \underset{\approx}{\varepsilon}^e$. If the stress is written as an increment, the resulting stress rate becomes

$$\dot{\underset{\approx}{\sigma}} = \underset{\approx}{\underset{\sim}{C}}\left(\Delta\tilde{\alpha}_3\right) : \dot{\underset{\approx}{\varepsilon}}^e + \left(\frac{d\,\underset{\approx}{\underset{\sim}{C}}\left(\Delta\tilde{\alpha}_3\right)}{d\Delta\tilde{\alpha}_3} \Delta\dot{\tilde{\alpha}}_3 \right) : \underset{\approx}{\varepsilon}^e \tag{96}$$

The derivative, $d\,\underset{\approx}{\underset{\sim}{C}}\left(\Delta\tilde{\alpha}_3\right) \Big/ d\Delta\tilde{\alpha}_3$, in Equation (96) can be found using $\underset{\approx}{\underset{\sim}{C}} : \underset{\approx}{\underset{\sim}{C}}^{-1} = \underset{\approx}{\underset{\sim}{I}}$, the differential product rule, and the compliance given by Equation (65) with the result of

$$\frac{d\,\underset{\approx}{\underset{\sim}{C}}}{d\Delta\tilde{\alpha}_3} = -\underset{\approx}{\underset{\sim}{C}} : \underset{\approx}{\underset{\sim}{\tilde{B}_3}} : \underset{\approx}{\underset{\sim}{C}} \tag{97}$$

Equation (96) becomes

$$\dot{\underset{\approx}{\sigma}} = \underset{\approx}{\underset{\sim}{C}}\left(\Delta\tilde{\alpha}_3\right) : \dot{\underset{\approx}{\varepsilon}}^e + \left(-\underset{\approx}{\underset{\sim}{C}} : \underset{\approx}{\underset{\sim}{\tilde{B}_3}} : \underset{\approx}{\underset{\sim}{C}} \right) \Delta\dot{\tilde{\alpha}}_3 : \underset{\approx}{\varepsilon}^e \tag{98}$$

Noting that degradation of the elastic compliance occurs only during inelastic loading, the rate of $\Delta\dot{\tilde{\alpha}}_3$ is presumed to be structured such that $\Delta\tilde{\alpha}_3$ evolves in proportion to the plastic strain. In other words, consistent with classical plasticity formulations, it is assumed that a state-dependent material function, h, exists such that $\Delta\dot{\tilde{\alpha}}_3 = h\dot{\lambda}$ where $\dot{\lambda}$ is a consistency parameter. Substitution of $\Delta\dot{\tilde{\alpha}}_3$ into Equation (98) yields

$$\dot{\underset{\approx}{\sigma}} = \underset{\approx}{\underset{\sim}{C}}\left(\Delta\tilde{\alpha}_3\right) : \dot{\underset{\approx}{\varepsilon}}^e - \underset{\approx}{Z}\,\dot{\lambda} \tag{99}$$

where $\underset{\approx}{Z} = \left(\underset{\approx}{\underset{\sim}{C}} : \underset{\approx}{\underset{\sim}{\tilde{B}_3}} : \underset{\approx}{\underset{\sim}{C}} \right) : \underset{\approx}{\varepsilon}^e\, h$ and is defined as the elastic-plastic coupling tensor.

4.4.4 Determination of the Ensemble Hardening Modulus

The ensemble hardening modulus, H, is defined as

$$H = \frac{-\left(\frac{\partial f}{\partial \Delta \tilde{\alpha}_3} h\right)}{\left\| \frac{\partial f}{\partial \underset{\approx}{\sigma}} \right\|} \tag{100}$$

The ensemble hardening modulus accounts for the total effect of all internal state variables changing at the same time, and results in movement of the yield surface. The parameter H accounts for the consistency condition, which ensures that the stress state remains on the yield surface during inelastic loading [91].

As described in Section 4.2, the limit surface is described by a von Mises function, which is set coincident to an affine limit surface. The function used in Equation (100) is given by $f\left(\underset{\approx}{\sigma}\right) = F\left(\underset{\approx\approx}{L} : \underset{\approx}{\sigma}\right)$. The denominator in Equation (100), $\partial f / \partial \underset{\approx}{\sigma}$, is given by Equation (70), h in the numerator is defined by Equation (90). The partial $\partial f / \partial \Delta \tilde{\alpha}_3$ can be found from the chain law $\partial f / \partial \Delta \tilde{\alpha}_3 = \partial F / \partial \underset{\approx}{\sigma}^* : \partial \underset{\approx}{\sigma}^* / \partial \Delta \tilde{\alpha}_3$ and through the use of $f\left(\underset{\approx}{\sigma}\right) = F\left(\underset{\approx\approx}{L} : \underset{\approx}{\sigma}\right)$. The term $\partial F / \partial \underset{\approx}{\sigma}^* = 2\ dev\left(\underset{\approx}{\sigma}\right)$ as initially discussed in Equation (68). The partial $\partial \underset{\approx}{\sigma}^* / \partial \Delta \tilde{\alpha}_3$ is determined as

$$\frac{\partial \sigma^*}{\partial \Delta \tilde{\alpha}_3} = \underset{\approx\approx}{C_o} : \underset{\approx\approx}{\tilde{B}_3} : \underset{\approx}{\sigma} \tag{101}$$

Substituting Equations (70) and (101) into Equation (100) and using $\underset{\approx}{\sigma}^* = \underset{\approx\approx}{L} : \underset{\approx}{\sigma}$ yields

$$H = \frac{-\left(\left(2\ dev\left(\underset{\approx}{\sigma}\right)\right) : \left(\underset{\approx\approx}{C_o} : \underset{\approx\approx}{\tilde{B}_3} : \underset{\approx}{\sigma}\right)\right) h}{\left\| 2 dev\left(\underset{\approx\approx}{L} : \underset{\approx}{\sigma}\right) + 4G\Delta\tilde{\alpha}_3\, dev\left(\underset{\approx\approx}{L} : \underset{\approx}{\sigma}\right) : \underset{\approx\approx}{\tilde{B}_3} \right\|} \tag{102}$$

4.5 Quantification of the Degree of Dilatation

As discussed in Section 3.12, the von Mises yield criterion is defined purely in terms of the deviatoric part of the stress. When the stress is written in terms of the distortion operator, $\underset{\approx}{\sigma}^* = \underset{\approx\approx}{L} : \underset{\approx}{\sigma}$, a dilatational component is introduced. The angle β as shown in

Figure 21 (assuming associativity), quantifies that degree of dilatation, which is zero prior the introduction of $\underset{\approx}{\sigma}^{*}$. The vector $\underset{\sim}{N}\left(\underset{\approx}{\sigma}\right)$ (blue arrow) represents the normal to the von Mises limit surface (blue line) and is defined by Equation (70). As $\Delta\tilde{\alpha}_3$ in Equation (70) increases, so does the dilatational contribution. This change is represented by the vector $\underset{\sim}{N}\left(\underset{\approx}{\sigma}^{*}\right)$ (red arrow).

Recall from Equation (19) that the anisotropic yield function f is given by a von Mises yield function F applied to an anisotropically transformed stress; namely $f\left(\underset{\approx}{\sigma}\right) = F\left(\underset{\approx}{\underset{\approx}{L}} : \underset{\approx}{\sigma}\right)$. Accordingly, the angle of inclination, β, can be determined from the isotropic and deviatoric parts of $\dfrac{\partial f}{\partial \underset{\approx}{\sigma}}$ (as shown in **Figure 21**), which may be found using the chain rule. Then in "isomorphic" stress space (which is the projection of the stress tensor onto the hyperplane spanned by the stress deviator and the identity, as sketched in **Figure 21**), $\tan(\beta)$ can be defined as

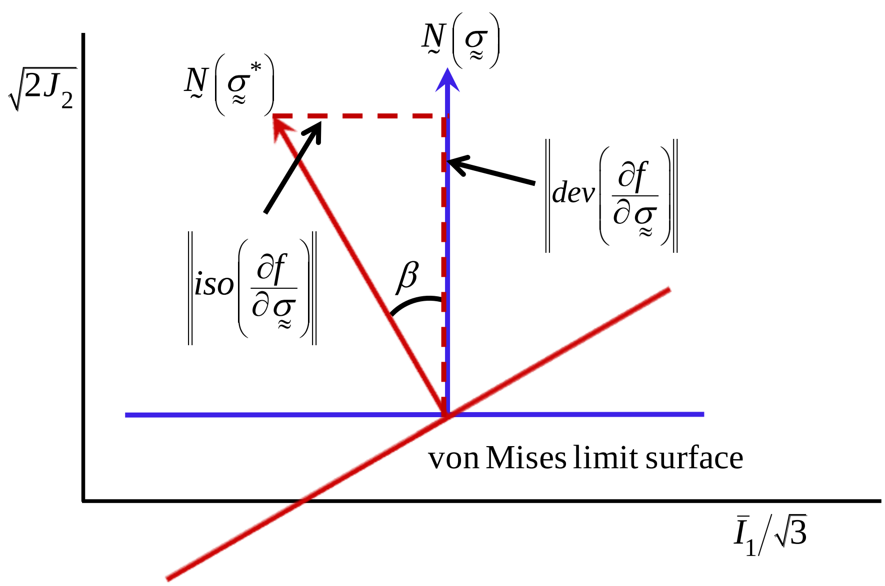

Figure 21. The angle β is a measure of the degree of dilatation as determined from a von Mises limit surface (which is purely deviatoric).

$$\tan(\beta) = \frac{\left\| iso\left(\frac{\partial f}{\partial \underset{\approx}{\sigma}} \right) \right\|}{\left\| dev\left(\frac{\partial f}{\partial \underset{\approx}{\sigma}} \right) \right\|} \tag{103}$$

The term $\tan(\beta)$ is determined in Appendix C with the result of

$$\Delta\tilde{\alpha}_3 = \frac{1}{G_o}\left(\frac{3\sqrt{2}\tan(\beta)}{4+\sqrt{2}\tan(\beta)} \right) \tag{104}$$

A plot of the CEF $\Delta\tilde{\alpha}_3$ versus $\beta \left(0 \le \beta < \frac{\pi}{2} \right)$ is shown in **Figure 22** (assuming $G_o = 5\times10^6 \text{ psi}$). It can be seen from the figure, that as β approaches $\frac{\pi}{2}$, $\Delta\tilde{\alpha}_3$ starts to

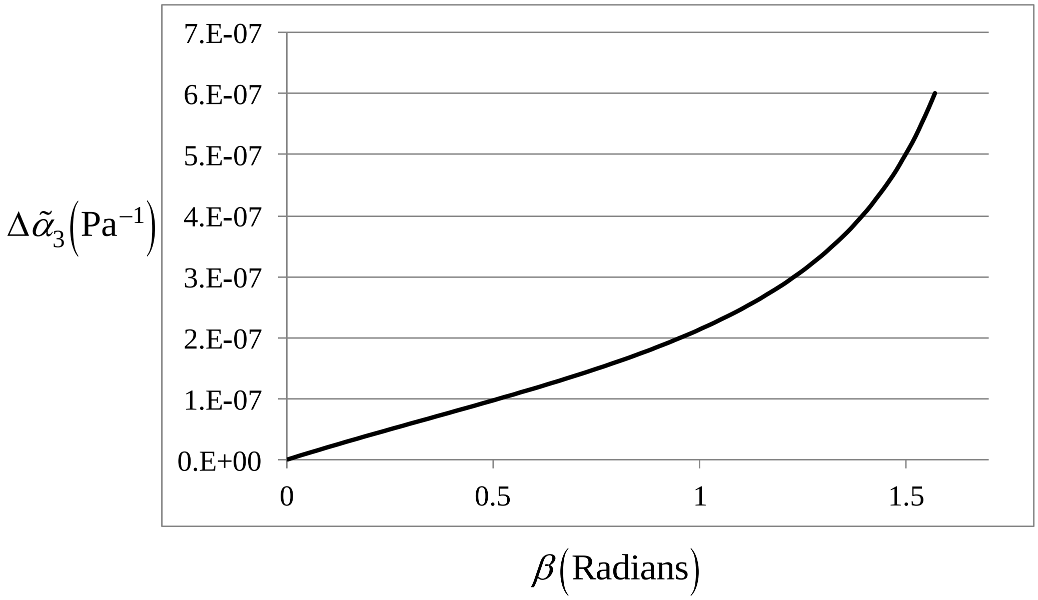

Figure 22. A plot of $\Delta\tilde{\alpha}_3$ versus β.

increase nonlinearly. On a qualitative basis, β represents a measure of dilatation, and $\Delta\tilde{\alpha}_3$ varies in proportion to the number-density function $F_\rho\left(\underset{\sim}{n}, t\right)$, defined in Section 3.4.

Therefore, Figure 22 demonstrates that dilatation in triaxial compression (i.e., nonzero β*) can indeed be predicted as a result of lateral strains induced from axial stress in triaxial compression (which is the stress-strain coupling implied by a nonzero value of* $\Delta\tilde{\alpha}_3$*)*

.

5. SUMMARY AND CONCLUSIONS

This thesis studied a cap evolution law based on the work of Warren et al. [1] (referenced in this work as the Kayenta Model) and is motivated by the phenomenon of porous media dilatation in triaxial compression (TXC). During typical TXC loading, the material is initially hydrostatically compressed with the possible result of compaction. Then, the lateral stresses are held constant as the axial stress is increased, leading to dilatation. The Kayenta model assumes an isotropic yield model with porosity as an internal state variable. During TXC, the Kayenta cap evolution law is capable of modeling compaction followed by dilatation, but it does so by counter-intuitively increasing the hydrostatic compressive strength when dilatation is occurring, which is behavior that has never been validated (or invalidated) in the laboratory. The work conducted in this thesis presents an alternative approach to modeling TXC dilatation.

Within the thesis text, a review of the Kayenta cap function is presented. The cap function models the presence of porosity and microcracks as two separate functions, which are combined into a single entity. Dilatation is controlled by a fracture function that is a phenomenological fit of experimental data and is identical to a limit function as if the material has microcracks but no porosity. Compaction is described by a cap function that accounts for the presence of pores and assumes no change in volume until a branch point is reached. A yield function is constructed by multiplying the fracture and cap functions together.

A literature review is conducted on the following topics:

- *Experimental evidence supporting the Kayenta cap evolution law* - No evidence is found to either support or invalidate the model's cap behavior. Testing is exclusively focused on initially hydrostatically loading the specimens and then loading the material in triaxial compression. Very little documentation exists of loading cases where the load profile is successfully varied beyond the typical TXC loading pattern (with the exception of cyclic loading). Attempts to perform such experiments were inconclusive.
- *Other yield models that include a cap* – Several other modeling efforts contained a cap in their description. Many consisted of two different yielding functions; one for the shear envelope and the other for compaction. For a significant number of these models, the cap function is nonsmooth, which can lead to integration difficulties.
- *Experimental evidence of inelastically induced anisotropy resulting from triaxial compression, and incorporation of anisotropy into constitutive models* – Substantial experimental evidence documenting TXC induced anisotropy exists. A wide variety of theoretical approaches to incorporating anisotropy is reported; including rotation of the yield surface around the origin in stress space, distorted ellipsoids incorporated into the yield surface, reduction of compliance in a particular direction, etc.
- Mesoscale modeling that analyzes yield surfaces – Several publications report the use of mesoscopic model to predict failure surface. Many of these publications

incorporated transversely anisotropic behavior into their models by reducing the compliance in the lateral directions.

To suppress unrealistic strengthening, an anisotropically transformed stress is used in an isotropic yield model. The stress is transformed through the use of an anisotropic distortion operator. This operator has the same eigenvalues as the elastic compliance and is constructed as a combination of the undeformed stiffness and the deformed compliance. The operator starts as the fourth-order identity in the initial state, but once deformation initiates; it evolves to a symmetric anisotropic tensor. The transformed stress is then sent to an isotropic yield function with the result of a new anisotropic function.

A transversely isotropic compliance is presented, based on a linear combination of natural bases constructed about an isotropic axis. Five basis terms are included in the compliance expression. The resulting construct is compared to the compliance expressions of Dienes et al. and Kachanov. The Dienes and Kachanov compliance expressions resulted from an ensemble of microcracks of all sizes and orientations. It is determined that the Kachanov expression is a special case of Dienes' theory. In their compliance formulations, they include two terms that correspond to two bases from the transversely isotropic compliance.

During TXC loading, cracks kink to become effectively aligned in the direction of axial loading. An axisymmetric probabilistic distribution of cracks is constructed for the case of transverse isotropy. A transversely isotropic compliance is formulated from a crack distribution that assumed that the only cracks of interest ran parallel to the axis of symmetry. The selected compliance is also based on terms that decreased the lateral stiffness, but left the axial stiffness unchanged. Based off of the presented compliance, it is demonstrated the distortion operator introduces anisotropy to an isotropic function, but does not require an increase in hydrostatic strength.

In the final section, a demonstration of how the distortion operator could be used in the elastic/plastic analysis of a von Mises surface loaded in TXC is presented. Specifically, the following quantities are calculated from the previously presented compliance:

- Elastic strains.
- Plastic strain.
- Modified compliance.
- Consistency parameter.
- Evolution law.
- Elastic-plastic coupling tensor.
- Ensemble hardening modulus.

In addition, a quantification of the degree of dilatation for a nominal von Mises surface distorted through the use of the distortion operator is presented.

The novel contributions of this work are

- An examination of the compliance expressions of Dienes et al. [84] and Kachanov [85] is performed. In their equations, Dienes clearly defines a number of cracks per unit volume along with a continuous crack size distribution, whereas Kachanov implies an equivalent term resulting from the summation over discrete crack sizes and orientations. Thus, Kachanov's theory is a special case of Dienes' theory. Both of these researchers, however, include compliance enhancement terms that accommodate additional strains only normal and/or tangential to the crack face. Neither researcher included compliance enhancement that allows an axial stress to induce additional lateral strain (beyond an ordinary Poisson effect). Recognition that only one of the five transverse basis tensors allows lateral strain enhancements in response to axial stress is a unique contribution of this research.
- A compliance expression for the special case of a damaged material with transverse isotropy was derived. In the undeformed state, the flaw orientations are presumed to be uniformly random in orientation. As the material is deformed by an increase in axial stress, the cracks will grow and rapidly kink to be parallel to the axial-load direction. However, because of the symmetry of loading, no bias is introduced in the dependence of the distribution on the meridian angle. Our compliance expression was reduced in form to focusing only on enhancement of the lateral strains (in addition to Poisson's effects) through selection of a specific transverse basis tensor that was capable of producing a lateral strain enhancement from an axial stress.
- It was shown to be possible for an isotropic function of stress to be used to construct an anisotropic function by simply applying the isotropic function to an anisotropically transformed stress argument. In particular, the stress sent to the isotropic function is given by an anisotropic distortion operator acting on the actual stress tensor. The distortion operator is a fourth-order tensor that starts in the undeformed state as the fourth-order identity, but once deformation commences, the operator becomes an anisotropic tensor. It was demonstrated that, for the von Mises function (which is purely deviatoric), the use of the distortion operator allowed for the introduction of dilatation without requiring an increase in hydrostatic strength. In addition, for the specific case of transverse isotropy, the distortion operator was used to derive the rate-independent plasticity equations.

5.1 Proposed Future Work

A number of areas worth investigating that are not specifically covered in this work are:

1. This thesis presented an alternative way of describing TXC data without predicting an increase in hydrostatic compressive strength when dilatation is occurring. This introduces the opportunity for mesoscale studies to help identify physics-based ISVs and their evolution laws, especially under changes in loading direction.

The $\underset{\approx}{\tilde{B}}_3$ basis is chosen to describe the compliance enhancement. In reality, a complete formulation for the compliance would include basis terms such as $\underset{\approx}{\tilde{B}}_1$ and/or $\underset{\approx}{\tilde{B}}_5$ following the lead of Dienes and Kachanov. Future work could include these terms in compliance expressions.

2. In the description of the compliance, it is assumed that all cracks are aligned along the axial direction. This assumption is justified for this thesis's limited scope of triaxial compression, since angled cracks can be assumed to immediately kink into the assumed orientation. A more realistic approach, applicable to arbitrary loading modes, would have the orientation of normals to the cracks determined through mesoscale modeling or experimental data.
3. A simple von Mises limit surface is analyzed through the use of the distortion operator, $\underset{\approx}{L}$. In this work, a qualitatively reasonable expression for the distortion tensor was to require it to describe a critical strain failure model. Accordingly the distortion tensor was formed as the product of the intact stiffness times the damaged compliance. Mesoscale analysis would be appropriate to validate or invalidate the existence of a critical strain failure criterion. Furthermore, if the failure surface is assumed to evolve from an isotropic to anisotropic form in a continuous manner (i.e., without forming yield surface vertices), then the approach taken in this thesis can be seen to be a first-order accurate description of the damage evolution process. A more thorough approach would be to use a higher-order model to describe the yield/limit surface. Furthermore, laboratory experiments and/or mesoscale modeling should be conducted to validate or invalidate the neglect of yield surface vertices.

6. REFERENCES

1. Warren, T. L., Fossum, A. F., and Frew, D. J., 2004, "Penetration into Low-Strength (23 MPa) Concrete: Target Characterization and Simulations," International Journal of Impact Engineering, 30, pp. 477-503.

2. Brannon, R. M., Fossum, A. F., and Strack, O. E., 2009, "Kayenta: Theory and User's Guide (SAND2009-2282),"Sandia National Laboratories, pp. 1-186.

3. Fanella, D., and Krajcinovic, D., 1988, "A Micromechanical Model for Concrete in Compression," Engineering Fracture Mechanics, 29(1), pp. 49-66.

4. Oka, F., Leroueil, S., and Tavenas, F., 1989, "Constitutive Model for Natural Soft Clay with Strain Softening," Soils and Foundations, 29(3), pp. 54-66.

5. Mellegard, K. D., and Pfeifle, T. W., 1999, "Laboratory Evaluation of Mechanical Properties of Rock Using an Automated Triaxial Compression Test with a Constant Mean Stress Criterion," ASTM Special Technical Publication, 1350, pp. 247-258.

6. Hoyos Jr, L. R., and Macari, E. J., 2000, "Nature of Principal Strain Response of Unsaturated Soils Under Multi-Axial Stress States," Geotechnical Special Publication, 99, pp. 333-343.

7. Mahnken, R., 2001, "Strength Difference in Compression and Tension and Pressure Dependence of Yielding in Elasto-Plasticity," Computer Methods in Applied Mechanics and Engineering, 190(39), pp. 5057-5080.

8. Batiste, S. N., Alshibli, K. A., Sture, S., and Lankton, M., 2004, "Shear Band Characterization of Triaxial Sand Specimens Using Computed Tomography," ASTM Geotechnical Testing Journal, 27(6), pp. 568-579.

9. Choi, C., Arduino, P., and Harney, M. D., 2005, "Two-Surface Soil Constitutive Model Calibration for Coarse Granular Materials," Geotechnical Special Publications, pp. 2549-2563.

10. Bica, A. V. D., Bressani, L. A., Vendramin, D., Martins, F. B., Ferreira, P. M. V., and Gobbi, F. G., 2008, "Anisotropic Shear Strength of a Residual Soil of Sandstone," Canadian Geotechnical Journal, 45(3), pp. 367-376.

11. Sitharam, T. G., and Vinod, J. S., 2009, "Critical State Behaviour of Granular Materials from Isotropic and Rebounded Paths: DEM Simulations," Granular Matter, 11(1), pp. 33-42.

12. Hoque, E., and Tatsuoka, F., 2004, "Effects of Stress Ratio on Small-Strain Stiffness During Triaxial Shearing," Géotechnique, 54(7), pp. 429-439.

13. Anhdan, L., and Koseki, J., 2005, "Small Strain Behaviour of Dense Granular Soils by True Triaxial Tests," Soils and Foundations, 45(3), pp. 21-38.

14. Schmidt, M. J., Cazacu, O., and Green, M. L., 2009, "Experimental and Theoretical Investigation of the High-Pressure Behavior of Concrete," International Journal for Numerical and Analytical Methods in Geomechanics, 33(1), pp. 1-23.

15. Kodaka, T., Oka, F., Ohta, H., and Otani, H., "Observation of Compaction Bands Under Triaxial Conditions for Diatomaceous Mudstone," Proc. Proceedings of the International Symposium on Geomechanics and Geotechnics of Particulate Media - Geomechanics and Geotechnics of Particulate Media, pp. 69-75.

16. Ezaoui, A., and Di Benedetto, H., 2009, "Experimental Measurements of the Global Anisotropic Elastic Behaviour of Dry Hostun Sand During Triaxial Tests, and Effect of Sample Preparation," Géotechnique, 59(7), pp. 621-635.

17. Lade, P. V., and Abelev, A. V., 2005, "Characterization of Cross-Anisotropic Soil Deposits from Isotropic Compression Tests," Soils and Foundations, 45(5), pp. 89-102.

18. Wang, L., Hoyos, L. R., Mohammad, L., and Abadie, C., 2005, "Characterization of Asphalt Concrete by Multi-Stage True Triaxial Testing," Journal of ASTM International, 2(10), pp. 7-16.

19. Reddy, K., Saxena, S. K., and Budiman, J. S., 1992, "Development of a True Triaxial Testing Apparatus," Geotechnical Testing Journal, 15(2), pp. 89-105.

20. Zhang, Y., Zhang, B. Y., G-X., L., and Sun, X., 2010, "Combined Tension-Compression Triaxial Tests and Extended Duncan-Chang Model of Compacted Clay," Chinese Journal of Geotechnical Engineering, 32(7), pp. 999-1004.

21. Han, L., Liu, X., Meng, Y., Li, G., Liu, H., and Wu, X., 2010, "Study of Deformation Behaviours of Limestone Under Cycle Triaxial Compression with Different Confining Pressures," Chinese Journal of Rock Mechanics and Engineering, 29(1), pp. 2840-2844.

22. Shi, W. C., Zhu, J. G., He, S. B., and Liu, H. L., 2010, "Stress-Induced Anisotropy of Coarse-Grained Soil by True Triaxial Tests," Chinese Journal of Geotechnical Engineering, 32(5), pp. 810-814.

23. Feng, T. G., Liu, H. L., XIANG, S., Zhou, Y. D., and Gao, Y. F., 2005, "Undrained Cyclical Torsional Shear Tests on Saturated Sand in Different Confining Pressures," Rock and Soil Mechanics, p. S1.

24. Hattab, M., and Hicher, P., 2004, "Dilitating Behaviour of Overconsolidated Clay," Soils and Foundations, 44(4), pp. 27-40.

25. Brannon, R. M., Burghardt, J. A., Bronowski, D., and Bauer, S., 2009, "Experimental Assessment of Unvalidated Assumptions in Classical Plasticity Theory (SAND2009-0351),"Sandia National Laboratories, pp. 1-120.

26. Sandler, I. S., 2005, "Review of the Development of Cap Models for Geomaterials," Shock and Vibration, 12(1), pp. 67-71.

27. Tong, X., and Tuan, C. Y., 2007, "Viscoplastic Cap Model for Soils under High Strain Rate Loading," Journal of Geotechnical and Geoenvironmental Engineering, 133(2), pp. 206-214.

28. Sandler, I. S., and Rubin, D., 1979, "An Algorithm and a Modular Subroutine for the Cap Model," International Journal for Numerical and Analytical Methods in Geomechanics, 3(2), pp. 173-186.

29. Sandler, I. S., Baladi, G. Y., and DiMaggio, F. L., 1976, "Generalized Cap Model for Geological Materials," Journal of the Geotechnical Engineering Division, 102(7), pp. 683-699.

30. Pinheiro, M., and Wan, R. G., 2010, "Finite Element Analysis of Diffuse Instability Using an Implicitly Integrated Pressure-Density Dependent Elastoplastic Model," Finite Elements in Analysis and Design, 46(6), pp. 487-495.

31. Liu, R., Lin, G., and Bhashyam, G., 2010, "Transformation of the Sandler and Rubin Nonsmooth Cap Model to the Pelessone Smooth Cap Model," Journal of Engineering Mechanics, 136(5), pp. 680-685.

32. Aydin, A., Borja, R. I., and Eichhubl, P., 2006, "Geological and Mathematical Framework for Failure Modes in Granular Rock," Journal of Structural Geology, 28(1), pp. 83-98.

33. Issen, K. A., 2002, "The Influence of Constitutive Models on Localization Conditions for Porous Rock," Engineering Fracture Mechanics, 69(17), pp. 1891-1906.

34. Challa, V., and Issen, K. A., 2004, "Conditions for Compaction Band Formation in Porous Rock Using a Two-Yield Surface Model," Journal of Engineering Mechanics, 130(9), pp. 1089-1097.

35. Liu, H. Y., Kou, S. Q., and Lindqvist, P. A., 2002, "Numerical Simulation of the Fracture Process in Cutting Heterogeneous Brittle Material," International Journal for Numerical and Analytical Methods in Geomechanics, 26(13), pp. 1253-1278.

36. Khoei, A., Azami, A., Anahid, M., and Lewis, R., 2006, "A Three-Invariant Hardening Plasticity for Numerical Simulation of Powder Forming Processes Via the Arbitrary Lagrangian–Eulerian FE Model," International Journal for Numerical Methods in Engineering, 66(5), pp. 843-877.

37. Sekiguchi, H., and Ohta, K., "Induced Anisotropy and Time Dependency in Clays," Proc. Proceedings of the 9th ICSMFE, Specialty Session 9, pp. 229-238.

38. Barlat, F., Brem, J. C., Yoon, J. W., Chung, K., Dick, R. E., Lege, D. J., Pourboghrat, F., Choi, S. H., and Chu, E., 2003, "Plane Stress Yield Function for Aluminum Alloy Sheets—Part 1: Theory," International Journal of Plasticity, 19(9), pp. 1297-1319.

39. Barlat, F., Ferreira Duarte, J. M., Gracio, J. J., Lopes, A. B., and Rauch, E. F., 2003, "Plastic Flow for Non-Monotonic Loading Conditions of an Aluminum Alloy Sheet Sample," International Journal of Plasticity, 19(8), pp. 1215-1244.

40. Kyriakides, S., Corona, E., and Miller, J. E., 2004, "Effect of Yield Surface Evolution on Bending Induced Cross Sectional Deformation of Thin-Walled Sections," International Journal of Plasticity, 20(4), pp. 607-618.

41. Belokas, G., and Kawadas, M., 2010, "An Anisotropic Model for Anisotropic Soils. Part I: Theory," Computers and Geotechnics, 37(6), pp. 737-747.

42. Dean, E. T. R., 2005, "Patterns, Fabric, Anisotropy, and Soil Elasto-Plasticity," International Journal of Plasticity, 21(3), pp. 513-571.

43. Tsutsumi, S., and Kaneko, K., 2008, "Constitutive Response of Idealized Granular Media Under the Principal Stress Axes Rotation," International Journal of Plasticity, 24(11), pp. 1967-1989.

44. Zhu, H., Mehrabadi, M. M., and Massoudi, M., 2006, "Three-Dimensional Constitutive Relations for Granular Materials Based on the Dilatant Double Shearing Mechanism and the Concept of Fabric," International Journal of Plasticity, 22(5), pp. 826-857.

45. Yang, Y., Yu, H. S., and Muraleetharan, K. K., 2005, "Solution Existence Conditions for Elastoplastic Constitutive Models of Granular Materials," International Journal of Plasticity, 21(12), pp. 2406-2425.

46. Robinson, D. N., and Binienda, W. K., 2001, "Model of Viscoplasticity for Transversely Isotropic Inelastically Compressible Solids," Journal of Engineering Mechanics, 127(6), pp. 567-573.

47. Svendsen, B., Levkovitch, V., Wang, J., Reusch, F., and Reese, S., 2006, "Application of the Concept of Evolving Structure Tensors to the Modeling of Initial and Induced Anisotropy at Large Deformation," Computers & Structures, 84(17), pp. 1077-1085.

48. Bertram, A., and Böhlke, T., 1999, "Simulation of Texture Induced Elastic Anisotropy of Polycrystalline Copper," Computational Materials Science, 16(1), pp. 2-9.

49. Mortara, G., 2010, "A Yield Criterion for Isotropic and Cross-Anisotropic Cohesive-Frictional Materials," International Journal for Numerical and Analytical Methods in Geomechanics, 34(9), pp. 953-977.

50. Dragon, A., Halm, D., and Désoyer, T., 2000, "Anisotropic Damage in Quasi-Brittle Solids: Modelling, Computational Issues and Applications," Computer Methods in Applied Mechanics and Engineering, 183(3-4), pp. 331-352.

51. Weng, M. C., Jeng, F. S., Hsieh, Y. M., and Huang, T. H., 2008, "A Simple Model for Stress-Induced Anisotropic Softening of Weak Sandstones," International Journal of Rock Mechanics and Mining Sciences, 45(2), pp. 155-166.

52. Carol, I., Rizzi, E., and Willam, K., 2002, "An 'Extended' Volumetric/Deviatoric Formulation of Anisotropic Damage Based on a Pseudo-Log Rate," European Journal of Mechanics-A/Solids, 21(5), pp. 747-772.

53. Toi, Y., and Che, J. S., 1994, "Computational Damage Mechanics Models for Brittle Microcracking Solids Based on Mesoscopic Simulations," Engineering Fracture Mechanics, 48(4), pp. 483-498.

54. Wimmer, S. A., and Karr, D. G., 1996, "Compressive Failure of Microcracked Porous Brittle Solids," Mechanics of Materials, 22(4), pp. 265-277.

55. Jeng, F. S., Weng, M. C., Lin, M. L., and Huang, T. H., 2004, "Influence of Petrographic Parameters on Geotechnical Properties of Tertiary Sandstones from Taiwan," Engineering Geology, 73(1-2), pp. 71-91.

56. Olsson, W. A., 1995, "Development of Anisotropy in the Incremental Shear Moduli for Rock Undergoing Inelastic Deformation," Mechanics of Materials, 21(3), pp. 231-242.

57. Manthei, G., 2005, "Characterization of Acoustic Emission Sources in a Rock Salt Specimen Under Triaxial Compression," Bulletin of the Seismological Society of America, 95(5), pp. 1674-1700.

58. Herget, G., 1988, Stresses in Rock, Balkema Rotterdam, New York.

59. Janach, W., and Guex, L. H., 1980, "In-Plane Propagation of Shear Microcracks in Brittle Rocks Under Triaxial Compression," Journal of Geophysical Research, 85(B5), pp. 2543-2553.

60. Sfer, D., Gettu, R., and Etse, G., 2002, "Study of the Behavior of Concrete Under Triaxial Compression," Journal of Engineering Mechanics, 128, p. 156163.

61. Lei, X. L., Kusunose, K., Nishizawa, O., Cho, A., and Satoh, T., 2000, "On the Spatio-Temporal Distribution of Acoustic Emissions in Two Granitic Rocks Under

Triaxial Compression: the Role of Pre-Existing Cracks," Geophysical Research Letters, 27(13), pp. 1997-2000.

62. Zhu, W., Montesi, L. G. J., and Wong, T., 1997, "Shear-Enhanced Compaction and Permeability Reduction: Triaxial Extension Tests on Porous Sandstone," Mechanics of Materials, 25(3), pp. 199-214.

63. Leukart, M., and Ramm, E., 2006, "Identification and Interpretation of Microplane Material Laws," Journal of Engineering Mechanics, 132(3), pp. 295-305.

64. Toi, Y., and Che, J. S., 1994, "Mesoscopic Simulation of Microcracking Behaviors of Brittle Polycrystalline Solids (First Report, Study of Isotropic Theory in Continuum Damage Mechanics)," JSME International Journal, Series A: Mechanics and Material Engineering, 37(4), pp. 434-441.

65. Abelev, A. V., Gutta, S. K., Lade, P. V., and Yamamuro, J. A., 2007, "Modeling Cross Anisotropy in Granular Materials," Journal of Engineering Mechanics, 133, pp. 919-932.

66. Zhu, Q., and Hu, D., 2008, "Research on Homogenization-Based Mesomechanical Damage Model and Its Application," Chinese Journal of Rock Mechanics and Engineering, 2(27), pp. 266-272.

67. Kowalczyk, K., and Ostrowska-Maciejewska, J., 2002, "Energy-Based Limit Conditions for Transversally Isotropic Solids," Archives of Mechanics, 54(5-6), pp. 496-523.

68. Theocaris, P. S., 1995, "The Extension of Beltrami's Ellipsoid to Anisotropic Bodies," Archive of Applied Mechanics, 65(2), pp. 86-98.

69. Molla-Abbasi, K., and Schuette, H., 2007, "Numerical Analysis of the Anisotropic Damage Evolution due to a Growing Mixed-Mode Crack," Key Engineering Materials, 348, pp. 401-404.

70. Wimmer, S. A., and Karr, D. G., "Brittle Compressive Failure of Microcracked Ice," Proc. Proceedings of the International Conference on Offshore Mechanics and Artic Engineering - OMAE, pp. 23-28.

71. Papanikolaou, V. K., and Kappos, A. J., 2007, "Confinement-Sensitive Plasticity Constitutive Model for Concrete in Triaxial Compression," International Journal of Solids and Structures, 44(21), pp. 7021-7048.

72. Kachanov, M., 1992, "Effective Elastic Properties of Cracked Solids," Applied Mechanics Review, 45(8).

73. Kachanov, M., Tsukrov, I., and Shafiro, B., 1994, "Effective Moduli of Solids with Cavities of Various Shapes," Applied Mechanics Reviews, 47, p. 151.

74. Guerrero, F., Sevostianov, I., and Giraud, A., 2007, "On an Arbitrarily Oriented Crack in a Transversely-Isotropic Medium," International Journal of Fracture, 148(3), pp. 273-279.

75. Sevostianov, I., and Kachanov, M., 2008, "On Approximate Symmetries of the Elastic Properties and Elliptic Orthotropy," International Journal of Engineering Science, 46(3), pp. 211-223.

76. Kachanov, M., Mear, M. E., Rungamornrat, J., and Sevostianov, I., 2009, "Resistances of Non-Flat Cracks and Their Relation to Crack Compliances," International Journal of Engineering Science, 47(7-8), pp. 754-766.

77. Sevostianov, I., Kachanov, M., and Zohdi, T., 2008, "On Computation of the Compliance and Stiffness Contribution Tensors of Non-Ellipsoidal Inhomogeneities," International Journal of Solids and Structures, 45(16), pp. 4375-4383.

78. von Mises, R., 1913, "Mechanik der Festen Körper im Plastisch-Deformablen Zustand," Göttin. Nachr. Math. Phys, 1, pp. 582-592.

79. Tsai, S. W., and Wu, E. M., 1971, "A General Theory of Strength for Anisotropic Materials," Journal of Composite Materials, 5(1), pp. 58-80.

80. Brannon, R. M., 2012 (Expected completion 2014), "Functional and Structured Cartesian Tensor Analysis for Engineers,"http://csm.mech.utah.edu/content/2011/03/03/functional-and-structured-tensor-analysis-for-engineers/, p. ~1000.

81. Brannon, R. M., 1996, "Expectations of Transversely Isotropic Tensors Over an Axisymmetric Distribution," Unpublished Work.

82. Fuller, T., and Brannon, R. M., 2011, "On the Thermodynamic Requirement of Elastic Stiffness Anisotropy in Isotropic Materials," International Journal of Engineering Science, 49, pp. 311-321.

83. Brannon, R. M., 1996, "Large Deformation Analysis of Axisymmetric Inhomogeneities Including Coupled Elastic and Plastic Anisotropy (SAND96-2846C)," Sandia National Labs., Albuquerque, NM (United States).

84. Dienes, J. K., Zuo, Q. H., and Kershner, J. D., 2006, "Impact Initiation of Explosives and Propellants via Statistical Crack Mechanics," Journal of the Mechanics and Physics of Solids, 54(6), pp. 1237-1275.

85. Kachanov, M., 1980, "Continuum Model of Medium with Cracks," Journal of the Engineering Mechanics Division, 106(5), pp. 1039-1051.

86. Graham-Brady, L., 2010, "Statistical Characterization of Meso-Scale Uniaxial Compressive Strength in Brittle Materials with Randomly Occurring Flaws," International Journal of Solids and Structures, 47(18), pp. 2398-2413.

87. Ashby, M. F., 1986, "The Gailure of Brittle Solids Containing Small Cracks Under Compressive Stress States," Acta Metallurgica, 34(3), pp. 497-510.

88. Azhdari, A., and Nemat-Nasser, S., 1996, "Energy-Release Rate and Crack Kinking in Anisotropic Brittle Solids," Journal of the Mechanics and Physics of Solids, 44(6), pp. 929-951.

89. Horii, H., and Nemat-Nasser, S., 1985, "Compression-Induced Microcrack Growth in Brittle Solids; Axial Splitting and Shear Failure," Journal of Geophysical Research, 90(B4), pp. 3105-3125.

90. Bobet, A., 2000, "The Initiation of Secondary Cracks in Compression," Engineering Fracture Mechanics, 66, pp. 187-219.

91. Brannon, R. M., 2007, "Elements in Phenomenological Plasticity: Geometric Insight, Computational Algorithms, and Applications in Shock Physics," Shock Wave Science and Technology Reference Library Volume 2, Y. Horie, ed., Springer, New York, pp. 189-274.

APPENDIX A: FORM AND SYMMETRY OF THE DISTORTION OPERATOR

A failure function, $h\left(\underset{\approx}{\varepsilon}\right)$, can be written in terms of the strain deviator, $dev\left(\underset{\approx}{\varepsilon}\right)$, as

$$h\left(\underset{\approx}{\varepsilon}\right) = dev\left(\underset{\approx}{\varepsilon}\right) : dev\left(\underset{\approx}{\varepsilon}\right) - k^2 \tag{A.1}$$

Equation (A.1) can be written in terms of a projector

$$h\left(\underset{\approx}{\varepsilon}\right) = \left\| \underset{\underset{\sim}{\approx}}{P}^{sd} : \underset{\approx}{\varepsilon} \right\|^2 - k^2 = 0 \tag{A.2}$$

where $\underset{\underset{\sim}{\approx}}{P}^{sd}$ is the “symdev” operator $\underset{\underset{\sim}{\approx}}{P}^{sd} = \frac{1}{2}\left(\delta_{im}\delta_{jn} + \delta_{in}\delta_{jm}\right) - \frac{1}{3}\delta_{ij}\delta_{mn}$. Equation (B.2) can be written as a stress failure criterion

$$f\left(\underset{\approx}{\sigma}, \underset{\underset{\sim}{\approx}}{S}\right) = \left\| \underset{\underset{\sim}{\approx}}{P}^{sd} : \underbrace{\underset{\underset{\sim}{\approx}}{S} : \underset{\approx}{\sigma}}_{\underset{\approx}{\varepsilon}} \right\|^2 - k^2 = 0 \tag{A.3}$$

where $\underset{\approx}{\sigma}$ is the stress tensor, and $\underset{\underset{\sim}{\approx}}{S}$ is the fourth-order compliance tensor. In this case, $\underset{\underset{\sim}{\approx}}{S}$ represents the compliance of the damaged material. The goal is to relate $\underset{\underset{\sim}{\approx}}{S}$ to the compliance of the undamaged material, $\underset{\underset{\sim}{\approx}}{S}_o$. A failure criterion based on the compliance of the undamaged material can be written as

$$f_o\left(\underset{\approx}{\sigma}\right) = f\left(\underset{\approx}{\sigma}, \underset{\underset{\sim}{\approx}}{S}_o\right) = \left\| \underset{\underset{\sim}{\approx}}{P}^{sd} : \underset{\underset{\sim}{\approx}}{S}_o : \underset{\approx}{\sigma} \right\|^2 - k^2 = 0 \tag{A.4}$$

It is necessary to relate $f\left(\underset{\approx}{\sigma}, \underset{\underset{\sim}{\approx}}{S}\right)$ to $f_o\left(\underset{\approx}{\sigma}\right)$, and this is done through the use of a fourth-order tensor, $\underset{\underset{\sim}{\approx}}{L}$ as

$$f\left(\underset{\approx}{\sigma}, \underset{\underset{\sim}{\approx}}{S}\right) = f_o\left(\underset{\underset{\sim}{\approx}}{L} : \underset{\approx}{\sigma}\right) \tag{A.5}$$

Substituting Equations (A.3) and (A.4) into Equation (A.5) yields

$$\underset{\underset{\sim}{\approx}}{P}^{sd} : \underset{\underset{\sim}{\approx}}{S} = \underset{\underset{\sim}{\approx}}{P}^{sd} : \underset{\underset{\sim}{\approx}}{S}_o : \underset{\underset{\sim}{\approx}}{L} \tag{A.6}$$

Equation (A.6) suggests that

$$\underset{\underset{\sim}{\approx}}{S} = \underset{\underset{\sim}{\approx}}{S}_o : \underset{\underset{\sim}{\approx}}{L} \quad \Rightarrow \quad \underset{\underset{\sim}{\approx}}{L} = \left(\underset{\underset{\sim}{\approx}}{S}_o\right)^{-1} : \underset{\underset{\sim}{\approx}}{S} = \underset{\underset{\sim}{\approx}}{C}_o : \underset{\underset{\sim}{\approx}}{S} \tag{A.7}$$

where $\underset{\underset{\sim}{\approx}}{C}_o$ is the stiffness tensor of the undeformed material.

The distortion operator is shown below to be symmetric. From Equation (19), an anisotropic yield function can be written in the form (with backstress and other internal state variables assumed to be present implicitly)

$$f\left(\underset{\approx}{\sigma}\right)=\underset{\approx}{\sigma}^{T}:\underset{\approxeq}{L}^{T}:\underset{\approxeq}{L}:\underset{\approx}{\sigma} \qquad \text{(A.8)}$$

Based on the definition of positive definite as

$$\underset{\approx}{\alpha}:\underset{\approxeq}{\gamma}:\underset{\approx}{\alpha}>0 \quad \forall\ \underset{\approx}{\alpha}\neq 0 \qquad \text{(A.9)}$$

where $\underset{\approx}{\alpha}$ is an arbitrary second order tensor. If the $\underset{\approxeq}{\gamma}$ tensor appears in a theory only quadratic forms, such as above, then it may be assumed to be symmetric without loss (i.e., if it is not symmetric, the value of the quadratic form is unchanged if $\underset{\approxeq}{\gamma}$ is replaced by its symmetric part). Thus, although the $\underset{\approxeq}{L}$ tensor in Equation (A.7) is not symmetric, it may be replaced by its symmetric part because its definition in this research appears as a quadratic form in the definition of the anisotropic yield function.

APPENDIX B: EVALUATION OF β

In deviatoric versus isotropic space, $\tan(\beta)$ (as defined in **Figure 21**) can be defined as

$$\tan(\beta) = \frac{\left\| iso\left(\frac{\partial f}{\partial \underset{\approx}{\sigma}}\right) \right\|}{\left\| dev\left(\frac{\partial f}{\partial \underset{\approx}{\sigma}}\right) \right\|} \tag{B.1}$$

The numerator in Equation (B.1) is

$$\begin{aligned} \left\| iso\left(\frac{\partial f}{\partial \underset{\approx}{\sigma}}\right) \right\| &= \left\| \frac{1}{3} tr\left(\frac{\partial f}{\partial \underset{\approx}{\sigma}}\right) \underset{\approx}{I} \right\| = \frac{1}{\sqrt{3}} \left| tr\left(\frac{\partial f}{\partial \underset{\approx}{\sigma}}\right) \right| \\ &= -\frac{8}{\sqrt{3}} G_o \Delta \tilde{\alpha}_3 \left(\frac{\sigma_A^* - \sigma_L^*}{3} \right) \end{aligned} \tag{B.2}$$

where the last step used the value of $tr\left(\partial f / \partial \underset{\approx}{\sigma}\right)$, previously defined in Equation (72). For triaxial compression, both stress components are compressive and the axial stress is more compressive than the lateral stress. Since this work adopts the sign convention that stress is positive in compression, triaxial compression therefore corresponds to $\sigma_A^* - \sigma_L^* < 0$, which is the source of the negative in the above equation so that the final result is positive.

The magnitude of the denominator in Equation (B.1) is found from

$$\left\| dev\left(\frac{\partial f}{\partial \underset{\approx}{\sigma}}\right) \right\| = \sqrt{dev\left(\frac{\partial f}{\partial \underset{\approx}{\sigma}}\right) : dev\left(\frac{\partial f}{\partial \underset{\approx}{\sigma}}\right)} \tag{B.3}$$

The partial $\left(\partial f / \partial \underset{\approx}{\sigma}\right)$ is given by Equation (70) and when inserted into Equation (B.3) yields

$$\left\| dev\left(\frac{\partial f}{\partial \underset{\approx}{\sigma}}\right)\right\| = \left[\begin{array}{l} 4\left(dev\left(\underset{\approx}{\sigma}^*\right) : dev\left(\underset{\approx}{\sigma}^*\right)\right) \\ +16 G_o \Delta\tilde{\alpha}_3 \left(dev\left(\underset{\approx}{\sigma}^*\right) : dev\left(dev\left(\underset{\approx}{\sigma}^*\right) : \underset{\approx\approx}{\tilde{B}_3}\right)\right) \\ +16 G_o^2 \Delta\tilde{\alpha}_3^2 \left(dev\left(dev\left(\underset{\approx}{\sigma}^*\right) : \underset{\approx\approx}{\tilde{B}_3}\right) : dev\left(dev\left(\underset{\approx}{\sigma}^*\right) : \underset{\approx\approx}{\tilde{B}_3}\right)\right) \end{array}\right]^{\frac{1}{2}} \tag{B.4}$$

For TXC loading in the 3-direction, $dev\left(\underset{\approx}{\sigma}^*\right)$ is

$$dev\left(\underset{\approx}{\sigma}^*\right) = \frac{\sigma_A^* - \sigma_L^*}{3}\begin{bmatrix} -1 & 0 & 0 \\ 0 & -1 & 0 \\ 0 & 0 & 2 \end{bmatrix} \tag{B.5}$$

From Equation (C.4), the term $dev\left(\underset{\approx}{\sigma}^*\right) : dev\left(\underset{\approx}{\sigma}^*\right)$ is found through the use of Equation (B.5) as

$$dev\left(\underset{\approx}{\sigma}^*\right) : dev\left(\underset{\approx}{\sigma}^*\right) = \frac{2}{3}\left(\sigma_A^* - \sigma_L^*\right)^2 \tag{B.6}$$

From Equation (C.4), $dev\left(dev\left(\underset{\approx}{\sigma}^*\right) : \underset{\approx\approx}{\tilde{B}_3}\right)$ is calculated as

$$dev\left(dev\left(\underset{\approx}{\sigma}^*\right) : \underset{\approx\approx}{\tilde{B}_3}\right) = \frac{\sigma_A^* - \sigma_L^*}{3}\left\{\frac{1}{6} \quad \frac{1}{6} \quad -\frac{1}{3} \quad 0 \quad 0 \quad 0\right\}^T \tag{B.7}$$

From Equations (C.5) and (C.7), $dev\left(\underset{\approx}{\sigma}^*\right):dev\left(dev\left(\underset{\approx}{\sigma}^*\right):\underset{\approx\approx}{\tilde{B}_3}\right)$ is found as

$$dev\left(\underset{\approx}{\sigma}^*\right):dev\left(dev\left(\underset{\approx}{\sigma}^*\right):\underset{\approx\approx}{\tilde{B}_3}\right)=(-1)\left(\frac{\sigma_A^*-\sigma_L^*}{3}\right)^2 \qquad \text{(B.8)}$$

The term $\left(dev\left(dev\left(\underset{\approx}{\sigma}^*\right):\underset{\approx\approx}{\tilde{B}_3}\right):dev\left(dev\left(\underset{\approx}{\sigma}^*\right):\underset{\approx\approx}{\tilde{B}_3}\right)\right)$ from Equation (C.7) is

$$\left(dev\left(dev\left(\underset{\approx}{\sigma}^*\right):\underset{\approx\approx}{\tilde{B}_3}\right):dev\left(dev\left(\underset{\approx}{\sigma}^*\right):\underset{\approx\approx}{\tilde{B}_3}\right)\right)=\frac{\left(\sigma_A^*-\sigma_L^*\right)^2}{54} \qquad \text{(B.9)}$$

Substitution of Equations (B.6), (B.8), and (B.9) into Equation (B.4) gives

$$\begin{aligned}\left\|dev\left(\frac{\partial f}{\partial \underset{\approx}{\sigma}}\right)\right\| &= \left[\Delta\tilde{\alpha}_3^2\frac{8}{27}G_o^2\left(\sigma_A^*-\sigma_L^*\right)^2-\Delta\tilde{\alpha}_3\frac{16}{9}G_o\left(\sigma_A^*-\sigma_L^*\right)^2+\frac{8}{3}\left(\sigma_A^*-\sigma_L^*\right)^2\right]^{1/2} \\ &= \frac{2\sqrt{6}}{9}\left|\left(G_o\Delta\tilde{\alpha}_3-3\right)\left(\sigma_A^*-\sigma_L^*\right)\right|\end{aligned} \qquad \text{(B.10)}$$

Initially, $\Delta\tilde{\alpha}_3=0$ and therefore $\left(G_o\Delta\tilde{\alpha}_3-3\right)<0$. Recall that, for triaxial compression, $\left(\sigma_A^*-\sigma_L^*\right)<0$. Therefore, initially,

$$\left\|dev\left(\frac{\partial f}{\partial \underset{\approx}{\sigma}}\right)\right\|=\frac{2\sqrt{6}}{9}\left(G_o\Delta\tilde{\alpha}_3-3\right)\left(\sigma_A^*-\sigma_L^*\right) \qquad \text{(B.11)}$$

Inserting Equations (B.2) and (B.11) into Equation (B.1), and simplifying yields

$$\Delta\tilde{\alpha}_3 = \frac{1}{G_o}\left(\frac{3\tan(\beta)}{2\sqrt{2}+\tan(\beta)}\right) \tag{B.12}$$

This result is valid as long as $G_o\Delta\tilde{\alpha}_3 < 3$. A plot of the above function is provided in **Figure 22**, which shows that over the range of β values of interest, $G_o\Delta\tilde{\alpha}_3$ is indeed smaller than 3.

Distribution

1 David Macon (electronic copy)
Mechanical Engineeering Dept., MEB
50 S. Central Campus Drive, Room 2110
Salt Lake City, UT 84112

1 Rebecca Brannon (electronic copy)
Mechanical Engineeering Dept., MEB
50 S. Central Campus Drive, Room 2110
Salt Lake City, UT 84112

1	MS0751	Tom Dewers	6914 (electronic copy)
1	MS0840	Lupe Arguello	1525 (electronic copy)
1	MS0840	Joe Bishop	1525 (electronic copy)
1	MS0840	Tim Fuller	1525 (electronic copy)
1	MS0847	Steve Attaway	1525 (electronic copy)
1	MS1323	O. Erik Strack	1443 (electronic copy)
1	MS0899	Technical Library	9536 (electronic copy)

Sandia National Laboratories